

# Physical and chemical complexity in high-mass star-forming regions with ALMA.

## I. Overview and evolutionary trends of physical properties

C. Gieser<sup>1,2</sup>, H. Beuther<sup>1</sup>, D. Semenov<sup>1,3</sup>, A. Ahmadi<sup>4</sup>, Th. Henning<sup>1</sup>, and M. R. A. Wells<sup>1</sup>

<sup>1</sup> Max Planck Institute for Astronomy, Königstuhl 17, 69117 Heidelberg, Germany

<sup>2</sup> Max-Planck-Institut für extraterrestrische Physik, Giessenbachstrasse 1, 85748 Garching, Germany,  
e-mail: gieser@mpe.mpg.de

<sup>3</sup> Department of Chemistry, Ludwig Maximilian University, Butenandtstr. 5-13, 81377 Munich, Germany

<sup>4</sup> Leiden Observatory, Leiden University, P.O. Box 9513, 2300 RA Leiden, the Netherlands

Received...; accepted...

### ABSTRACT

**Context.** High-mass star formation is a hierarchical process from cloud ( $>1$  pc), to clump (0.1-1 pc) to core scales ( $<0.1$  pc). Modern interferometers achieving high angular resolutions at mm wavelengths allow us to probe the physical and chemical properties of the gas and dust of protostellar cores in the earliest evolutionary formation phases.

**Aims.** In this study, we investigate how physical properties, such as the density and temperature profiles, evolve on core scales through the evolutionary sequence during high-mass star formation ranging from protostars in cold infrared dark clouds to evolved UCHII regions.

**Methods.** We observed 11 high-mass star-forming regions with the Atacama Large Millimeter/submillimeter Array (ALMA) at 3 mm wavelengths. Based on the 3 mm continuum morphology and H(40) $\alpha$  recombination line emission, tracing locations with free-free (ff) emission, the fragmented cores analyzed in this study are classified into either “dust” or “dust+ff” cores. In addition, we resolve three cometary UCHII regions with extended 3 mm emission that is dominated by free-free emission. The temperature structure and radial profiles ( $T \sim r^{-q}$ ) are determined by modeling molecular emission of CH<sub>3</sub>CN and CH<sub>3</sub><sup>13</sup>CN with XCLASS and by using the HCN-to-HNC intensity ratio as probes for the gas kinetic temperature. The density profiles ( $n \sim r^{-p}$ ) are estimated from the 3 mm continuum visibility profiles. The masses  $M$  and H<sub>2</sub> column densities  $N(\text{H}_2)$  are then calculated from the 3 mm dust continuum emission.

**Results.** We find a large spread in mass and peak H<sub>2</sub> column density in the detected sources ranging from 0.1 - 150  $M_{\odot}$  and  $10^{23}$  -  $10^{26}$  cm<sup>-2</sup>, respectively. Including the results of the CORE and CORE-extension studies to increase the sample size, we find evolutionary trends on core scales for the temperature power-law index  $q$  increasing from 0.1 to 0.7 from infrared dark clouds to UCHII regions, while for the density power-law index  $p$  on core scales, we do not find strong evidence for an evolutionary trend. However, we find that on the larger clump scales throughout these evolutionary phases the density profile flattens from  $p \approx 2.2$  to  $p \approx 1.2$ .

**Conclusions.** By characterizing a large statistical sample of individual fragmented cores, we find that the physical properties, such as the temperature on core scales and density profile on clump scales, evolve even during the earliest evolutionary phases in high-mass star-forming regions. These findings provide observational constraint for theoretical models describing the formation of massive stars. In follow-up studies we aim to further characterize the chemical properties of the regions by analyzing the large amount of molecular lines detected with ALMA in order to investigate how the chemical properties of the molecular gas evolve during the formation of massive stars.

**Key words.** star formation – astrochemistry

## 1. Introduction

Current research on high-mass star formation (HMSF) is centered around how gas accretion can efficiently be funneled from large scales toward individual protostars and what processes set the fragmentation within a single high-mass star-forming region (HMSFR). For dedicated reviews regarding observations and theories of HMSF we refer to Beuther et al. (2007a), Bonnell (2007), Zinnecker & Yorke (2007), Smith et al. (2009), Tan et al. (2014), Krumholz (2015), Schilke (2015), Motte et al. (2018), and Rosen et al. (2020). Since the formation of a massive star is fast compared to its low-mass analogues and the distances are typically at a few kiloparsec, they can be best studied in their earliest phases of their formation with interferometric observa-

tions at (sub)mm wavelengths allowing us to probe the dust and molecular gas on core scales ( $<0.1$  pc).

Massive stars form in the densest regions of molecular clouds with typical formation time scales on the order of  $10^5$  yr (McKee & Tan 2002, 2003; Mottram et al. 2011; Kuiper & Hosokawa 2018). The evolutionary stages of high-mass protostars can be empirically categorized into four different stages based on observed properties that are further explained in the following:

- infrared dark cloud (IRDC)
- high-mass protostellar object (HMPO)
- hot molecular core (HMC)
- ultra-compact HII (UCHII) region

Considering the underlying physical properties during HMSF (e.g., Beuther et al. 2007a; Zinnecker & Yorke 2007; Gerner

et al. 2014), these evolutionary stages can be related to the high-mass star formation scenario proposed by Motte et al. (2018).

Due to their high extinctions at near-infrared (NIR) and mid-infrared (MIR) wavelengths, IRDCs were initially identified as absorption features against the bright Galactic MIR background, while at far-infrared (FIR) wavelengths they appear in emission (e.g., Rathborne et al. 2006; Henning et al. 2010). IRDCs with sizes of 1–10 pc have a typical density of  $n \gtrsim 10^4 \text{ cm}^{-3}$  and temperature of  $T < 20 \text{ K}$ , and are the birth places of stars (e.g., Carey et al. 1998; Pillai et al. 2006; Rathborne et al. 2006; Zhang et al. 2015). In local high-density regions, star formation with MIR-bright protostellar cores takes place, while in other parts of the cloud prestellar cores can be found that are only detected at FIR and mm wavelengths. In this stage, low- and intermediate-mass protostars and potentially high-mass starless cores exist (Motte et al. 2018).

Dense cores that undergo gravitational collapse can harbor high-mass protostars that have high luminosities,  $L > 10^3 L_{\odot}$ , and high accretion rates,  $\dot{M} \gtrsim 10^{-4} M_{\odot} \text{ yr}^{-1}$ , inferred from large bipolar molecular outflows (e.g., Beuther et al. 2002b; Duarte-Cabral et al. 2013). These are referred to as HMPOs (e.g., Beuther et al. 2002a; Williams et al. 2004; Motte et al. 2007; Beuther et al. 2010). The temperature in the envelope increases due to the central heating of the protostar and since outflows are commonly observed, disks should also be present, but due to their small sizes ( $\lesssim 1000 \text{ au}$ ) they remain challenging to observe (e.g., Sánchez-Monge et al. 2013a; Beltrán & de Wit 2016), while they are commonly found around low-mass protostars (e.g., ALMA Partnership et al. 2015; Andrews et al. 2018; Avenhaus et al. 2018; Öberg et al. 2021). HMPOs are bright at mm wavelengths, but have no or only weak emission at cm wavelengths.

As the protostar heats up the envelope to  $\geq 100 \text{ K}$ , molecules that have resided and/or formed on dust grains evaporate into the gas-phase revealing line rich emission spectra, being classified as HMCs or “hot cores” (Cesaroni et al. 1997; Osorio et al. 1999; Belloche et al. 2013; Sánchez-Monge et al. 2017; Beltrán et al. 2018). In HMCs, complex organic molecules (COMs, consisting six or more atoms, following the definition by Herbst & van Dishoeck 2009) are very abundant, for example, methanol ( $\text{CH}_3\text{OH}$ ), acetone ( $\text{CH}_3\text{COCH}_3$ ), methyl formate ( $\text{CH}_3\text{OCHO}$ ), and ethyl cyanide ( $\text{CH}_3\text{CH}_2\text{CN}$ ) as revealed by spectral line surveys (e.g., Belloche et al. 2013). Due to the ionizing radiation of the protostar, in the central region of the HMC, a hyper-compact (HC) HII region might already be present.

The strong protostellar radiation causes an expansion and further ionization of the surrounding envelope that is eventually disrupted revealing the massive star. The region is then classified to be a UCHII region (e.g., Wood & Churchwell 1989; Hatchell et al. 1998; Garay & Lizano 1999; Kurtz et al. 2000; Churchwell 2002; Palau et al. 2007; Qin et al. 2008; Sánchez-Monge et al. 2013b; Klaassen et al. 2018). UCHII regions can be studied at cm wavelengths due to free-free emission from scattered electrons (Churchwell 2002; Peters et al. 2010) and show diverse spatial morphologies from compact cores to cometary halos (Churchwell 2002). Typical sizes of UCHII regions are  $R < 0.1 \text{ pc}$ , while HCHII regions are even more compact with  $R < 0.01 \text{ pc}$ . At NIR and MIR wavelengths, the massive star might be detectable depending on the extinction in the cloud.

During the formation of high-mass stars, the physical and chemical properties on core scales are diverse (Gieser et al. 2019, 2021, 2022) as revealed in the CORE (Beuther et al. 2018a) and CORE-extension HMSFRs (Beuther et al. 2021) using sub-arcsecond interferometric NOEMA observations at 1 mm wave-

lengths. Since HMSFRs are typically located at distances of a few kpc, the linear resolution is on the order of a few thousand au. This allows us to resolve the envelope of protostellar cores, for which the temperature profile can be described by a power-law profile in the form of

$$T(r) = T_{\text{in}} \times \left(\frac{r}{r_{\text{in}}}\right)^{-q} \quad (1)$$

and the radial density profile in the form of

$$n(r) = n_{\text{in}} \times \left(\frac{r}{r_{\text{in}}}\right)^{-p}. \quad (2)$$

In Gieser et al. (2021, 2022) the temperature and density profiles of a sample of HMSFRs were derived as well as mass,  $M$ , and  $\text{H}_2$  column density,  $N(\text{H}_2)$ , estimates. The regions in the CORE sample (Gieser et al. 2021) are classified to be roughly in the HMPO and HMC stages, while the regions in the CORE-extension sample (Gieser et al. 2022) were classified to be younger and colder regions. In these studies, a mean temperature and density power-law index of  $q \approx 0.4$  and  $p \approx 2.0$ , respectively, is derived. With a spread in  $q$  and  $p$  around the mean values, it was not clear whether a spread is real or due to uncertainties and a small number of analyzed cores.

To increase the sample size of HMSFRs and to investigate evolutionary trends of both physical and chemical properties, we carried out ALMA observations in Cycle 6 targeting in total 11 HMSFRs in Band 3 covering the full evolutionary sequence during HMSF - from protostars in cold IRDCs to evolved UCHII regions. The ALMA continuum and spectral line observations with an angular resolution of  $\approx 1''$  allow us to study the fragmentation and physical properties on core scales and characterize the molecular content of the cores and in the surrounding structures they are embedded in.

The 3 mm spectral setup (Table A.2) covers a variety of molecular lines targeting, for example, high- and low-density and temperature regimes, photochemistry, shocks and outflows, and C-/O-/N-/S- bearing species. Since molecule formation and destruction depends heavily on the underlying physical conditions, with this sample covering multiple evolutionary stages we are able to probe the evolution of physical properties and molecular abundances with time.

In this first study, we analyze the fragmentation properties based on the ALMA 3 mm continuum and the temperature and density profiles. Furthermore, we investigate how the properties change along the evolutionary sequence taking into account the results from the CORE and CORE-extension regions (Gieser et al. 2021, 2022). Future studies will be dedicated to a detailed chemical analysis targeting a variety of processes, for example the formation and spatial morphology of COMs, isotopologues and isomers, shocks, and outflows.

## 2. Sample

The 11 target regions were selected from the chemical study by Gerner et al. (2014, 2015) targeting a total of 59 HMSFRs at all evolutionary phases during HMSF from IRDCs to UCHII regions. Their analysis was based on observations with single-dish telescopes (e.g., with the IRAM 30m telescope) that can not resolve individual fragmented cores at the typical distances of HMSFRs but only trace the larger-scale clump structures. In addition, protostars in various evolutionary phases can be present within one clump as revealed by the CORE (Beuther et al. 2018a; Gieser et al. 2021) and CORE-extension NOEMA observations

Table 1: Overview of the sample.

Region	Phase center		Velocity $v_{\text{LSR}}$ (km s <sup>-1</sup> )	ATLASGAL clump properties <sup>(*)</sup>			
	$\alpha$ (J2000)	$\delta$ (J2000)		Distance $d$ (kpc)	Dust temperature $T_{\text{dust}}$ (K)	Mass $\log M$ ( $\log M_{\odot}$ )	Luminosity $\log L$ ( $\log L_{\odot}$ )
IRDC G11.11-4	18:10:28.30	-19:22:31.5	+29.2	2.9	16	3.0	2.8
IRDC 18223-3	18:25:08.40	-12:45:15.5	+45.3	3.4	13	3.1	2.7
IRDC 18310-4	18:33:39.42	-08:21:10.4	+86.5	5.9	13	3.0	2.5
HMPO IRAS 18089	18:11:51.52	-17:31:28.9	+33.8	2.5	23	3.1	4.3
HMPO IRAS 18182	18:21:09.21	-14:31:45.5	+59.1	4.7	25	3.1	4.3
HMPO IRAS 18264	18:29:14.68	-11:50:24.0	+43.6	3.3	20	3.2	3.9
HMC G9.62+0.19	18:06:14.92	-20:31:39.2	+4.4	5.2	32	3.5	5.4
HMC G10.47+0.03	18:08:38.20	-19:51:50.1	+67.8	8.6	25	4.4	5.7
HMC G34.26+0.15	18:53:18.54	+01:14:57.9	+58.0	1.6	29	3.2	4.8
UCHII G10.30-0.15	18:08:55.92	-20:05:54.6	+13.5	3.6	30	3.3	5.2
UCHII G13.87+0.28	18:14:35.95	-16:45:36.5	+48.3	3.9	34	3.1	5.1

Notes. <sup>(\*)</sup> taken from [Urquhart et al. \(2018\)](#).

([Beuther et al. 2021](#); [Gieser et al. 2022](#)). We therefore observed 11 HMSFRs of the sample by [Gerner et al. \(2014, 2015\)](#) at an angular resolution of  $\approx 1''$  with ALMA in Cycle 6 at 3 mm wavelengths.

In Table 1 the region properties such as the coordinates of the phase center and velocity  $v_{\text{LSR}}$  are summarized with additional information of the larger scale clump properties (distance  $d$ , dust temperature  $T_{\text{dust}}$ , mass  $M$ , and luminosity  $L$ ) taken from the APEX Telescope Large Area Survey of the Galaxy (ATLASGAL, [Urquhart et al. 2018](#)). A short description of each region is given in Appendix B. Within this study, we consistently use the clump properties ( $d$ ,  $L$ ,  $M$ ,  $T_{\text{dust}}$ ) taken from the ATLASGAL survey listed in Table 1. Archival mid-infrared (MIR) and far-infrared (FIR), and cm observations with the Atacama Pathfinder Experiment (APEX), *Herschel*, and *Spitzer* telescopes, and the *Karl G. Jansky* Very Large Array (VLA) are presented in Appendix B in Figs. B.1 – B.11 for a multi-wavelength and multi-scale overview of each region. The *Herschel* 250  $\mu\text{m}$  data, for example, reveal that, except for IRDC 18310-4, all regions are embedded in dense clump structures while being surrounded by filamentary structures that might feed the central hub with new material ([Kumar et al. 2020](#)).

The regions are located at distances in the range of 1.6 kpc to 8.6 kpc (Table 1). Since HMSFRs are less common compared to star-forming regions in the low-mass only regime, it is hardly possible to find a large sample of HMSFRs at different evolutionary stages and at similar distances. However, in Sect. 8.1 we show that the overall clump properties are unbiased by distance in our selected sample.

### 3. Observations

In this study, we use the ALMA 3 mm observations toward the sample in combination with archival MIR, FIR, and cm data with the *Spitzer*, *Herschel*, and APEX telescopes, and the VLA. The ALMA data calibration and imaging procedure is explained in Sect. 3.1 and an overview of the archival data is given in Sect. 3.2.

#### 3.1. ALMA

The ALMA observations were carried out during Cycle 6 with the project code 2018.1.00424.S (PI: Caroline Gieser). In total, 12 science targets were observed in Band 3 covering a (non-continuous) spectral range (SPR) from 86–110 GHz in three different spectral range setups (referred to as SPR1, SPR2, and SPR3) and in total 39 spectral windows (spws), summarized in Table A.2. In order to reduce off-source time, the regions were grouped into three fields (referred to as Field 1, Field 2 and Field 3, last column in Table 2). One of the observed science targets turned out to be a misclassified UCHII region ([Wood & Churchwell 1989](#)) and is in fact a planetary nebula ([Walsh et al. 2003](#); [Thompson et al. 2006](#)) and is not further discussed in the following analysis, however the ALMA data will be presented in [Moraga et al.](#) (in preparation).

The initial strategy of the observations was to observe all regions with three array configurations, two with the “12m-array” (C43-4 and C43-1) and one with the Atacama Compact Array (ACA, also referred to as the “7m-array”) covering spatial scales from  $1''$  to  $60''$ . Since not all observations could be carried out during Cycle 6, the intermediate C43-1 configuration is missing for the most part, however, the  $uv$  coverage of the C43-4 and ACA configurations have a sufficient overlap in order to successfully combine the data. For Field 2/SPR3, the C43-4 configuration is missing, however, these regions were observed with the C43-1 configuration instead. For the remaining fields and spectral setups, observations in the C43-1 configuration are missing, but data in the C43-4 configuration is available. Therefore, the angular resolution of Field 2/SPR3 is lower ( $\approx 3''$ ) compared to the SPR3 line data products of Field 1 and Field 3 ( $\approx 1''$ ).

A summary of all ALMA Cycle 6 observations - including the array configuration, observation date, precipitable water vapor (PWV) and minimum and maximum baseline - is presented in Table A.1. During the observations from October 2018 until May 2019, the PWV ranged from 1–6 mm sufficient for observations at 3 mm wavelengths. The baselines cover 9–1 400 m. We do not have complementary observations with the total power array to recover missing short-spacing information, we therefore filter out spatial scales  $>60''$  in both the continuum and spectral line data.

Table 2: Overview of the ALMA 3 mm continuum data products.

Region	Beam		Noise $\sigma_{\text{cont}}$ (mJy beam <sup>-1</sup> )	Peak intensity $I_{3\text{mm}}^{\text{region}}$ (mJy beam <sup>-1</sup> )	Flux density $F_{3\text{mm}}^{\text{region}}$ (mJy)	Field
	$\theta_{\text{maj}} \times \theta_{\text{min}}$ ("×")	PA (°)				
IRDC G11.11–4	1.0×0.8	104	0.033	1.4	15	Field 2
IRDC 18223–3	1.0×0.7	108	0.022	2.9	23	Field 3
IRDC 18310–4	1.0×0.7	111	0.022	1.2	4.0	Field 3
HMPO IRAS 18089	0.8×0.7	101	0.057	24	130	Field 2
HMPO IRAS 18182	1.1×0.7	107	0.029	13	90	Field 3
HMPO IRAS 18264	1.0×0.7	108	0.031	9.9	130	Field 3
HMC G9.62+0.19	0.9×0.7	104	0.049	58	640	Field 2
HMC G10.47+0.03	0.8×0.7	100	0.25	340	830	Field 2
HMC G34.26+0.15	0.8×0.7	118	1.8	2 500	7 100	Field 1
UCH <sub>II</sub> G10.30–0.15	1.0×0.8	104	0.041	18	1 000	Field 2
UCH <sub>II</sub> G13.87+0.28	1.0×0.8	105	0.065	7.0	1 800	Field 2

**Notes.** The regions are grouped into three fields (Field 1, Field 2, and Field 3) and were observed together during the ALMA observations to reduce off-source calibration time. The flux density  $F_{3\text{mm}}^{\text{region}}$  is computed considering only areas with  $S/N > 5$  within the full ALMA FOV.

The covered frequency ranges and spectral resolution of each of the 39 spws is summarized in Table A.2. In total, there are 36 high-resolution spws with a channel width of 244 kHz ( $\approx 0.8 \text{ km s}^{-1}$  at 3 mm) covering 0.12 GHz each and 3 low-resolution spws with a channel width of 1 MHz ( $\approx 3 \text{ km s}^{-1}$  at 3 mm) covering 1.9 GHz each. The channel width of the three low-resolution spws is not sufficient to resolve typical line widths toward IRDCs ( $\lesssim 3 \text{ km s}^{-1}$ ), however, for the remaining regions, the line emission can be spectrally resolved.

### 3.1.1. Calibration

The data of each observation block (Table A.1) were calibrated using the CASA pipeline (CASA version 5.4.0). When multiple observations were carried out for each SPR, field and array configuration, the data were merged using the `concat` task. Science targets were extracted from the calibrated  $uv$  tables using the `split` task.

In order to extract the 3 mm continuum, we computed an average spectrum for each region, array configuration, and spw in order to determine all line-free channels. All line-free channels were merged using the `concat` task to create a continuum table containing all SPRs and array configurations. To increase the  $S/N$ , the continuum visibilities were averaged over 30 s at a central frequency of 98.3 GHz (corresponding to  $\approx 3$  mm).

The continuum is subtracted from the spectral line data using the `uvcontsub` task by fitting a first-order polynomial to the line-free channels. Using the `concat` task, all array configurations were merged for each SPR. With the `split` task, for each spw a  $uv$  table of the merged spectral line data is created.

### 3.1.2. Self-calibration and imaging

The ALMA continuum and spectral line data are imaged using the `tclean` task. All data are CLEANed using the Hogbom algorithm (Högbom 1974) with Briggs weighting (Briggs 1995) using a robust parameter of 0.5.

To increase the  $S/N$ , we perform phase self-calibration on the continuum data using a similar method adopted for the CORE NOEMA data (Gieser et al. 2021) and apply the solutions to the spectral line data. First, a shallow model of the

continuum data is created using `tclean` with a stopping criterion of either 2 000 CLEAN components or a peak residual intensity of  $0.1 \text{ mJy beam}^{-1}$ . In a first self-calibration loop, the gains based on the source model are determined using the `gaincal` task with a solution interval of 120 s. The gain solutions are applied with the `applycal` task using the “calonly” mode, that does not flag baselines for which the  $S/N$  is too small for self-calibration ( $S/N < 3$ ), therefore long baselines with low  $S/N$  are not self-calibrated but kept in the  $uv$  table in order to maintain a high angular resolution. In the second and third self-calibration loop, the number of iterations increases to 4 000 and 8 000, the peak residual intensity decreases to  $0.05 \text{ mJy beam}^{-1}$  and  $0.025 \text{ mJy beam}^{-1}$ , and the solution interval decreases to 60 s and 30 s, respectively.

The final self-calibrated continuum data are then imaged with a stopping criterion of either 8 000 CLEAN components or a peak residual intensity of  $0.025 \text{ mJy beam}^{-1}$  with a pixel size of  $0.''15$ . An overview of the self-calibrated continuum data products for each region is presented in Table 2. The synthesized beam size is  $\approx 1''$ . Table 2 also shows the continuum peak intensity  $I_{3\text{mm}}^{\text{region}}$  and region-integrated flux density  $F_{3\text{mm}}^{\text{region}}$  considering only areas with  $S/N > 5$ . The continuum noise  $\sigma_{\text{cont}}$  in the regions is smaller than  $0.07 \text{ mJy beam}^{-1}$ , except for HMC G10.47+0.03 and G34.26+0.15. These two regions are bright continuum sources and their spectra do not have many line-free emission channels, which results in a higher continuum noise compared to regions with fainter continuum emission and more line-free channels.

A comparison between the standard-calibrated and self-calibrated continuum data of the HMC G9.62+0.19 region is presented in Fig. 1. This region has a similar complex morphology as the W3 IRS4 region of the CORE sample (Fig. 1 in Gieser et al. 2021). Strong noise artifacts throughout the field-of-view (FOV) due to a high phase noise are clearly corrected by the phase self-calibration procedure decreasing the continuum noise  $\sigma_{\text{cont}}$  by a factor of two. The peak intensity is slightly enhanced as well. Overall, the  $S/N$  is increased by a factor of two from  $\approx 610$  to  $\approx 1 200$  by applying phase self-calibration in the HMC G9.62+0.19 region.

The gain solutions of the phase self-calibrated continuum data are applied to all 39 spws using the `applycal` task, keeping non self-calibrated visibilities with  $S/N < 3$  in order to not



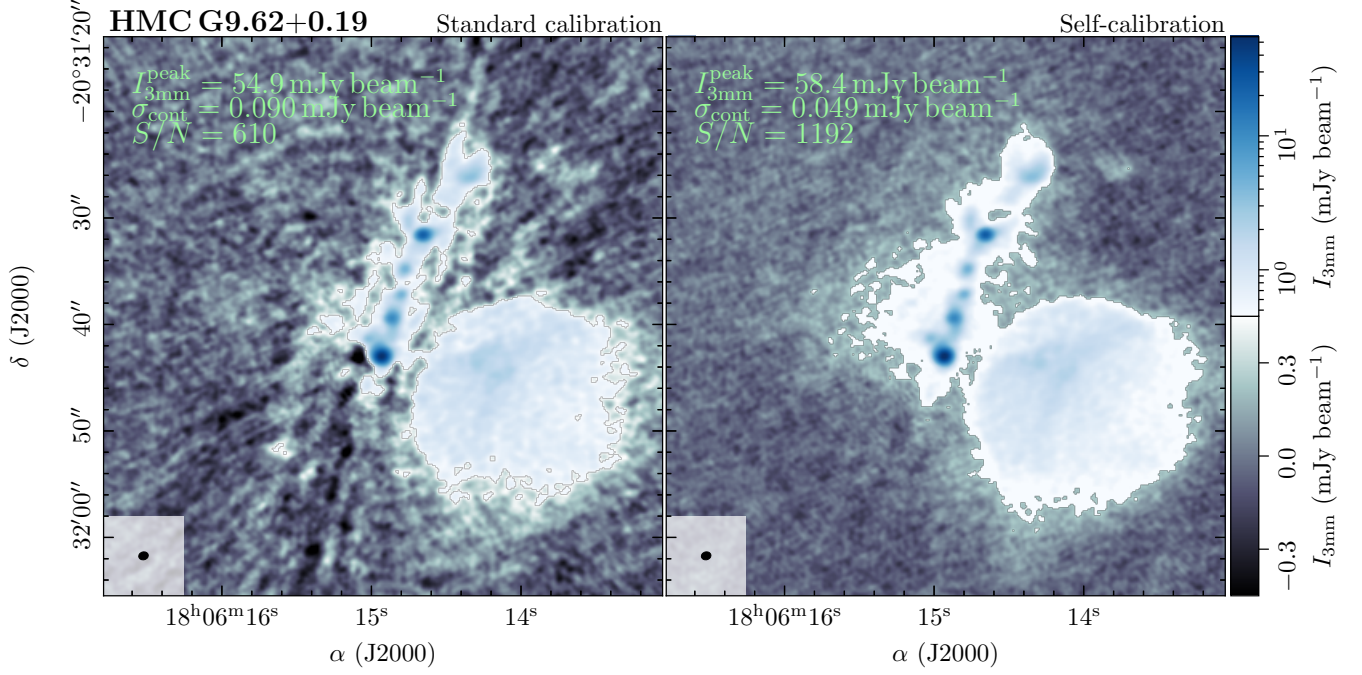


Fig. 1: Comparison of CASA standard calibrated (*left panel*) and CASA self-calibrated (*right panel*) HMC G9.62+0.19 ALMA continuum data. In each panel, the beam size is shown in the bottom left corner. The linear grey-scale and logarithmic blue-scale color map highlight the continuum intensity between  $-5\sigma_{\text{cont}}$  to  $+5\sigma_{\text{cont}}$  and between  $+5\sigma_{\text{cont}}$  and peak intensity of the standard calibrated data, respectively.

Table 3: Transition properties of lines analyzed in this work.

Line	$\nu_0$ (GHz)	$\log A_{ul}$ ( $\log \text{s}^{-1}$ )	$E_u/k_B$ (K)	SPR spw
H(40) $\alpha$	99.023	...	...	SPR2 spw6
HCN 1 – 0	88.630	-4.6	4	SPR1 spw5
HNC 1 – 0	90.664	-4.6	4	SPR3 spw9
CH <sub>3</sub> CN 5 <sub>4</sub> – 4 <sub>4</sub>	91.959	-4.8	128	SPR3 spw13
CH <sub>3</sub> CN 5 <sub>3</sub> – 4 <sub>3</sub>	91.971	-4.6	78	SPR3 spw13
CH <sub>3</sub> CN 5 <sub>2</sub> – 4 <sub>2</sub>	91.980	-4.4	42	SPR3 spw13
CH <sub>3</sub> CN 5 <sub>1</sub> – 4 <sub>1</sub>	91.985	-4.4	20	SPR3 spw13
CH <sub>3</sub> CN 5 <sub>0</sub> – 4 <sub>0</sub>	91.987	-4.4	13	SPR3 spw13
CH <sub>3</sub> <sup>13</sup> CN 5 <sub>4</sub> – 4 <sub>4</sub>	91.913	-4.6	128	SPR3 spw11
CH <sub>3</sub> <sup>13</sup> CN 5 <sub>3</sub> – 4 <sub>3</sub>	91.926	-4.4	78	SPR3 spw11
CH <sub>3</sub> <sup>13</sup> CN 5 <sub>2</sub> – 4 <sub>2</sub>	91.935	-4.3	42	SPR3 spw11
CH <sub>3</sub> <sup>13</sup> CN 5 <sub>1</sub> – 4 <sub>1</sub>	91.940	-4.2	20	SPR3 spw11
CH <sub>3</sub> <sup>13</sup> CN 5 <sub>0</sub> – 4 <sub>0</sub>	91.942	-4.2	13	SPR3 spw11

**Notes.** The line properties are taken from the Cologne Database for Molecular Spectroscopy (CDMS, Müller et al. 2005) and the Jet Propulsion Laboratory (JPL, Pickett et al. 1998) database. The last column refers to the corresponding line data product (SPR and spw) that covers the transition in the ALMA observations (Table A.2).

flag long baseline data. The spectral line data are imaged with a pixel size of  $0.''15$  (except for Field 2/SPR3 with a pixel size of  $0.''5$ ). The CLEAN stopping criterion of the 36 high-resolution spws is a peak residual intensity of  $20 \text{ mJy beam}^{-1}$  (except for Field 2/SPR3 where the threshold is  $28 \text{ mJy beam}^{-1}$ ). The 3 low-resolution spws are CLEANed with a stopping criterion set to  $10 \text{ mJy beam}^{-1}$  of the peak residual intensity.

In this work, we focus on the physical properties of fragmented objects within the regions, we therefore only utilize a few emission lines. H(40) $\alpha$  recombination line emission is used to estimate for which regions and fragments there is a contribution of free-free emission to the 3 mm continuum emission aside from dust emission (Sect. 4.2). Molecular line emission of HCN, HNC, CH<sub>3</sub>CN, and CH<sub>3</sub><sup>13</sup>CN is used to estimate the temperature structure in the regions (Sect. 5). The line properties, such as rest frequency  $\nu_0$  and upper energy level  $E_u/k_B$ , are summarized in Table 3.

The spectral line data products of the lines analyzed in this work are summarized in Table 4. For each field, a mean value for the beam size and line noise are shown. The line noise  $\sigma_{\text{line}}$  in the low-resolution spw containing the H(40) $\alpha$  emission is  $\approx 0.1 \text{ K}$ . The line noise in the high-resolution spws containing the HCN, HNC, CH<sub>3</sub>CN, and CH<sub>3</sub><sup>13</sup>CN is  $\approx 0.7 \text{ K}$  (except for Field 2/SPR3,  $\approx 0.1 \text{ K}$ ). For the purpose of this work, for all regions in Field 2, the HCN spectral line data are imaged using the same baselines, pixel size, and stopping criterion as the HNC observations have (Table A.1). Since in this work we use the HCN-to-HNC intensity ratio (Hacar et al. 2020) to estimate the temperature in the regions (Sect. 5.1) that requires the same angular resolution for both lines for a reliable comparison.

### 3.2. Archival data

We use archival MIR, FIR, and cm data in order to create a multi-wavelength picture of each region in Figs. B.1 - B.11. Science-ready *Spitzer* IRAC  $4.5 \mu\text{m}$  and MIPS  $24 \mu\text{m}$  data are taken from the *Spitzer* Heritage Archive and science-ready *Herschel* PACS  $160 \mu\text{m}$  and SPIRE  $250 \mu\text{m}$  data products are taken from the *Herschel* Science Archive.

Table 4: Overview of the ALMA spectral line data products used in this work.

Line	Field 1			Field 2			Field 3		
	Beam		Noise $\sigma_{\text{line}}$ (K)	Beam		Noise $\sigma_{\text{line}}$ (K)	Beam		Noise $\sigma_{\text{line}}$ (K)
	$\theta_{\text{maj}} \times \theta_{\text{min}}$ ("×")	PA (°)		$\theta_{\text{maj}} \times \theta_{\text{min}}$ ("×")	PA (°)		$\theta_{\text{maj}} \times \theta_{\text{min}}$ ("×")	PA (°)	
H(40) $\alpha$	1.5×1.2	122	0.12	1.9×1.0	105	0.12	1.5×1.0	111	0.11
HCN 1 – 0	0.9×0.8	97	0.73	4.2×2.5	104	0.02	0.9×0.7	102	0.52
HNC 1 – 0	0.8×0.7	80	0.84	4.2×2.5	104	0.08	1.0×0.7	104	0.66
CH <sub>3</sub> CN $J=5 - 4, K=0-4$	0.8×0.7	72	0.85	4.2×2.5	104	0.09	1.1×0.7	98	0.59
CH <sub>3</sub> <sup>13</sup> CN $J=5 - 4, K=0-4$	0.8×0.7	75	0.78	4.2×2.5	104	0.09	0.9×0.7	102	0.66

**Notes.** The transition properties are summarized in Table 3. The line noise  $\sigma_{\text{line}}$  is a mean value taken from the regions grouped within the three fields. Table 2 lists which region is grouped into which field.

The clump properties of the 11 target regions are taken from ATLASGAL results. The 870  $\mu\text{m}$  observations with APEX using the Large APEX Bolometer CAmera (LABOCA) have an angular resolution of 19.''2 (Schuller et al. 2009). The clump properties used in this study are taken from Urquhart et al. (2018) and listed in Table 1. In Figs. B.1 - B.11 it can be clearly seen that an ATLASGAL clump roughly covers the ALMA FOV that is highlighted by a grey circle.

Radio continuum observations at 5 GHz (6 cm) were taken with the VLA as part of the COordinated Radio aNd Infrared Survey for High-mass star formation (CORNISH) project (Hoare et al. 2012) for all regions in our sample except for HMC G9.62+0.19 (Sect. 4.2). The CORNISH project is a 5 GHz (6 cm) radio continuum survey with the VLA covering the Galactic plane at  $10^\circ < l < 65^\circ$  and  $|b| < 1^\circ$  at an angular resolution of 1.''5 and sensitivity of  $\approx 0.3 \text{ mJy beam}^{-1}$  with the primary aim to study UCHII regions. The CORNISH data give a complementary overview for which sources the 3 mm ALMA emission is contaminated by free-free emission (Sect. 4.2).

## 4. Continuum

In this section, we analyze the fragmentation properties in the regions and classify the fragmented objects (Sect. 4.1). The free-free contribution in the 3 mm continuum data for evolved cores and UCHII regions is estimated using the H(40) $\alpha$  recombination line (Sect. 4.2).

The ALMA 3 mm continuum data is presented in Fig. 2 which consists not only of dust emission but also of free-free emission in regions containing evolved protostars. All regions show some level of fragmentation, with some being dominated by a single core (e.g., IRDC G11.11–4 and HMPO IRAS 18089), while others have a number of bright cores (e.g., HMPO IRAS 18182 and HMPO IRAS 18264). In IRDC 18223–3 and HMC G9.62+0.19 the cores are aligned in an elongated filamentary structure. In HMC G34.26+0.15, three UCHII regions (referred to as A, B, and C in the literature, e.g., Mookerjee et al. 2007, corresponding to source 3, 2, and 1 in Fig. 2) are clearly resolved and detected. The UCHII regions G10.30–0.15 and G13.87+0.28 show extended 3 mm emission in the shape of cometary halos. In HMC G9.62+0.19 there is an extended cometary UCHII region toward the south-west of a filament with embedded cores.

### 4.1. Fragmentation and classification

In order to quantify the fragmentation in the continuum data, we use the `clumpfind` algorithm (Williams et al. 1994). The algorithm groups the continuum emission into individual ‘‘clumps’’ and we choose a starting level of  $5\sigma_{\text{cont}}$  and contour spacing of  $5\sigma_{\text{cont}}$ . Although the algorithm is called `clumpfind`, we may not refer to the structures as clumps, but refer to them in the following as cores since with the ALMA observations we trace the core scales with fragments typically smaller than 0.1 pc. The minimum number of pixels in a core is set to 20, which covers a slightly smaller area of one synthesized beam.

The properties (coordinates, relative position, peak intensity, integrated flux, radius) of all cores extracted by the `clumpfind` algorithm are listed in Table C.1. The relative positions are given with respect to the phase center (Table 1). The fragments are sorted by peak intensity and assigned with increasing number at decreasing peak intensity. The radius is calculated from the area  $A$  covered by each identified core by  $r_{\text{out}} = \sqrt{\frac{A}{\pi}}$ .

Since the three cometary UCHII regions (UCHII G10.30–0.15 1, UCHII G13.87+0.28 1, and HMC G9.62+0.19 9, Fig. 2) have extended clumpy morphology, we exclude the area covered by these cometary UCHII regions from the `clumpfind` analysis and treat them as individual structures in our analysis. The peak intensity and integrated flux are computed over the area with  $S/N > 5$  covered by the extended cometary UCHII regions.

The 3 mm continuum emission reveals that cores are embedded in extended envelopes which can themselves be clumpy. In the following analysis we therefore only focus on the cores identified by the `clumpfind` algorithm with a  $S/N > 15$ . With additional 5 GHz data of the CORNISH project and observed H(40) $\alpha$  recombination line revealing regions where the 3 mm emission is a composite of dust and free-free emission, we can further classify the fragmented sources. Cores with no detected H(40) $\alpha$  recombination line emission are referred to as ‘‘dust cores’’, while those with detected H(40) $\alpha$  and 5 GHz emission (Sect. 4.2) are classified as ‘‘dust+ff cores’’. The three extended UCHII regions are classified as ‘‘cometary UCHII regions’’. The classification for each fragment is listed in the last column in Table C.1.

In the following, ‘‘protostellar sources’’ refer to all fragments classified as dust cores, dust+ff cores, and cometary UCHII regions. While the structures with  $S/N < 15$  might also contain protostellar objects, we refrain from analyzing their properties in this work due to insufficient sensitivity and angular resolution, since faint cores are typically unresolved in our data. Since these are minor substructures in our data and the goal of this work is to

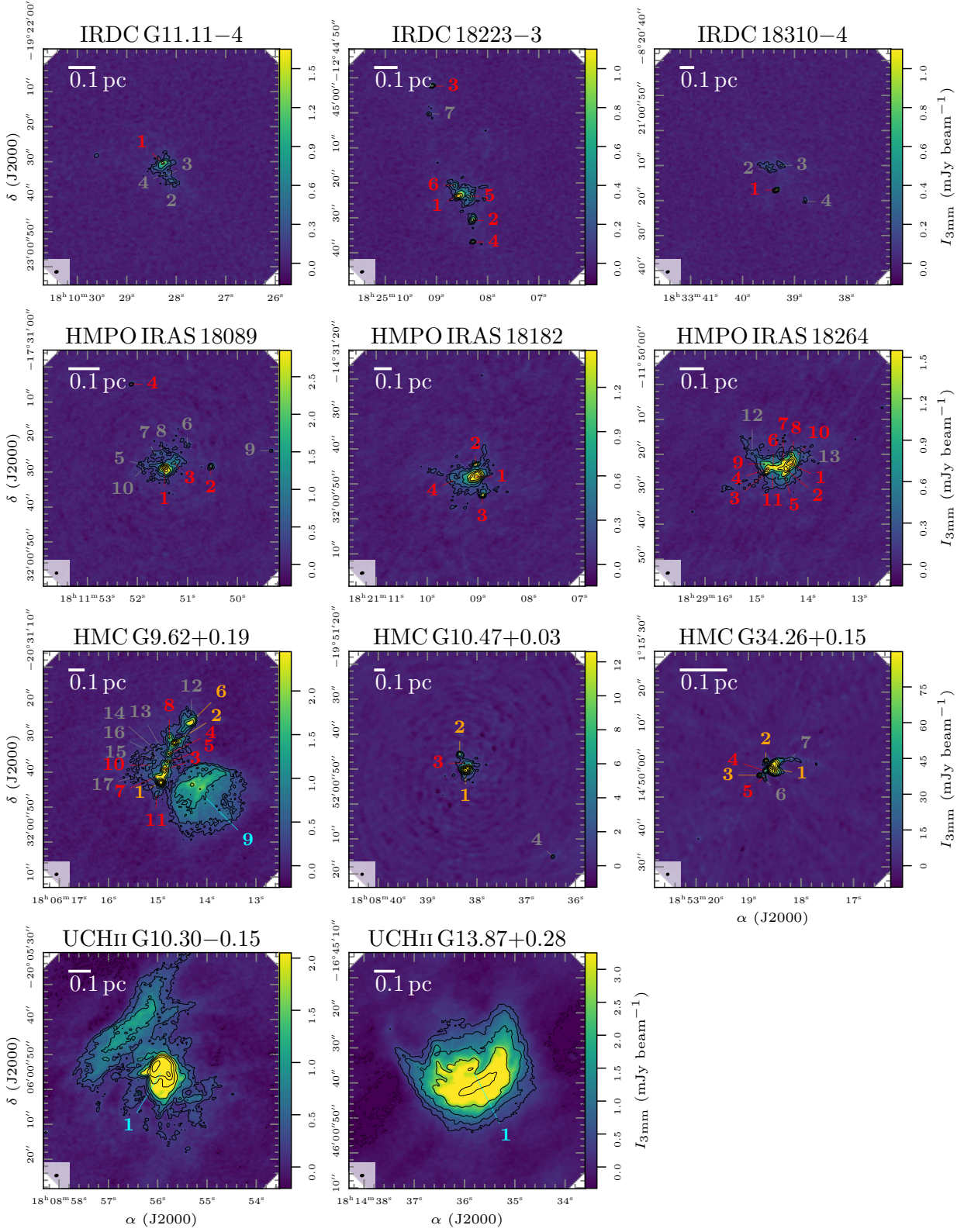


Fig. 2: ALMA 3 mm continuum. In each panel, the continuum data of the region is shown in color and black contours. The dotted black contour marks the  $-5\sigma_{\text{cont}}$  level. The solid black contours start at  $5\sigma_{\text{cont}}$  and contour steps increase by a factor of 2 (e.g., 5, 10, 20,  $40\sigma_{\text{cont}}$ ). The synthesized beam size is shown in the bottom left corner. The bar in the top left corner indicates a linear spatial scale of 0.1 pc. The continuum noise and synthesized beam size are listed in Table 2. The continuum fragments are classified into dust cores (red), dust+ff cores (orange), cometary UCHII regions (cyan), further explained in Sect. 4.1. Fragments with  $S/N < 15$  are not analyzed in this study and are labeled in grey.



study radial density and temperature profiles, we exclude these cores in our analysis.

In total, we extract 48 protostellar sources: 37 dust cores, 8 dust+ff cores, 3 cometary UCHII regions. In total 24 cores extracted using `clumpfind` have  $S/N < 15$  and are not further analyzed in this work. Excluding these cores, the 3 mm peak intensity and integrated flux of the fragments cover 5 orders of magnitudes from 0.44 to 2 500 mJy beam<sup>-1</sup> and 0.75 to 6 600 mJy, respectively and the radii range from 1 100 to 66 000 au.

In the following analysis, we derive the temperature and density profiles ( $T \sim r^{-q}$  and  $n \sim r^{-p}$ ), H<sub>2</sub> column densities  $N(\text{H}_2)$ , and masses  $M$  of the protostellar sources. In order to reliably estimate the H<sub>2</sub> column density and mass (Sect. 7), free-free emission that can have a significant contribution at 3 mm wavelengths has to be subtracted first from the ALMA 3 mm continuum in order to determine the 3 mm dust emission (Sect. 4.2).

#### 4.2. Free-free emission

The continuum emission at mm wavelengths toward young and cold protostars typically arises from optically thin dust emission. An additional contribution from free-free emission can be present for more evolved protostars toward the HMC and UCHII regions. Free-free emission arises from free electrons scattering of ions (Condon & Ransom 2016). The CORNISH 5 GHz data (Figs. B.1 - B.11) reveal that only in the HMCs and UCHII regions strong cm emission is present. Unfortunately, HMC G9.62+0.19 is not covered by the CORNISH survey. In order to reliably estimate the H<sub>2</sub> column density and mass (Sect. 7) for all protostellar sources, the free-free contribution at 3 mm wavelengths is estimated toward the HMC and UCHII regions using the H(40) $\alpha$  recombination line.

Our ALMA 3 mm spectral setup SPR2 covers the H(40) $\alpha$  recombination line allowing us to estimate for which sources there is a significant contribution of free-free emission at 3 mm. The integrated intensity maps of the H(40) $\alpha$  recombination line are shown in Fig. D.1. In all IRDCs and HMPOs, there is no H(40) $\alpha$  emission detected at a line sensitivity of  $\approx 0.1$  K (Table 4) which is expected since these regions are young and is in agreement with the lack of strong cm emission (Figs. B.1 - B.11). In contrast, all HMCs and UCHII regions show at least toward some sources H(40) $\alpha$  emission. Thus the ALMA 3 mm continuum emission is dominated by dust for all IRDCs and HMPOs and a composite of dust and free-free emission for the HMCs and UCHII regions.

All cores with compact 3 mm continuum emission with detected H(40) $\alpha$  emission are classified as dust+ff cores (Sect. 4.1, Table C.1). In addition, all three cometary UCHII regions show extended H(40) $\alpha$  emission. Assuming local thermal equilibrium (LTE) and that the free-free emission is optically thin, we can use the H(40) $\alpha$  recombination line and the line-to-continuum ratio (Condon & Ransom 2016) given by

$$\frac{T_L}{T_C} = 7 \times 10^3 \left( \frac{\Delta v}{\text{km s}^{-1}} \right)^{-1} \left( \frac{\nu}{\text{GHz}} \right)^{1.1} \left( \frac{T_e}{\text{K}} \right)^{-1.15} \left( 1 + \frac{N(\text{He}^+)}{N(\text{H}^+)} \right)^{-1} \quad (3)$$

to estimate the free-free contribution at 3 mm wavelengths.  $T_L$  and  $\Delta v$  are the H(40) $\alpha$  peak intensity and line width, respectively at  $\nu = 99.023$  GHz (Table 3).  $T_e$  and  $\frac{N(\text{He}^+)}{N(\text{H}^+)}$  are the electron temperature and He<sup>+</sup>/H<sup>+</sup> ion ratio, respectively. The corresponding free-free continuum emission is  $T_C$ . Since the H(40) $\alpha$  emission line is covered by the SPR2 setup, we image the SPR2-only

3 mm continuum in order to ensure that exactly the same spatial scales are traced in both data sets. The results for all HMC and UCHII regions are summarized in Fig. D.2. The SPR2 3 mm continuum is shown as contours in all panels in Fig. D.2. In all panels, areas are masked where the H(40) $\alpha$  integrated intensity and SPR2 3 mm continuum have a  $S/N < 5$ . In all bottom panels, the units are converted from units of brightness temperature  $T$  (K) to intensity  $I$  (mJy beam<sup>-1</sup>). The H(40) $\alpha$  peak intensity  $T_L$  is shown in the top left panel for all regions. The line integrated intensity map is shown in the top center panel. The line width  $\Delta v$  is estimated from the  $2\text{nd}$  moment, corresponding to the dispersion  $\sigma^2$ , with  $\Delta v = \sqrt{8 \times \ln(2) \times \sigma^2}$  (top right panel), assuming Gaussian-shaped line profiles. The bottom left panel shows the SPR2 3 mm continuum emission containing both dust and free-free emission. The bottom center panel shows the 3 mm free-free continuum emission calculated using Eq. (3) assuming an electron temperature of  $T_e$  of 5 500 K (e.g., Khan et al. 2022) and  $\frac{N(\text{He}^+)}{N(\text{H}^+)} = 0.08$  (Condon & Ransom 2016). In the bottom right panel the pure dust emission, calculated according to  $I_{3\text{mm,dust}} = I_{3\text{mm,dust+ff}} - I_{3\text{mm,ff}}$ , is shown. In Table 5, the integrated flux of the SPR2 3 mm continuum  $F_{3\text{mm}}$ , free-free  $F_{\text{ff},3\text{mm}}$ , and dust  $F_{\text{dust},3\text{mm}}$  emission is presented for all dust+ff cores and cometary UCHII regions. In addition, the fraction of free-free emission at 3 mm wavelengths,  $\frac{F_{\text{ff},3\text{mm}}}{F_{3\text{mm}}}$  is shown in Table 5.

While for a few dust+ff cores (e.g., HMC G9.62+0.19 2 and HMC G10.47+0.03 1) the free-free emission contributes less than 30% to the total 3 mm continuum, for the remaining sources the 3 mm emission is dominated by free-free emission (>60%) at 3 mm. For HMC G34.26+0.15 1 we might underestimate the free-free contribution at 3 mm since Mookerjee et al. (2007) estimate that at 3 mm the continuum is completely dominated by free-free emission, while we estimate a fraction of 69%. Therefore, we might overestimate the mass and column density in Sect. 7.

## 5. Temperature structure

The temperature in the densest regions in IRDCs is typically very low,  $T < 20$  K (e.g., Carey et al. 1998), but as protostars form, they heat up the surrounding gas and dust and eventually the envelope is completely disrupted. On clump scales, the temperature can be estimated by fitting the spectral energy distribution (SED) of the dust continuum emission (e.g., with *Herschel* observations, Ragan et al. 2012), but the angular resolution is not sufficient to resolve individual cores embedded within their parental clumps. Molecular line emission can also be used to estimate the temperature, for example H<sub>2</sub>CO and CH<sub>3</sub>CN (e.g., Rodón et al. 2012; Gieser et al. 2019, 2021, 2022; Lin et al. 2022). Recently, Hacar et al. (2020) reported that between 15 K and 50 K the HCN-to-HNC intensity ratio provides a good estimate of the temperature.

In this section we use both the HCN-to-HNC intensity ratio (Sect. 5.1), tracing the cold extended gas, and CH<sub>3</sub>CN and CH<sub>3</sub><sup>13</sup>CN line emission (Sect. 5.2), tracing warmer gas, to create temperature maps for all regions. Azimuthal-averaged temperature profiles are computed in Sect. 5.3 for all protostellar sources to estimate the temperature power-law index  $q$  according to Eq. (1).

It has to be noted that these molecular temperature tracers were covered in the spectral setup SPR3 (Sect. 3). For all regions located in Field 2 (Table 1), the angular resolution is poorer ( $\approx 3''$ ) compared to Field 1 and Field 3 ( $\approx 1''$ ). Thus, the spa-



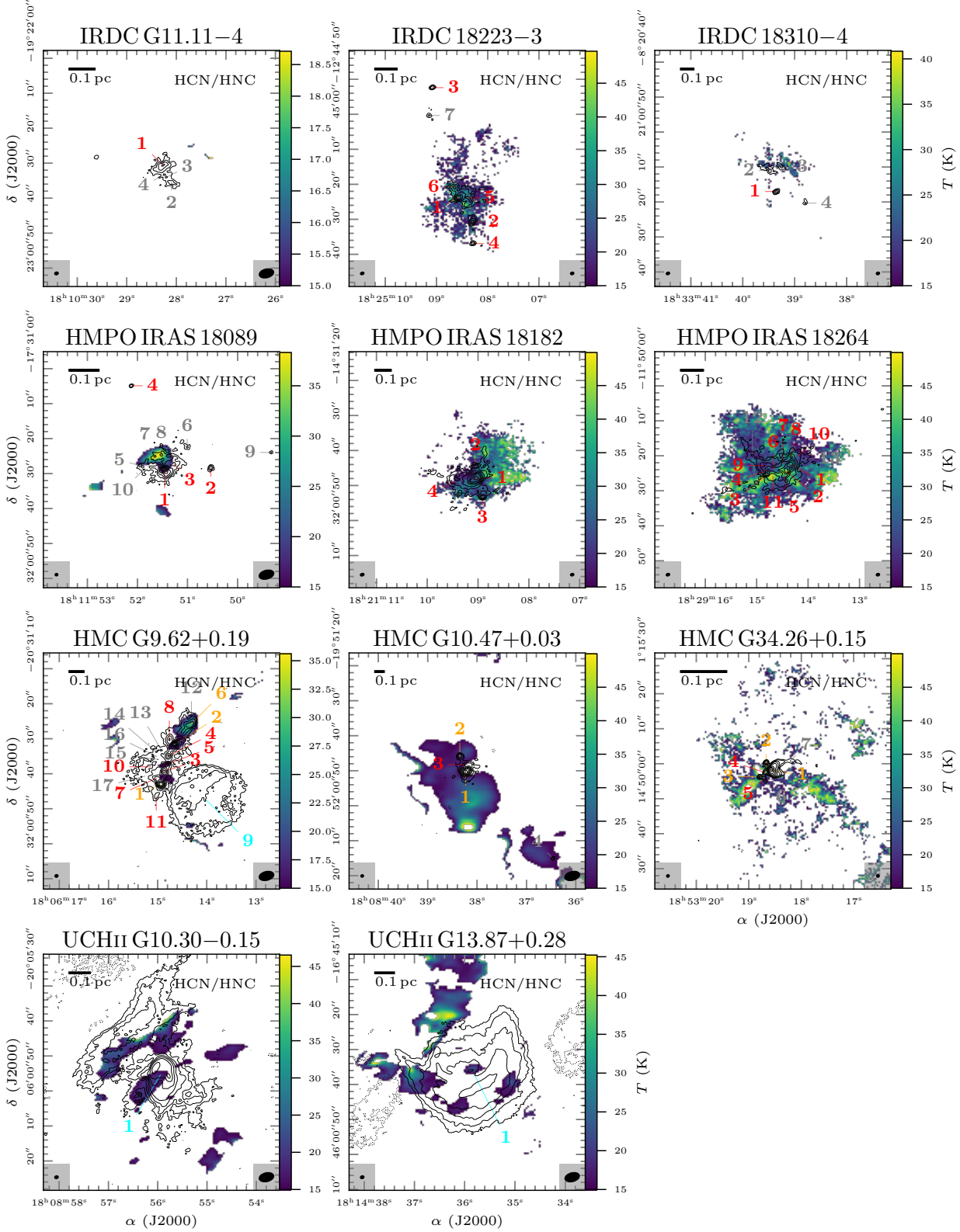


Fig. 3: Temperature maps derived with the HCN-to-HNC intensity ratio. In each panel, the temperature is shown in color and the 3 mm continuum in black contours. The dotted black contour marks the  $-5\sigma_{\text{cont}}$  level. The solid black contours start at  $5\sigma_{\text{cont}}$  and contour steps increase by a factor of 2 (e.g., 5, 10, 20,  $40\sigma_{\text{cont}}$ ). The synthesized beam size of the continuum and line data is shown in the bottom left and right corner, respectively. The continuum fragments are classified into dust cores (red), dust+ff cores (orange), cometary UCHII regions (cyan), further explained in Sect. 4.1. Fragments with  $S/N < 15$  are not analyzed in this study and are labeled in grey.

Table 5: Free-free contribution at 3 mm in the ALMA regions.

	$F_{3\text{mm}}$	$F_{\text{ff},3\text{mm}}$ (mJy)	$F_{\text{dust},3\text{mm}}$	$F_{\text{ff},3\text{mm}}/F_{3\text{mm}}$ (%)	classification
HMC G9.62+0.19 1	76.38	46.46	29.85	60.84	dust+ff core
HMC G9.62+0.19 2	14.23	2.92	11.31	20.51	dust+ff core
HMC G9.62+0.19 6	9.78	9.37	0.41	95.84	dust+ff core
HMC G9.62+0.19 9	177.23	158.8	18.21	89.6	cometary UCHII region
HMC G10.47+0.03 1	709.92	189.83	519.3	26.74	dust+ff core
HMC G10.47+0.03 2	8.98	8.21	0.62	91.34	dust+ff core
HMC G34.26+0.15 1	5276.23	3636.25	1639.98	68.92	dust+ff core
HMC G34.26+0.15 2	81.24	63.25	17.99	77.86	dust+ff core
HMC G34.26+0.15 3	43.44	38.69	4.75	89.07	dust+ff core
UCHII G10.30-0.15 1	452.35	389.58	59.7	86.12	cometary UCHII region
UCHII G13.87+0.28 1	481.71	355.29	112.71	73.76	cometary UCHII region

**Notes.** The free-free emission is estimated using the H(40) $\alpha$  recombination line (Fig. D.2).

tial scales that are traced by the ALMA observations in these molecular tracers are larger for regions in Field 2.

### 5.1. HCN-to-HNC intensity ratio

Hacar et al. (2020) find an empirical relation between the gas temperature and the HCN-to-HNC line integrated intensity ratio  $\frac{I(\text{HCN})}{I(\text{HNC})}$ . The authors used IRAM 30m observations of the 1 – 0 transition of HCN and HNC and compared the line integrated intensity ratios with kinetic temperature estimates derived from NH<sub>3</sub> observations. The empirical relation derived by Hacar et al. (2020) follows:

$$T = 10 \times \frac{I(\text{HCN})}{I(\text{HNC})} \quad \text{if } \frac{I(\text{HCN})}{I(\text{HNC})} \leq 4$$

$$T = 3 \times \left( \frac{I(\text{HCN})}{I(\text{HNC})} - 4 \right) + 40 \quad \text{if } \frac{I(\text{HCN})}{I(\text{HNC})} > 4. \quad (4)$$

Our observational setup covers the 1 – 0 transition of HCN and HNC (Table 3) and therefore we use this approach to estimate the kinetic temperature of the extended low-density and low-temperature gas, where no CH<sub>3</sub>CN line emission is detected. The HCN and HNC line data products are summarized in Table 4. For both molecules, the integrated intensity is computed from  $v_{\text{LSR}} - 30 \text{ km s}^{-1}$  to  $v_{\text{LSR}} + 30 \text{ km s}^{-1}$ . The noise in the integrated intensity maps is estimated from  $\sigma_{\text{line}}$  (Table 4) and the number of channels  $n_{\text{channel}}$ :  $\sigma_{\text{int.intensity}} = \sqrt{n_{\text{channel}}} \times \sigma_{\text{line}} \times \delta v$ , with  $\delta v = 0.8 \text{ km s}^{-1}$ . All pixels with a  $S/N < 3$  in the integrated intensity map are masked. Since the HCN line is in SPR1 and HNC in SPR3, for which all regions in Field 2 (Table 1) have a poorer resolution of  $\approx 3''$ , we imaged the HCN spectral line data using the same baselines as the HNC spectral line data (Sect. 3.1). The temperature is calculated according to Eq. (4) from the HCN-to-HNC intensity ratio. We further mask all pixels with  $T_{\text{kin}} < 15 \text{ K}$  and  $T_{\text{kin}} > 50 \text{ K}$ .

The temperature maps derived with the HCN-to-HNC intensity ratio are presented in Fig. 3. In many cases (IRDC 18223-3, HMPO IRAS 18182, HMPO IRAS 18264, HMC G10.47+0.03), the temperature maps are extended due to HCN and HNC emitting strong along large spatial scales. In IRDC G11.11-4, we are not able to estimate the temperature using this method since the derived temperatures are  $< 15 \text{ K}$ , that is the lower limit for which the HCN-to-HNC intensity ratio is valid (Hacar et al. 2020). In IRDC 18310-4, a temperature can only be estimated in the outskirts of core 2 and 3. In HMPO IRAS 18089, an enhanced

temperature is found toward the northern part of mm 1 towards position 7 and 8. This feature can be connected to the north-south outflow (Beuther et al. 2004). Broad line wings of bipolar outflows can affect the line integrated intensities (e.g., toward HMC G34.26+0.15). In HMPO IRAS 18182 a large scale E-W temperature gradient can be observed. The UCHII region at position HMC G9.62+0.19 6 heats up the environment with elevated temperatures in the surrounding envelope. In HMC G10.47+0.03 a clump with enhanced temperatures is found  $\approx 15''$  south of the continuum peak position.

Since this method is only valid from  $\approx 15 \text{ K}$  up to  $\approx 50 \text{ K}$  (Hacar et al. 2020) and the HCN and HNC lines can become optically thick in the densest regions, we use CH<sub>3</sub>CN and CH<sub>3</sub><sup>13</sup>CN in the next section to probe the temperature in the high-density and high-temperature regions.

### 5.2. Methyl cyanide

Gieser et al. (2021) model CH<sub>3</sub>CN line emission to infer the temperature structure in the CORE sample using the radiative transfer tool XCLASS (Möller et al. 2017). While the CORE 1 mm spectral setup covered the CH<sub>3</sub>CN  $J = 12 - 11 \text{ K}$ -ladder ( $E_{\text{u}}/k_{\text{B}} = 69 - 530 \text{ K}$ ), in the ALMA 3 mm setup the  $J = 5 - 4$  transitions are covered ( $E_{\text{u}}/k_{\text{B}} = 13 - 130 \text{ K}$  for CH<sub>3</sub>CN and CH<sub>3</sub><sup>13</sup>CN, Table 3). Extended CH<sub>3</sub><sup>13</sup>CN emission is only detected toward the three HMCs and HMPO IRAS 18089, and due to a high optical depth of the main isotopologue, CH<sub>3</sub><sup>13</sup>CN can thus more reliably trace the temperature of denser inner regions.

With myXCLASSmapfit, we fit all pixels with a peak intensity  $> 5\sigma_{\text{line}}$  in the spectrum (Table 4) using CH<sub>3</sub>CN for all 11 regions and CH<sub>3</sub><sup>13</sup>CN for the four regions in which significant emission is detected. Each parameter range (rotation temperature  $T_{\text{rot}}$ , column density  $N$ , source size  $\theta_{\text{Source}}$ , line width  $\Delta v$ , and velocity offset  $v_{\text{off}}$ ) is adjusted for each region and molecule, since the sample covers a broad range of densities and temperatures. We therefore iteratively adjust the parameter ranges that result in relatively smooth parameter maps without too many outliers due to unreliable fits. When many lines are optically thick, the algorithm converges to high temperatures (Gieser et al. 2021), we therefore set the highest possible temperature to 250 K. To trace hotter gas layers, observations of CH<sub>3</sub>CN and CH<sub>3</sub><sup>13</sup>CN transitions with higher upper energy levels are required.

The temperature maps of CH<sub>3</sub>CN and CH<sub>3</sub><sup>13</sup>CN are presented in Figs. 4 and 5, respectively. Toward the likely youngest region in our sample, IRDC 18310-4, CH<sub>3</sub>CN is not detected.

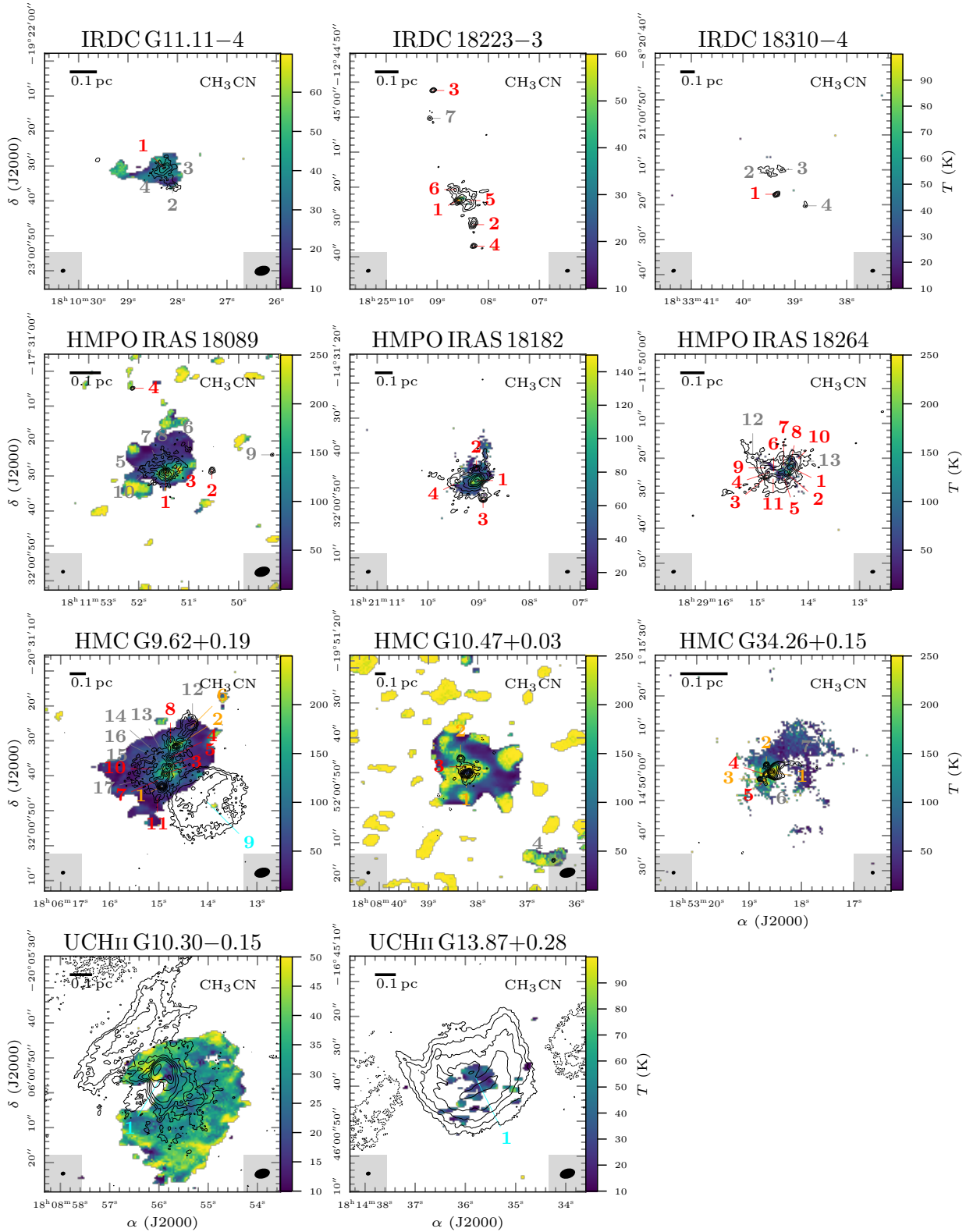


Fig. 4: Temperature maps derived with  $\text{CH}_3\text{CN}$ . In each panel, the temperature is shown in color and the 3 mm continuum in black contours. The dotted black contour marks the  $-5\sigma_{\text{cont}}$  level. The solid black contours start at  $5\sigma_{\text{cont}}$  and contour steps increase by a factor of 2 (e.g., 5, 10, 20,  $40\sigma_{\text{cont}}$ ). The synthesized beam size of the continuum and spectral line data are shown in the bottom left and right corner, respectively. The continuum fragments are classified into dust cores (red), dust+ff cores (orange), cometary UCHII regions (cyan), further explained in Sect. 4.1. Fragments with  $S/N < 15$  are not analyzed in this study and are labeled in grey. The clumpy features surrounding HMPO IRAS 18089 and HMC G10.47+0.03 are caused by side lobes.

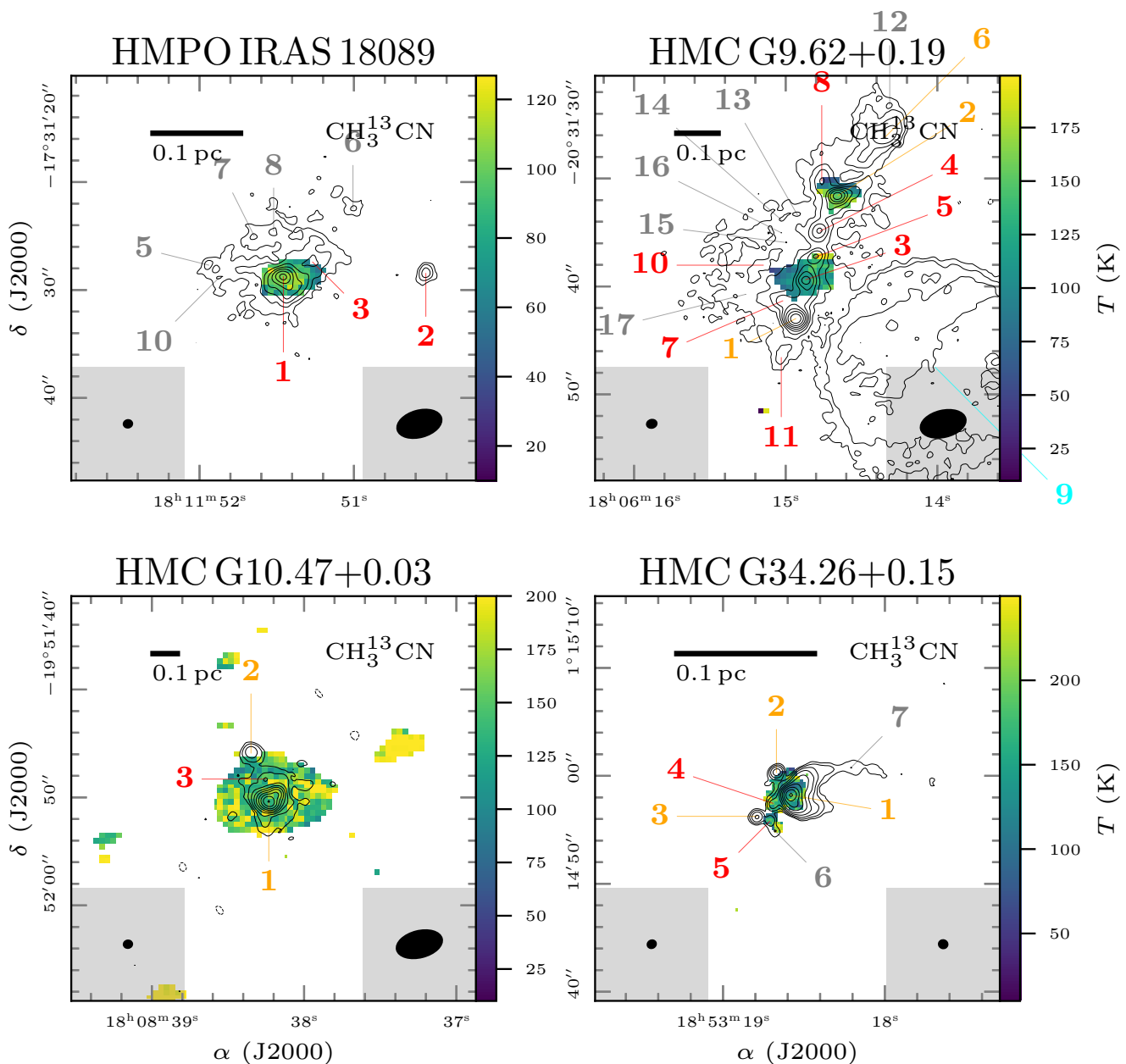


Fig. 5: Temperature maps derived with  $\text{CH}_3^{13}\text{CN}$ . In each panel, the temperature is shown in color and the 3 mm continuum in black contours. The dotted black contour marks the  $-5\sigma_{\text{cont}}$  level. The solid black contours start at  $5\sigma_{\text{cont}}$  and contour steps increase by a factor of 2 (e.g., 5, 10, 20,  $40\sigma_{\text{cont}}$ ). The synthesized beam size of the continuum and spectral line data are shown in the bottom left and right corner, respectively. The continuum fragments are classified into dust cores (red), dust+ff cores (orange), cometary UCHII regions (cyan), further explained in Sect. 4.1. Fragments with  $S/N < 15$  are not analyzed in this study and are labeled in grey.

In IRDC 18223–3, the temperature can only be estimated toward the 3 mm continuum peak position. In IRDC G11.11–4, the  $\text{CH}_3\text{CN}$  emission is already more extended with  $T \approx 50$  K. From the IRDCs to the HMCs, the peak temperature is clearly increasing up to  $\approx 250$  K (that is the upper limit set in XCLASS). Bright  $\text{CH}_3\text{CN}$  emission in HMPO IRAS 18089 and HMC G10.47+0.03 causes strong side lobes which can be seen as artifacts toward the edges surrounding the central region. A temperature plateau is reached toward the continuum peak positions in the HMCs, and in these cases  $\text{CH}_3^{13}\text{CN}$  is a better temperature probe.  $\text{CH}_3^{13}\text{CN}$  is less extended, but clearly traces high

temperatures  $> 150$  K in the four regions with detected  $\text{CH}_3^{13}\text{CN}$  emission. The cometary UCHII region in HMC G9.62+0.19 (source 9) produces a temperature increase of  $\approx 150$  K toward the edge of the filament which otherwise has a lower temperature of  $\approx 50$  K in the envelope.

The temperature map of UCHII G10.30–0.15 is very extended toward the west, and no  $\text{CH}_3\text{CN}$  is detected toward the east facing the bipolar HII region. In UCHII G13.87+0.28 the temperature map is less extended with  $\text{CH}_3\text{CN}$  being present in the cometary halo. In both UCHII regions, the kinetic temperature is very low, with  $T < 50$  K. There are two possible explana-



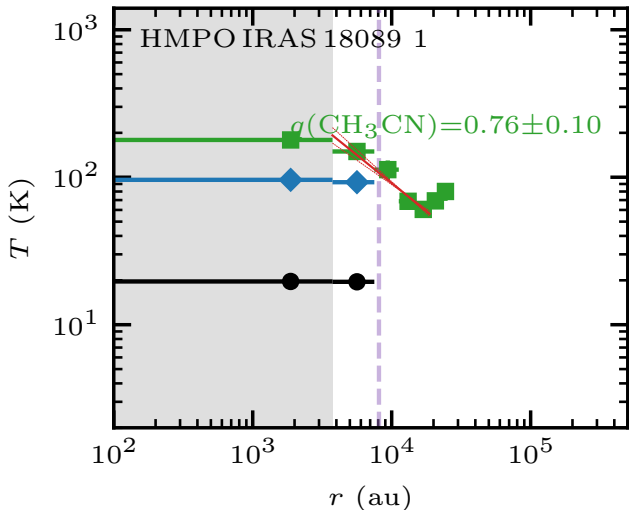


Fig. 6: Radial temperature profile of dust core 1 in HMPO IRAS 18089. The profiles extracted from the HCN-to-HNC intensity ratio (Fig. 3), CH<sub>3</sub>CN (Fig. 4), and CH<sub>3</sub><sup>13</sup>CN (Fig. 5) temperature maps are shown by black circles, green squares, and blue diamonds, respectively. The inner unresolved region (one beam radius) is shown as a grey-shaded area. The dashed purple vertical line indicates the outer radius  $r_{\text{out}}$  based on the continuum (Table C.1). A power-law fit and its  $1\sigma$  uncertainty to resolved and radially decreasing profiles is shown by the red solid and dashed lines, respectively (Sect. 5.3). The figures for the remaining sources are shown in Fig. C.1.

tions for such a low temperature: either CH<sub>3</sub>CN is present in the cold gas envelope or the line emission is produced by non-LTE effects. However, since the HCN-to-HNC intensity ratio method also infers temperatures  $\lesssim 50$  K, the first explanation seems to be more likely. Therefore, the extended molecular emission in the cometary UCHII regions seems to stem from an envelope that either stayed cold during the evolution of the protostars or is cooling due to the expanding UCHII region.

### 5.3. Radial temperature profiles

The temperature maps created with the HCN-to-HNC intensity ratio, CH<sub>3</sub>CN, and CH<sub>3</sub><sup>13</sup>CN allow us to derive radial temperature profiles of the protostellar sources. The radial temperature profiles are approximated by a power-law profile with temperature power-law index  $q$ ,  $T \sim r^{-q}$  (Eq. 1). For each of the protostellar sources and temperature tracers, the azimuthal-averaged temperature profile is calculated along seven beams, that is sufficient to fully resolve the radial profiles, starting at the continuum peak position of the source (Table C.1). The temperature profiles are binned in steps of half the synthesized beam size.

In order to derive the radial temperature profile, we fit a power-law profile (Eq. 1) to continuous profiles that are resolved along at least two beams and that are radially decreasing. In the fitting, we exclude the innermost data point that is smeared out by the limiting beam size (highlighted as a gray shaded area in Fig. 6) if more than three radial steps are otherwise available for a fit. The profiles are fitted as long as continuous data points are available and as long as the profiles are not increasing with increasing radius along radial steps. The fit results including the inner radius  $r_{\text{in}}$ , temperature  $T_{\text{in}} = T(r_{\text{in}})$ , and temperature power-

law index  $q$  are summarized in Table C.2. The radial temperature profile of the dust core HMPO IRAS 18089 1 is shown in Fig. 6 and in Fig. C.1 for all remaining protostellar sources that could be fitted by a power-law profile.

The temperature profiles derived from the HCN-to-HNC intensity ratio tracing the colder envelope are flat  $q \approx 0.1 - 0.3$ , while the CH<sub>3</sub>CN profiles tracing the hotter gas can be steeper with values ranging between  $q \approx 0.1 - 0.8$ . The temperature profiles are steep  $q > 0.5$  toward sources that are in the HMC regions, but also already toward dust cores in HMPO regions (dust cores 1 and 3 in HMPO IRAS 18089, dust core 1 in HMPO IRAS 18182). The observed CH<sub>3</sub><sup>13</sup>CN radial profiles (five sources in total) are either not resolved or flat and are therefore not fitted. With HCN and HNC we therefore trace the temperature of the colder larger scale envelope where the cores are embedded in, while high-density tracers such as CH<sub>3</sub>CN can be used to infer the temperature of the protostellar core.

The beam-averaged temperature  $\bar{T}$  for all three tracers is computed for all sources from the temperature maps (Figs. 3, 4, and 5) in order to estimate the H<sub>2</sub> column density and mass (Sect. 7). The results of the beam-averaged temperatures are summarized in Table C.3. By constraint, the HCN-to-HNC intensity ratio only traces temperatures up to 50 K, in addition, the low upper energy level ( $E_u/k_B = 4$  K) of the HCN and HNC emission line is only sensitive to the colder envelope and might become optically thick toward the denser regions. Therefore, the temperatures might be considerably lower compared to the temperatures derived with CH<sub>3</sub>CN and CH<sub>3</sub><sup>13</sup>CN. In most cases, the CH<sub>3</sub><sup>13</sup>CN beam-averaged temperature is lower than the CH<sub>3</sub>CN beam-averaged temperature. This can be attributed to the fact that if most CH<sub>3</sub>CN transitions become optically thick, the fitting algorithm in XCLASS converges toward the upper limit of the rotation temperature that we set to 250 K. A similar effect was found for the CORE sample, where in regions with a high H<sub>2</sub>CO line optical depth, the derived H<sub>2</sub>CO rotation temperature is higher than the CH<sub>3</sub>CN rotation temperature (Gieser et al. 2021). In Sect. 8 we discuss evolutionary trends of the temperature profiles and compare the results with the CORE and CORE-extension regions (Gieser et al. 2021, 2022).

A high line optical depth of the CH<sub>3</sub>CN lines causes XCLASS to converge to 250 K, that is the set upper limit (Sect. 5.2). This regime is reached toward the inner regions of dust+ff cores 1 in HMC G10.47+0.03 and HMC G34.26+0.15 (Fig. 4). However, since the CH<sub>3</sub>CN emission is extended, more data points in the optically thin regime are available for a reliable radial temperature profile fit (Fig. C.1).

## 6. Density profiles

In this section, we derive radial density profiles of the protostellar sources using the 3 mm continuum data. Interferometric observations filter out extended emission and missing flux can therefore be an issue. The radial density profile with power-law index  $p$  (Eq. 2) can be best estimated from the continuum data in the  $uv$  plane (e.g., Adams 1991; Looney et al. 2003; Zhang et al. 2009; Beuther et al. 2007b) considering the visibility and temperature power-law indices,  $\alpha$  and  $q$ , with

$$\alpha = p + q - 3. \quad (5)$$

Since bright nearby sources can affect the visibility profiles of individual fragmented sources, we first subtract the emission of other dust and/or dust+ff cores (Sect. 6.1) and then compute and fit the complex-averaged visibility profiles  $\bar{V}$  (Sect. 6.2).

### 6.1. Source subtraction

For each dust and/or dust+ff core, we subtract the emission of the remaining dust and/or dust+ff cores within a region by modeling their emission with a circular Gaussian profile using the task `uvmodel fit` in CASA.

The source model is Fourier-transformed to the  $uv$  plane with the `ft` task in CASA and subtracted from the data using the `uvsub` task in CASA. Source subtraction is only necessary when multiple dust and/or dust+ff cores are present within one region, therefore this step is not necessary for IRDC G11.11–4, IRDC 18310–4, UCH<sub>II</sub> G10.30–0.15, and UCH<sub>II</sub> G13.87+0.28 (Fig. 2 and Table C). Since HMC G9.62+0.19 9 is an extended cometary UCH<sub>II</sub> region (Fig. 2) with a complex morphology and cannot be described by a simple model, we refrain from modeling and subtracting the emission of this source. For the remaining regions, we carefully check by imaging the source-subtracted data that the emission of each source is approximately removed without over-subtracting the emission and does not affect the emission of nearby sources. Since most of the sources are embedded in fainter extended envelopes, it is not possible to completely model and remove the emission of those extended envelopes by a simple Gaussian model. However, with imaging the core-subtracted data we ensure that the bright source emission is subtracted well.

As an example, before computing the visibility profile of dust core 2 in HMPO IRAS 18182, we subtract the emission of the remaining dust cores 1, 3, and 4. One caveat is that the continuum data of the dust+ff cores and cometary UCH<sub>II</sub> regions contain not only dust, but also extended free-free emission (Sect. 4.2) that might have an impact on the derived density profile.

### 6.2. Visibility profiles

The complex-averaged visibility profiles  $\bar{V}$  as a function of  $uv$  distance are computed using the `plotms` task in CASA. The phase center is shifted to the corresponding source position (Table C.4). For a comparison of how the subtraction of the remaining cores in the region is impacting the visibility profiles, we also compute the complex-averaged visibility profiles  $\bar{V}$  using the original 3 mm continuum data, i.e. with no source subtraction.

Since the number of long baselines is much smaller than the number of short baselines, the visibility profiles are binned with bin sizes of 3, 15, and 60  $k\lambda$  in the ranges of 0 – 15, 15 – 120, and 120 – 470  $k\lambda$ , respectively. Since the shortest baseline corresponds to  $\approx 2.3 k\lambda$ , the first binned data point (0 – 3  $k\lambda$ ) is expected to suffer from missing flux. The visibility profile of dust+ff core 2 in HMC G9.62+0.19 is shown in Fig. 7 as an example and in Fig. C.2 for all remaining protostellar sources.

In contrast to the CORE and CORE-extension cores (Gieser et al. 2021, 2022) which all have visibility profiles that can be described by a single power-law profile,  $\bar{V} \sim s^\alpha$ , most of the sources in this ALMA sample are better described by two power-law profiles with with slope  $\alpha_1$ , at short baselines (large spatial scales), and with slope  $\alpha_2$ , at longer baselines (small spatial scales). We therefore fit two power-law profiles with  $\alpha_1$  and  $\alpha_2$  to the observed binned visibility profiles. The breakpoint between the two slopes is determined using the `pwlf` python package that allows a continuous piecewise linear function to be fitted to the logarithmic visibility profiles. In order to avoid a breakpoint at the shortest and longest  $uv$ -distances where only a few data points would be available, the breakpoint is allowed to be between 10  $k\lambda$  and 100  $k\lambda$ . The slopes  $\alpha_1$  and  $\alpha_2$  roughly correspond to clump ( $>0.1 pc$ ) and core ( $<0.1 pc$ ) scales, respectively.

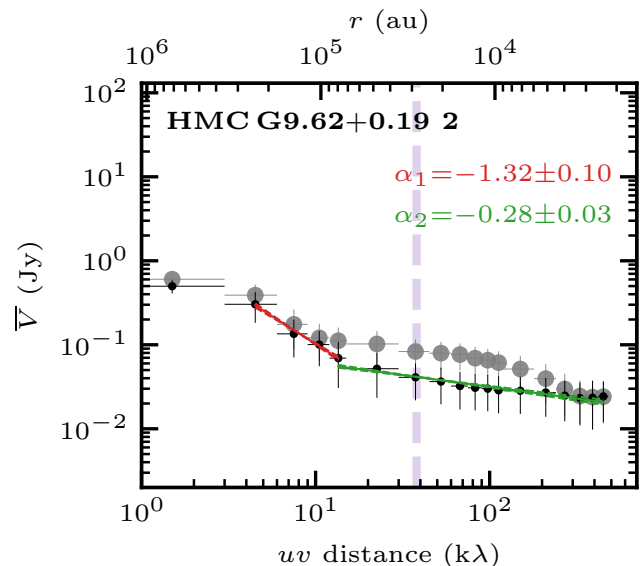


Fig. 7: Visibility profile of dust+ff core 2 in HMC G9.62+0.19. The profile of the non-core-subtracted and core-subtracted data is shown in grey and black, respectively (further explained in Sect. 6.1). Two power-law profiles, tracing roughly the clump and core scales, are fitted to the core-subtracted data shown in red and green, respectively. The bottom axis shows the  $uv$  distance in  $k\lambda$  and the top axis is the corresponding spatial scale. The purple dashed line indicates the source diameter (Table C.1). The figures for the remaining sources are shown in Fig. C.2.

The first binned data point, suffering from missing flux, is not included in the fit. The corresponding density profiles are calculated according to Eq. (5) using the temperature power-law index  $q$  measured toward each source (Table C.2). The results for  $\alpha_1$ ,  $\alpha_2$ ,  $p_1$ , and  $p_2$  are summarized in Table C.4.

Potential reasons for the presence of two power-law profiles in the ALMA data, compared to one power-law profile in the NOEMA data are discussed in more detail in Sect. 8.2. The most likely reason is that at the longer  $uv$ -distances, ALMA has a higher sensitivity due to the array consisting of more antennas with longer baselines compared to NOEMA. We therefore can more easily identify several power-law profiles in the ALMA data.

In Figs. 7 and C.2 it is clearly visible that the source subtraction can have a big impact on the visibility profiles when bright sources are located within a single region (e.g., for sources in the HMC G9.62+0.19 and HMC G34.26+0.15 regions). Toward sources in bright regions (HMC G10.47+0.03 and HMC G34.26+0.15), the visibility profiles flatten at short  $uv$  distances. A possible explanation could be the presence of free-free emission. However, this would imply extended free-free emission, while we find that the free-free contribution is concentrated toward the sources and is not extended (Fig. D.2). A physical explanation could be that the envelope is disrupted by the protostars themselves or by neighboring sources resulting in a steep density profile and thus a flat visibility profile at short  $uv$ -distances.

In a few regions, a significant contribution of free-free emission is present at 3 mm wavelengths as evaluated in Sect. 4.2 (Table 5). As an example, for UCH<sub>II</sub> G10.30–0.15 and UCH<sub>II</sub> G13.87+0.28 the free-free contribution is greater than

80%. In these cases, the visibility profiles are a composite of dust and free-free emission, while in the calculation of the density power-law index optically thin dust emission is assumed (Sect. 7).

When multiple sources are present within one region (e.g., IRDC 18223–3 and HMPO IRAS 18182), the visibility slope at clump scales ( $\alpha_1$ ) are similar (Table C.4). This can be explained by the fact that at small baselines, the cores are all covered by such short baselines (and corresponding larger angular resolution) and even though the phase center is shifted to the source position, it does not impact the clump scale in which the cores are embedded in. Except for the sources with a flattening at small  $uv$  distances, there is a trend such that the visibility profiles  $\alpha_1$ , corresponding to the large scale structures, steepen from the IRDC to UCHII regions implying a flattening of the density profile  $p_1$ .

The visibility slope at the smaller core scales ( $\alpha_2$ ) are nearly flat,  $\alpha_2 \approx 0$ , implying unresolved sources in the IRDC stages and become then also steeper, with a slope up to  $\alpha_2 \approx -1.0$ . A detailed discussion of the physical structure and evolutionary trends is presented in Sect. 8.

## 7. Molecular hydrogen column density and mass estimates

The  $H_2$  column density  $N(H_2)$  and mass  $M$  of the sources can be estimated from the 3 mm continuum emission according to

$$N(H_2) = \int n(H_2) ds = \frac{F_\nu^{\text{peak}} \eta}{\mu m_H \Omega_A \kappa_\nu B_\nu(T)}, \quad (6)$$

and

$$M = \frac{F_\nu \eta d^2}{\kappa_\nu B_\nu(T)}, \quad (7)$$

with the assumption that the emission stems from dust and is optically thin. Therefore, for the dust+ff cores and cometary UCHII regions that all have free-free emission at 3 mm, we correct the peak intensity  $I_{3\text{mm}}$  and integrated flux  $F_{3\text{mm}}$  by the fraction of estimated free-free emission listed in Table 5. For the temperature, we assume either the beam-averaged temperature  $\bar{T}$  based on the  $CH_3^{13}CN$  temperature maps if detected,  $CH_3CN$  if otherwise detected, and HCN-to-HNC intensity ratio otherwise (Table C.3). We use the same values for the following parameters as for the CORE and CORE-extension regions (Gieser et al. 2021, 2022) with gas-to-dust mass ratio  $\eta = 150$  (Draine 2011) and mean molecular weight  $\mu = 2.8$  (Kauffmann et al. 2008). The dust opacity is extrapolated from 1.3 mm ( $\kappa_0 = 0.9 \text{ g cm}^{-2}$ , Ossenkopf & Henning 1994) to 3 mm wavelengths with  $\kappa_\nu = \kappa_0 \left(\frac{\nu}{\nu_0}\right)^\beta$ , resulting in  $\kappa_\nu = 0.12 \text{ g cm}^{-2}$  assuming  $\beta = 2$ .

The results for  $N(H_2)$  and  $M$  are summarized in Table C.3. The optical depth  $\tau_\nu^{\text{cont}}$  calculated according to

$$\tau_\nu^{\text{cont}} = -\ln\left(1 - \frac{I_\nu}{B_\nu(T)}\right), \quad (8)$$

is also listed in Table C.3. Since the properties are derived from interferometric observations, the results are lower limits due to potential missing flux (Sect. 3.1). For HMC G34.26+0.15 1, the optical depth cannot be estimated since the numerator is larger than the denominator in Eq. (8), most likely because we overestimate the 3 mm dust emission as discussed in Sect. 4.2, and therefore the optical depth is estimated to be high. In addition,

for dust+ff core 1 in HMC G10.47+0.03, the optical depth becomes high as well,  $\tau_\nu^{\text{cont}} = 0.5$ . For the remaining sources, the optical depth  $\tau_\nu^{\text{cont}}$  is much smaller than 1. Indeed, the brightness temperatures are high toward the continuum peak position in HMC G10.47+0.03 and HMC G34.26+0.15 with  $T_B \approx 40 \text{ K}$  and  $T_B \approx 300 \text{ K}$ , respectively, while for the remaining regions  $T_B < 10 \text{ K}$  holds.

The  $H_2$  column densities vary between  $1 \times 10^{23} \text{ cm}^{-2}$  and  $2 \times 10^{26} \text{ cm}^{-2}$  and the masses range between  $0.1 M_\odot$  and  $150 M_\odot$ . While the estimated core masses are below  $8 M_\odot$  for most cores, all regions are embedded within massive clumps of at least  $1000 M_\odot$  (Table 1). The estimated core masses, based on the interferometric observations, are lower limits since the extended emission is filtered out. Thus, considering mass estimates on the core and clump scales, and taking into account the high bolometric luminosities (Table 1), suggests that the regions are forming massive stars. However, not all of the cores will be massive enough to host a high-mass star ( $M_* > 8 M_\odot$ ). The highest mass is found toward HMC G10.47+0.03 1 with  $M \approx 150 M_\odot$ . Cesaroni et al. (2010) detect three sources toward this position at 1.6 cm with the VLA at a higher angular resolution of  $0.''1$ . This indicates that this region is currently forming a compact cluster of massive stars.

## 8. Discussion

In this study, we characterized the physical properties toward a sample of 11 HMSFRs observed with ALMA based on the 3 mm continuum and spectral line emission. The 3 mm continuum data reveal a high degree of fragmentation (Fig. 2) and fragmented objects, identified using `cumpfind` (Williams et al. 2004), are classified into dust cores (compact 3 mm emission), dust+ff cores (with compact 3 mm emission, H(40) $\alpha$ , and cm emission), and cometary UCHII regions (with extended 3 mm emission, H(40) $\alpha$ , and cm emission), summarized in Table C.1. Cores with  $S/N < 15$  were not analyzed in this study due to insufficient sensitivity and angular resolution.

In Sect. 8.1, the region properties (peak intensity  $I_{3\text{mm}}^{\text{region}}$  and flux density  $F_{3\text{mm}}^{\text{region}}$ ) derived with the ALMA observations are compared to the large scale clump properties derived from the ATLASGAL survey (Urquhart et al. 2018, 2022). In Sect. 8.2 the evolutionary trends of the physical properties on core scales are discussed and compared with the results of the CORE (Gieser et al. 2021) and CORE-extension (Gieser et al. 2022) studies.

### 8.1. Evolutionary trends of the clump properties

All regions in our ALMA sample are also covered by the ATLASGAL survey (Schuller et al. 2009) targeting dust emission on clump scales in the Galactic plane. The  $870 \mu\text{m}$  images are presented in the top right panel in Figs. B.1 – B.11. The clump sizes cover roughly the FOV of the ALMA 3 mm observations, we therefore compare in this section the ATLASGAL clump properties with the ALMA 3 mm peak intensity  $I_{3\text{mm}}^{\text{region}}$  and flux density  $F_{3\text{mm}}^{\text{region}}$  of each region.

The distance  $d$ , luminosity  $L$ , mass  $M$ , and dust temperature  $T_{\text{dust}}$  are taken from the ATLASGAL study by Urquhart et al. (2018) and are listed in Table 1. The clump distances  $d$  are estimated using different methods, including maser parallaxes and kinematic distances based on radial velocities. The luminosity, mass, and dust temperature are derived by fitting the SED using additional MIR and FIR data from, for example, the Galactic Legacy Infrared Mid-Plane Survey Extraordinaire (GLIMPSE,



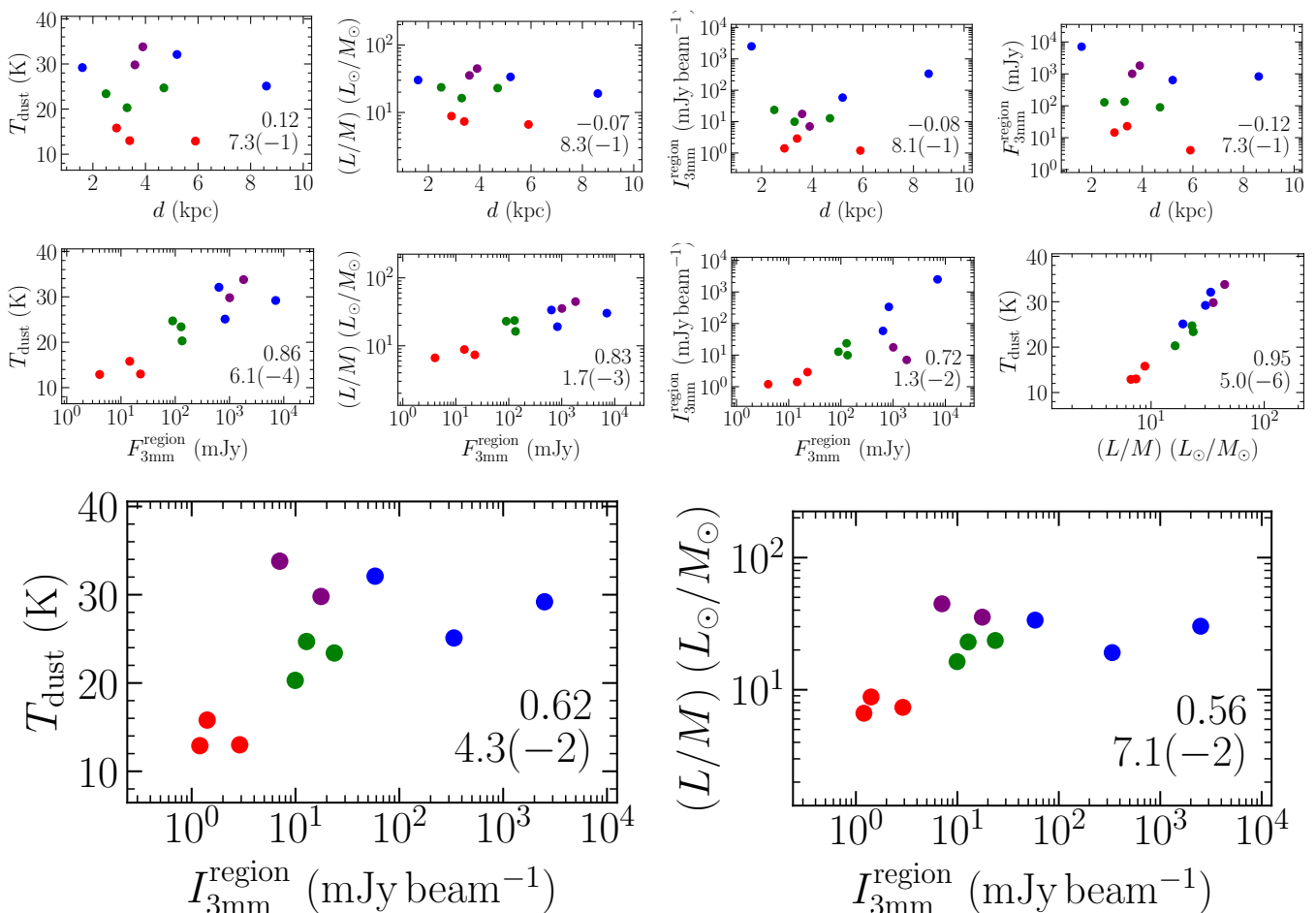


Fig. 8: Comparison of the clump parameters of the regions. The temperature  $T_{\text{dust}}$ , luminosity  $L$ , mass  $M$ , and distance  $d$  are listed in Table 1 and are taken from the ATLASGAL survey (Schuller et al. 2009; Urquhart et al. 2018). The region peak intensity  $I_{3\text{mm}}^{\text{region}}$  and flux density  $F_{3\text{mm}}^{\text{region}}$  of the ALMA 3 mm continuum data is listed in Table 2. The colors of the data points highlight the four evolutionary stages (red: IRDC, green: HMPO, blue: HMC, and purple: UCHII region). The Spearman correlation coefficient  $r_s$  and  $p$ -value, with a(b) meaning  $a \times 10^b$ , are shown in the bottom right corner.

Benjamin et al. 2003), the MIPS GALactic plane survey (MIPSGAL, Carey et al. 2009), and the *Herschel* infrared GALactic plane survey (Hi-GAL Molinari et al. 2010). The CORE and CORE-extension regions are not covered by ATLASGAL and therefore a consistent method that could derive these parameters is not available. We therefore do not include the clump properties of CORE and CORE-extension in this analysis.

The ALMA 3 mm peak intensity  $I_{3\text{mm}}^{\text{region}}$  and flux density  $F_{3\text{mm}}^{\text{region}}$  are listed in Table 2. The flux density is integrated considering the area with emission  $>5\sigma_{\text{cont}}$ . In contrast to the single-dish observations with *Spitzer*, *Herschel*, and APEX telescopes used for the SED fit in Urquhart et al. (2018), the interferometric ALMA observations suffer from spatial filtering (on scales larger than  $>60''$ , Sect. 3.1) that can be an issue especially for the extended UCHII regions that have widespread emission within the full ALMA primary beam (Fig. 2). In addition to dust emission, at 3 mm wavelengths there is a contribution from free-free emission toward evolved protostars in the HMC and UCHII regions (Sect. 4.2).

In Fig. 8 relations between the following clump parameters are presented:  $d$ ,  $L/M$ ,  $T_{\text{dust}}$ ,  $I_{3\text{mm}}^{\text{region}}$ , and  $F_{3\text{mm}}^{\text{region}}$ . The  $L/M$  ratio is an indicator of evolutionary stage increasing from IRDC to

UCHII regions (e.g., Sridharan et al. 2002; Molinari et al. 2008, 2010; Maud et al. 2015; Molinari et al. 2016; Urquhart et al. 2018; Molinari et al. 2019). In color, the different evolutionary stages (IRDC - HMPO - HMC - UCHII) based on the classification by Gerner et al. (2014, 2015) are highlighted. In order to quantify potential correlations, we use the Spearman correlation coefficient  $r_s$ , that is zero for uncorrelated data and  $\pm 1$  for correlated and anticorrelated data, respectively (Cohen 1988). The  $p$ -value indicates the probability that an uncorrelated data set would have with this Spearman correlation coefficient value. The Spearman correlation coefficient  $r_s$  and  $p$ -value are shown in Fig. 8 for each parameter pair.

The top row in Fig. 8 shows the relation of the properties as a function of distance  $d$ . With  $|r_s| < 0.12$  for all parameters,  $T_{\text{dust}}$ ,  $L/M$ ,  $I_{3\text{mm}}^{\text{region}}$ , and  $F_{3\text{mm}}^{\text{region}}$  are not correlated with distance  $d$ . This implies that our sample is not biased by distance such that more luminous regions would be at larger distances. However, there are clear evolutionary trends, highlighted in different colors, for  $T_{\text{dust}}$ ,  $L/M$ , and  $F_{3\text{mm}}^{\text{region}}$ , with these values increasing with evolutionary stage, but independent of distance. For example, the dust temperature  $T_{\text{dust}}$  increases from  $\approx 15$  K (IRDCs),  $\approx 20$  K (HMPOs),  $\approx 30$  K (HMCs and UCHII regions). For the peak inten-



sity  $I_{3\text{mm}}^{\text{region}}$ , this trend is seen from the IRDC to the HMC stages, while for the UCH<sub>II</sub> regions, the peak intensity  $I_{3\text{mm}}^{\text{region}}$  decreases compared to the HMC stage. Since both UCH<sub>II</sub> regions have a cometary morphology with extended emission (Fig. 2), the decrease of  $I_{3\text{mm}}^{\text{region}}$  compared to previous evolutionary stages can be explained by the expanding envelope driven by the central protostar resulting in a lower surface brightness. In addition, the material is continuously fed onto the central protostar, while at the same time matter is expelled through the outflow.

For the remaining parameter pairs (excluding the distance  $d$ ), we find positive correlations with  $r_S \geq 0.56$  (all panels in the second and third row in Fig. 8), with  $T_{\text{dust}}$ ,  $L/M$ , and  $F_{3\text{mm}}^{\text{region}}$  increasing with evolutionary stage.

Urquhart et al. (2022) investigated the evolutionary trends of  $\approx 5\,000$  ATLASGAL clumps using a slightly different evolutionary scheme (quiescent - protostellar - YSO - H<sub>II</sub> region). The clumps were visually classified based on additional MIR and FIR data from GLIMPSE, MIPS GAL, and Hi-GAL. For example, quiescent clumps have no counterpart at wavelengths of  $70\ \mu\text{m}$  and below, while YSOs have  $70\ \mu\text{m}$ ,  $24\ \mu\text{m}$  and  $4 - 8\ \mu\text{m}$  counterparts, but show no cm emission. Based on the cumulative distribution of  $T_{\text{dust}}$  and  $L/M$ , Urquhart et al. (2022) also find that these parameters increase with evolutionary stage.

Despite the fact that the sample analyzed in this work covers only 11 HMSFRs compared to, for example, the  $\approx 10\,000$  clumps studied in the ATLASGAL survey, we still cover a broad range in clump properties as shown in Fig. 8. The four evolutionary stages form relatively distinct regions in these correlation plots, and in the next section we will investigate if and how the physical properties in HMSFRs correlate on smaller core scales, such as the temperature and density profiles, and mass. Since a high degree of fragmentation is observed in this sample (Fig. 2 and Table C.1), it is expected that the evolutionary trends become less prominent due to multiple protostars, potentially at different evolutionary stages, present within a single clump.

## 8.2. Evolutionary trends on core scales

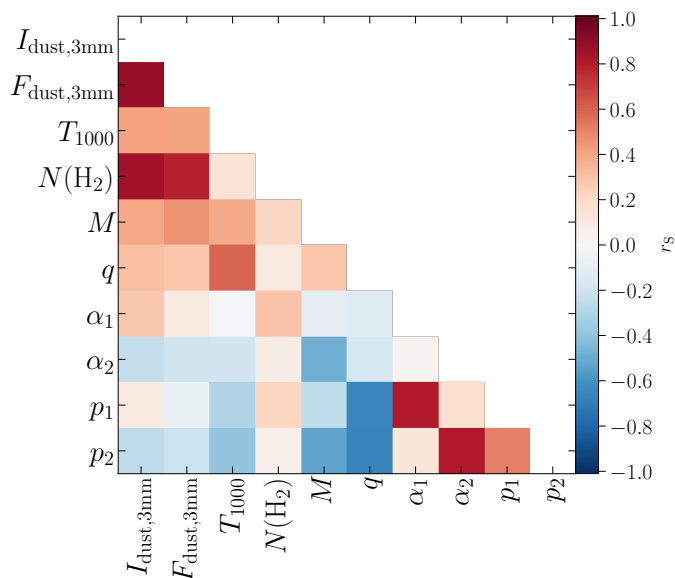


Fig. 9: Correlations of the physical parameters of the ALMA, CORE, and CORE-extension samples.

In this section, we analyze relations between physical properties on the smaller core scales, i.e., the physical structure of the dust cores, dust+ff cores, and cometary UCH<sub>II</sub> regions of the sample analyzed in this study and the cores of the CORE and CORE-extension sample (Gieser et al. 2021, 2022). Following the nomenclature of this study, the cores in the CORE and CORE-extension studies can be classified as dust cores. We focus on the following physical properties that were derived in all three studies.

The 3 mm peak intensity  $I_{\text{dust},3\text{mm}}$  and integrated flux density  $F_{\text{dust},3\text{mm}}$  of the dust emission are estimated from the continuum data. For the regions observed with ALMA at 3 mm, we use the free-free corrected 3 mm continuum data (Sect. 4.2). For the CORE and CORE-extension sample, we extrapolate the 1 mm peak intensity and flux density to 3 mm wavelengths assuming black body emission with  $I_\nu \sim \nu^2$  and  $F_\nu \sim \nu^2$ . The masses  $M$  and  $\text{H}_2$  column density  $N(\text{H}_2)$  were calculated in all studies according to Eq. 7 and 6, respectively.

In order to account for the fact that the regions are at various distances and were observed at slightly different angular resolutions, we extrapolate the radial temperature profiles to a common radius of  $1\,000\ \text{au}$ ,  $T_{1000} = T(r=1\,000\ \text{au})$ . The radial temperature profiles were taken from the  $\text{H}_2\text{CO}$ ,  $\text{CH}_3\text{CN}$ , and  $\text{CH}_3^{13}\text{CN}$  temperature maps derived with XCLASS or the temperature map derived using the HCN-to-HNC intensity ratio (Hacar et al. 2020).

The observed temperature power-law index  $q$  is derived from the radial temperature profiles and the visibility power-law index  $\alpha$  is estimated from the continuum visibility profiles. Since we find that most of the ALMA sources are best fitted by two power-law profiles,  $\alpha_1$  and  $\alpha_2$ , we assume  $\alpha_1 = \alpha_2 = \alpha$  for the CORE and CORE-extension dust cores and check for correlations for both profiles separately. The indices  $\alpha_1$  and  $\alpha_2$  roughly correspond to the clump and core scales, respectively (Sect. 6).

The density profiles  $p_1$  and  $p_2$  are calculated according to Eq. (5) using  $\alpha_1$  and  $\alpha_2$ , respectively. We use for each source the observed temperature power-law index  $q$ . Therefore, we have two density power-law indices,  $p_1$  and  $p_2$  tracing the clump and core scales, respectively. For the dust cores in the CORE and CORE extension sample  $p_1 = p_2$  holds.

In total, a complete set of these physical parameters can be derived for 56 protostellar sources: 22 dust cores in the CORE sample (Gieser et al. 2021); 5 dust cores in the CORE-extension sample (Gieser et al. 2022); and 22 dust cores, 6 dust+ff cores and 1 cometary UCH<sub>II</sub> region in this study. To investigate potential correlations between pairs of these parameters, we compute the Spearman correlation coefficient. Figure 9 summarizes the Spearman correlation coefficient for all parameter pairs. While for some parameters, e.g.,  $\alpha_1$  and  $M$ , we do not find hints for potential correlations, other parameters show clear correlations, e.g.,  $q$  and  $T_{1000}$ . Thus in Fig. 10 the parameter pairs with  $|r_S| > 0.5$  are shown, indicating weak ( $|r_S| \approx 0.5$ ) to high (anti)correlations ( $|r_S| = 1.0$ ), and in the following we focus on the discussion of these parameter pairs. Different colors in Fig. 10 highlight the different evolutionary stages based on the larger clump scales (IRDC - HMPO - HMC - UCH<sub>II</sub>). We group the dust cores CORE-extension and CORE regions into the IRDC and HMPO stage, respectively (Gieser et al. 2021, 2022).

We find positive correlations of  $I_{\text{dust},3\text{mm}}$  with  $F_{\text{dust},3\text{mm}}$  and  $N(\text{H}_2)$ . The integrated flux density  $F_{\text{dust},3\text{mm}}$  is positively correlated with  $N(\text{H}_2)$ . Evolutionary trends for these parameters are clearly seen from dust cores in IRDCs to the dust+ff cores in HMCs. The peak intensity is lower for the cometary UCH<sub>II</sub> region compared to the other sources. From dust+ff cores to

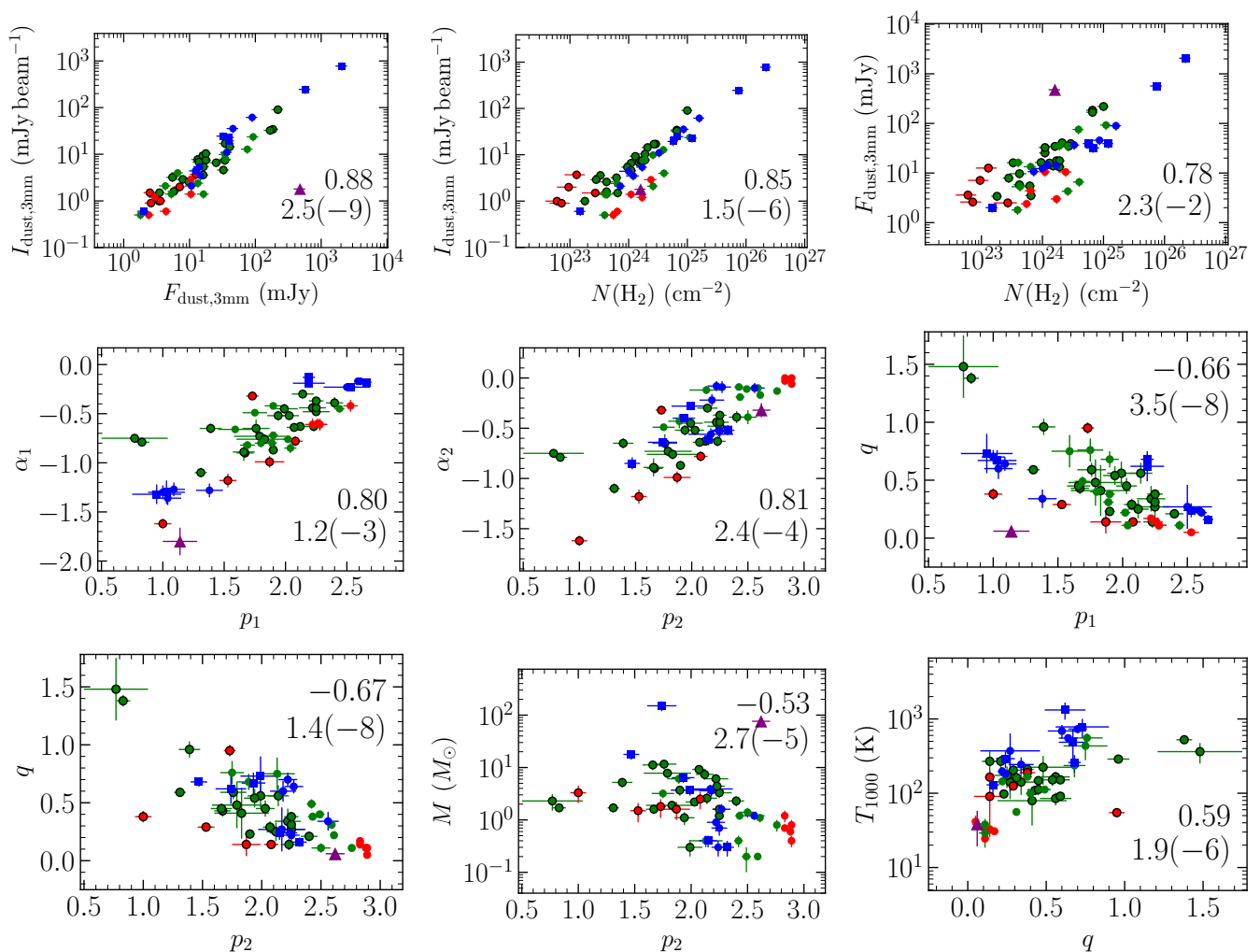


Fig. 10: Correlations with  $|r_s| > 0.5$  of the physical parameters of the ALMA, CORE, and CORE-extension sample. The color of the data points highlight the four evolutionary stages (red: IRDC, green: HMPO, blue: HMC, and purple: UCHII region). The data points of the cores of the CORE (green) and CORE-extension (red) sample are enclosed in black rings. The dust cores, dust+ff cores and cometary UCHII regions are shown by circles, squares and triangles, respectively. The Spearman correlation coefficient  $r_s$  and  $p$ -value, with a(b) meaning  $a \times 10^b$ , are shown in each panel.

cometary UCHII regions, the dust peak intensity decreases significantly. This can be explained by the fact that the protostellar radiation disrupts the surrounding gas and dust envelope. The surface brightness (corresponding to the intensity) is therefore decreasing as well and since the dust is slowly expelled into the more diffuse ISM, the flux density within our limited sensitivity decreases as well. Regarding the estimated temperatures, the central protostar in the cometary UCHII region is expected to be much hotter than the  $\approx 36$  K estimated with the extended CH<sub>3</sub>CN line emission (Table C.2).

With the observed CH<sub>3</sub>CN and CH<sub>3</sub><sup>13</sup>CN emission lines and angular resolution, gas layers up to 200 – 250 K can be traced, however, higher J-transitions are required to constrain the temperature profiles in higher density regions. In addition, the angular resolution and line sensitivity only allows for the radial temperature profiles to be only marginally resolved, typically only along 2 – 3 beams, that are challenging to reliably fit (Figs. 6 and C.1).

The positive correlation between the pair of  $\alpha_1$  and  $p_1$  and of  $\alpha_2$  and  $p_2$  is due to the fact that  $p$  is calculated taking into account  $\alpha$  in Eq. (5). If these flat visibility slopes, with  $\alpha_1 > -0.3$ ,

are not considered, there is a clear trend such that the density profile on clump scales,  $p_1$ , flattens from the dust cores in IRDCs ( $p_1 \approx 2.2$ ) to dust+ff cores in HMCs ( $p_1 \approx 1.2$ ). This can be explained by the fact that steep density profiles are expected for collapsing and accreting clumps, while feedback of the massive stars disrupts the surrounding envelope, e.g. due to powerful outflows or an expanding UCHII region. This flattening of the density power-law index on clump scales has also been observed by Beuther et al. (2002a) where their “strong molecular sources” have  $p \approx 1.9$  and their more evolved “cm sources” have  $p \approx 1.5$ . We do not find strong evidence for evolutionary trends of the density profile on the core scales,  $p_2$ . Most of the objects seem to be collapsing and accreting toward the gravitational center and thus toward  $p_2 \approx 2$  a high density of data points of cores of dust and dust+ff cores is found, but overall there is a large scatter from 1.0 to 2.5 (excluding the unresolved dust cores in the IRDCs with  $\alpha_2 \approx 0$ ). The presence of compact free-free emission at 3 mm wavelengths can impact the visibility profiles and thus also the derived density profile. It is therefore necessary to analyze the density profile on core scales in an even larger sample, preferentially at shorter wavelengths, where the contribution

of free-free emission is less severe, e.g. with the ALMAGAL project that targets  $\approx 1\,000$  HMSFRs in a similar spectral setup as CORE.

The observed temperature power-law index  $q$  is anticorrelated with the density power-law indices  $p_1$  and  $p_2$ . There is a clear evolutionary trend such that the temperature profiles steepens from the IRDC ( $q \approx 0.1$ ) to the UCHII regions ( $q \approx 0.7$ ), while for the cometary UCHII region the profile becomes flat. This suggests that an embedded source is steadily heating up the envelope. This is also confirmed by the fact that the slope  $q$  becomes steeper with  $T_{1000}$  increasing from 20 K up to 1 000 K. The cometary UCHII region has a low value of  $T_{1000}$  ( $\approx 30$  K). An increase of the temperature power-law index  $q$  compared to the typical value of 0.3–0.4 has been observed toward several HMCs in the literature (Beltrán et al. 2018; Mottram et al. 2020). We also find in the analysis of the 22 cores of the CORE sample, that the distribution of  $q$  has a spread (Gieser et al. 2021). The four data points with  $q > 0.9$  are most likely outliers due to unreliable fits. In the HMC models by Nomura & Millar (2004) and Osorio et al. (2009), in which the temperature profile is calculated self-consistently, the temperature profiles also steepen on core scales with  $q > 0.4$ .

An unexpected result of the density profile analysis is that for most of the sources, we find that the visibility profiles follow at least two power-law profiles (Sect. 6), while for the CORE and CORE-extension samples, a single power-law profile was sufficient (Gieser et al. 2021, 2022). The traced spatial scales of NOEMA and ALMA observations are not too different (2 – 500 k $\lambda$  and 10 – 600 k $\lambda$ , respectively), but NOEMA has less long baselines resulting in higher noise at long baselines in the visibility profiles (Gieser et al. 2021, 2022) compared to ALMA (Fig. 7). To test if the two power-law slopes are an effect of observed wavelength (1 mm versus 3 mm), we aim to obtain additional 3 mm observations of the CORE sample. A pilot study toward the IRAS 23385, IRAS 23033 and NGC7538S CORE regions will investigate the differences between the 1 mm and 3 mm data (Gieser et al. in prep.). The fact that the sources in the ALMA regions show two power-law slopes can be explained by the young cores in the IRDCs containing unresolved point sources. In an inside-out collapse picture, the cores grow in mass and size, and the density profile of the cores in the HMPOs aligns with the underlying clump density profile. In these cases, a single visibility power-law profile is observed, in our cases for the CORE sample (Gieser et al. 2021) and for dust core 1 in HMPO IRAS 18089 (Fig. C.2) for which we also find  $\alpha_1 = \alpha_2$ .

We find evolutionary trends on core scales, but there are clear overlaps in contrast to the larger scale clump properties discussed in Sect. 8.1. In our analysis of the physical properties, we assume that the envelopes are spherically symmetric, however, the presence of outflows and the inclination might also impact, for example, the temperature and density profiles. High angular resolution data of HMSFRs clearly show that a single classification of the evolutionary stage based on the clump properties is not sufficient to describe the evolutionary phases of protostellar sources embedded within a single clump. We therefore aim to use in a future study the physical-chemical model MUSCLE (Gerner et al. 2014, 2015) to derive chemical timescales,  $\tau_{\text{chem}}$ , in combination with MIR, FIR, and cm data in order to better characterize and classify individual protostellar sources on core scales in clustered HMSFRs.

## 9. Summary and conclusions

In this study we analyzed ALMA 3 mm continuum and line observations of 11 high-mass star-forming regions at evolutionary stages from protostars in young infrared dark clouds to evolved UCHII regions. In addition, we made use of archival data at MIR, FIR, and cm wavelengths in order to characterize the regions along different wavelengths. In particular, we made use of the H(40) $\alpha$  recombination line to distinguish between dust and free-free emission in the ALMA 3 mm continuum data.

At an angular resolution of  $\approx 1''$ , we observe a high degree of fragmentation in the regions and the fragmentation was quantified using the `cLumpfind` algorithm. We classify the fragments into protostellar sources with  $S/N > 15$ , while cores with  $S/N < 15$  are not further analyzed. The protostellar sources are divided further into dust cores (compact mm emission originating from dust), dust+ff cores (compact mm and additional H(40) $\alpha$  and cm emission) and cometary UCHII regions (extended mm and additional H(40) $\alpha$  and cm emission) for which we detect 37, 8, and 3 sources, respectively. In our analysis, we exclude 24 cores due to insufficient sensitivity and/or angular resolution. Our findings are summarized as follows:

1. We create temperature maps using the HCN-to-HNC intensity ratio to trace the low-temperature regime and with XCLASS we model and fit CH<sub>3</sub>CN and CH<sub>3</sub><sup>13</sup>CN line emission to trace the high-temperature regime. Radial temperature profiles with power-law index  $q$  (Eq. 1) are computed for all protostellar sources. We find that there is a spread in  $q$  between  $\approx 0.1 - 0.7$ .
2. The density profiles (Eq. 2) are estimated from the 3 mm continuum visibility profiles. In contrast to the CORE and CORE-extension regions (Gieser et al. 2021, 2022), most of the visibility profiles are best explained by two profiles with varying slope  $\alpha_1$  and  $\alpha_2$  instead of a single profile. The visibility slopes  $\alpha_1$  and  $\alpha_2$  approximately trace the clump and core scales, respectively. The estimated density power-law index  $p_1$  and  $p_2$  (Eq. 5) varies between 1 and 2.6, and 1.6 and 3, respectively.
3. Using the peak intensity  $I_{\text{dust},3\text{mm}}$  and integrated flux density  $F_{\text{dust},3\text{mm}}$  of the 3 mm dust, we estimate the mass and H<sub>2</sub> column density of the protostellar sources. We find a large spread in H<sub>2</sub> column density,  $N(\text{H}_2) \approx 10^{23} - 10^{26} \text{ cm}^{-2}$ , and mass,  $M \approx 0.1 - 150 M_{\odot}$ , within the protostellar sources.
4. Comparing the 3 mm peak intensity and region-integrated flux density ( $I_{3\text{mm}}^{\text{region}}$  and  $F_{3\text{mm}}^{\text{region}}$ ) with clump properties ( $T_{\text{dust}}$ ,  $L/M$ ) derived by the ATLASGAL survey (Urquhart et al. 2018), we find that there are clear evolutionary trends of  $T_{\text{dust}}$ ,  $L/M$ , and  $F_{3\text{mm}}^{\text{region}}$  increasing from IRDC to UCHII regions. The peak intensity  $I_{3\text{mm}}^{\text{region}}$  is increasing from the IRDC to HMC stage and then significantly decreases in the UCHII regions. This can be explained by the fact that the expanding extended envelope has a low surface brightness compared to compact cores in the IRDC to HMC stages. Even though our sample consists of only 11 regions, we still cover a broad range in physical properties on clump scales.
5. We combined the results of the physical structure on core scales derived in this study with the results of the CORE and CORE extension sample (Gieser et al. 2021, 2022) and analyzed a sample of a total of 56 protostellar sources for correlations and evolutionary trends. We find that the temperature at a characteristic radius of 1 000 au,  $T_{1000}$ , is increasing with evolutionary stage and at the same time, the temperature power-law index  $q$  steepens from  $q \approx 0.1$  to  $q \approx 0.7$



from dust cores in IRDCs to dust+ff cores in HMCs. The density profile  $p_1$  on clump scales, flattens from  $p_1 \approx 2.2$  in the IRDC stage to  $p_1 \approx 1.2$  in UCHII regions, while for the density profile  $p_2$  on core scales, we do not find evidence for evolutionary trends, with a mean of  $p \approx 2$  considering the full sample, but with an overall scatter from 1.0 to 2.5. These results provide invaluable observational constraints for physical models describing the formation of high-mass stars.

In this study, we focused on the characterization of the physical properties 11 regions observed with ALMA at high angular resolution. We now aim to further investigate the physical and chemical properties using the rich molecular line data covered by our ALMA observations (Table A.2) and apply the physical-chemical model MUSCLE (Gerner et al. 2014, 2015) to these regions in order to estimate chemical timescales  $\tau_{\text{chem}}$  of the protostellar sources (Gieser et al. 2021, 2022). With additional MIR, FIR, and cm data at high angular resolution, we aim to better characterize and classify the evolutionary stages on core scales, compared to larger clump scales, considering that multiple fragmented protostellar sources in different evolutionary phases are typically embedded within a single clump.

*Acknowledgements.* The authors would like to thank the anonymous referee whose comments helped improve the clarity of this paper. C.G. and H.B. acknowledge support from the European Research Council under the Horizon 2020 Framework Programme via the ERC Consolidator Grant CSF-648505. This paper makes use of the following ALMA data: ADS/JAO.ALMA#2018.1.00424.S ALMA is a partnership of ESO (representing its member states), NSF (USA) and NINS (Japan), together with NRC (Canada), MOST and ASIAA (Taiwan), and KASI (Republic of Korea), in cooperation with the Republic of Chile. The Joint ALMA Observatory is operated by ESO, AUI/NRAO and NAOJ. This research made use of Astropy<sup>1</sup>, a community-developed core Python package for Astronomy (Astropy Collaboration et al. 2013, 2018).

## References

Adams, F. C. 1991, *ApJ*, 382, 544  
 ALMA Partnership, Brogan, C. L., Pérez, L. M., et al. 2015, *ApJ*, 808, L3  
 Andrews, S. M., Huang, J., Pérez, L. M., et al. 2018, *ApJ*, 869, L41  
 Astropy Collaboration, Price-Whelan, A. M., Sipőcz, B. M., et al. 2018, *AJ*, 156, 123  
 Astropy Collaboration, Robitaille, T. P., Tollerud, E. J., et al. 2013, *A&A*, 558, A33  
 Avenhaus, H., Quanz, S. P., Garufi, A., et al. 2018, *ApJ*, 863, 44  
 Belloche, A., Müller, H. S. P., Menten, K. M., Schilke, P., & Comito, C. 2013, *A&A*, 559, A47  
 Beltrán, M. T., Cesaroni, R., Rivilla, V. M., et al. 2018, *A&A*, 615, A141  
 Beltrán, M. T. & de Wit, W. J. 2016, *A&A Rev.*, 24, 6  
 Benjamin, R. A., Churchwell, E., Babler, B. L., et al. 2003, *PASP*, 115, 953  
 Beuther, H., Churchwell, E. B., McKee, C. F., & Tan, J. C. 2007a, in *Protostars and Planets V*, ed. B. Reipurth, D. Jewitt, & K. Keil, 165  
 Beuther, H., Gieser, C., Suri, S., et al. 2021, *A&A*, 649, A113  
 Beuther, H., Henning, T., Linz, H., et al. 2015a, *A&A*, 581, A119  
 Beuther, H., Henning, T., Linz, H., et al. 2010, *A&A*, 518, L78  
 Beuther, H., Hunter, T. R., Zhang, Q., et al. 2004, *ApJ*, 616, L23  
 Beuther, H., Leurini, S., Schilke, P., et al. 2007b, *A&A*, 466, 1065  
 Beuther, H., Linz, H., Henning, T., et al. 2011, *A&A*, 531, A26  
 Beuther, H., Linz, H., Tackenberg, J., et al. 2013, *A&A*, 553, A115  
 Beuther, H., Mottram, J. C., Ahmadi, A., et al. 2018a, *A&A*, 617, A100  
 Beuther, H., Ragan, S. E., Johnston, K., et al. 2015b, *A&A*, 584, A67  
 Beuther, H., Schilke, P., Menten, K. M., et al. 2002a, *ApJ*, 566, 945  
 Beuther, H., Schilke, P., Sridharan, T. K., et al. 2002b, *A&A*, 383, 892  
 Beuther, H., Soler, J. D., Vlemmings, W., et al. 2018b, *A&A*, 614, A64  
 Beuther, H., Sridharan, T. K., & Saito, M. 2005a, *ApJ*, 634, L185  
 Beuther, H. & Steinacker, J. 2007, *ApJ*, 656, L85  
 Beuther, H., Walsh, A., Schilke, P., et al. 2002c, *A&A*, 390, 289  
 Beuther, H., Zhang, Q., Sridharan, T. K., & Chen, Y. 2005b, *ApJ*, 628, 800  
 Beuther, H., Zhang, Q., Sridharan, T. K., Lee, C. F., & Zapata, L. A. 2006, *A&A*, 454, 221

Bonnell, I. A. 2007, in *Astronomical Society of the Pacific Conference Series*, Vol. 367, *Massive Stars in Interactive Binaries*, ed. N. St.-Louis & A. F. J. Moffat, 303  
 Briggs, D. S. 1995, PhD thesis, New Mexico Institute of Mining and Technology  
 Bronfman, L., Nyman, L. A., & May, J. 1996, *A&AS*, 115, 81  
 Carey, S. J., Clark, F. O., Egan, M. P., et al. 1998, *ApJ*, 508, 721  
 Carey, S. J., Noriega-Crespo, A., Mizuno, D. R., et al. 2009, *PASP*, 121, 76  
 Cesaroni, R., Churchwell, E., Hofner, P., Walmsley, C. M., & Kurtz, S. 1994, *A&A*, 288, 903  
 Cesaroni, R., Felli, M., Testi, L., Walmsley, C. M., & Olmi, L. 1997, *A&A*, 325, 725  
 Cesaroni, R., Hofner, P., Araya, E., & Kurtz, S. 2010, *A&A*, 509, A50  
 Chen, X., Ellingsen, S. P., Shen, Z.-Q., Titmarsh, A., & Gan, C.-G. 2011, *ApJS*, 196, 9  
 Churchwell, E. 2002, *ARA&A*, 40, 27  
 Cohen, J. 1988, *Statistical Power Analysis for the Behavioral Sciences* (Lawrence Erlbaum Associates)  
 Condon, J. J. & Ransom, S. M. 2016, *Essential Radio Astronomy*  
 Cyganowski, C. J., Whitney, B. A., Holden, E., et al. 2008, *AJ*, 136, 2391  
 Deharveng, L., Zavagno, A., Samal, M. R., et al. 2015, *A&A*, 582, A1  
 Dewangan, L. K., Ojha, D. K., Zinchenko, I., & Baug, T. 2018, *ApJ*, 861, 19  
 Draine, B. T. 2011, *Physics of the Interstellar and Intergalactic Medium*  
 Duarte-Cabral, A., Bontemps, S., Motte, F., et al. 2013, *A&A*, 558, A125  
 Fallscheer, C., Beuther, H., Zhang, Q., Keto, E., & Sridharan, T. K. 2009, *A&A*, 504, 127  
 Garay, G. & Lizano, S. 1999, *PASP*, 111, 1049  
 Garay, G., Lizano, S., & Gomez, Y. 1994, *ApJ*, 429, 268  
 Gerner, T., Beuther, H., Semenov, D., et al. 2014, *A&A*, 563, A97  
 Gerner, T., Shirley, Y. L., Beuther, H., et al. 2015, *A&A*, 579, A80  
 Gieser, C., Beuther, H., Semenov, D., et al. 2021, *A&A*, 648, A66  
 Gieser, C., Beuther, H., Semenov, D., et al. 2022, *A&A*, 657, A3  
 Gieser, C., Semenov, D., Beuther, H., et al. 2019, *A&A*, 631, A142  
 Goedhart, S., Langa, M. C., Gaylard, M. J., & Van Der Walt, D. J. 2009, *MNRAS*, 398, 995  
 Gorai, P., Bhat, B., Sil, M., et al. 2020, *ApJ*, 895, 86  
 Hacar, A., Bosman, A. D., & van Dishoeck, E. F. 2020, *A&A*, 635, A4  
 Hajigholi, M., Persson, C. M., Wirstrom, E. S., et al. 2016, *A&A*, 585, A158  
 Hatchell, J., Thompson, M. A., Millar, T. J., & MacDonald, G. H. 1998, *A&AS*, 133, 29  
 Henning, T., Linz, H., Krause, O., et al. 2010, *A&A*, 518, L95  
 Herbst, E. & van Dishoeck, E. F. 2009, *ARA&A*, 47, 427  
 Hoare, M. G., Purcell, C. R., Churchwell, E. B., et al. 2012, *PASP*, 124, 939  
 Högbom, J. A. 1974, *A&AS*, 15, 417  
 Issac, N., Tej, A., Liu, T., et al. 2020, *MNRAS*, 497, 5454  
 Johnstone, D., Fiege, J. D., Redman, R. O., Feldman, P. A., & Carey, S. J. 2003, *ApJ*, 588, L37  
 Kauffmann, J., Bertoldi, F., Bourke, T. L., Evans, N. J., I., & Lee, C. W. 2008, *A&A*, 487, 993  
 Khan, S., Pandian, J. D., Lal, D. V., et al. 2022, *A&A*, 664, A140  
 Klaassen, P. D., Johnston, K. G., Urquhart, J. S., et al. 2018, *A&A*, 611, A99  
 Krumholz, M. R. 2015, in *Astrophysics and Space Science Library*, Vol. 412, *Very Massive Stars in the Local Universe*, ed. J. S. Vink, 43  
 Kuiper, R. & Hosokawa, T. 2018, *A&A*, 616, A101  
 Kumar, M. S. N., Palmeirim, P., Arzoumanian, D., & Inutsuka, S. I. 2020, *A&A*, 642, A87  
 Kurtz, S., Cesaroni, R., Churchwell, E., Hofner, P., & Walmsley, C. M. 2000, in *Protostars and Planets IV*, ed. V. Mannings, A. P. Boss, & S. S. Russell, 299–326  
 Lin, Y., Wyrowski, F., Liu, H. B., et al. 2022, *A&A*, 658, A128  
 Linz, H., Stecklum, B., Henning, T., Hofner, P., & Brandl, B. 2005, *A&A*, 429, 903  
 Liu, T., Evans, N. J., Kim, K.-T., et al. 2020, *MNRAS*, 496, 2790  
 Liu, T., Lacy, J., Li, P. S., et al. 2017, *ApJ*, 849, 25  
 Looney, L. W., Mundy, L. G., & Welch, W. J. 2003, *ApJ*, 592, 255  
 MacDonald, G. H., Gibb, A. G., Habing, R. J., & Millar, T. J. 1996, *A&AS*, 119, 333  
 Maud, L. T., Lumsden, S. L., Moore, T. J. T., et al. 2015, *MNRAS*, 452, 637  
 McKee, C. F. & Tan, J. C. 2002, *Nature*, 416, 59  
 McKee, C. F. & Tan, J. C. 2003, *ApJ*, 585, 850  
 Molinari, S., Balmeschi, A., Robitaille, T. P., et al. 2019, *MNRAS*, 486, 4508  
 Molinari, S., Merello, M., Elia, D., et al. 2016, *ApJ*, 826, L8  
 Molinari, S., Pezzuto, S., Cesaroni, R., et al. 2008, *A&A*, 481, 345  
 Molinari, S., Swinyard, B., Bally, J., et al. 2010, *PASP*, 122, 314  
 Möller, T., Endres, C., & Schilke, P. 2017, *A&A*, 598, A7  
 Mookerjee, B., Casper, E., Mundy, L. G., & Looney, L. W. 2007, *ApJ*, 659, 447  
 Morii, K., Sanhueza, P., Nakamura, F., et al. 2021, *ApJ*, 923, 147  
 Motte, F., Bontemps, S., & Louvet, F. 2018, *ARA&A*, 56, 41  
 Motte, F., Bontemps, S., Schilke, P., et al. 2007, *A&A*, 476, 1243  
 Mottram, J. C., Beuther, H., Ahmadi, A., et al. 2020, *A&A*, 636, A118  
 Mottram, J. C., Hoare, M. G., Davies, B., et al. 2011, *ApJ*, 730, L33

<sup>1</sup> <http://www.astropy.org>



- Müller, H. S. P., Schlöder, F., Stutzki, J., & Winnewisser, G. 2005, *Journal of Molecular Structure*, 742, 215
- Nomura, H. & Millar, T. J. 2004, *A&A*, 414, 409
- Öberg, K. I., Guzmán, V. V., Walsh, C., et al. 2021, *ApJS*, 257, 1
- Olimi, L., Cesaroni, R., & Walmsley, C. M. 1996, *A&A*, 307, 599
- Osorio, M., Anglada, G., Lizano, S., & D'Alessio, P. 2009, *ApJ*, 694, 29
- Osorio, M., Lizano, S., & D'Alessio, P. 1999, *ApJ*, 525, 808
- Ossenkopf, V. & Henning, T. 1994, *A&A*, 291, 943
- Palau, A., Estalella, R., Girart, J. M., et al. 2007, *A&A*, 465, 219
- Pascucci, I., Apai, D., Henning, T., Stecklum, B., & Brandl, B. 2004, *A&A*, 426, 523
- Peters, T., Mac Low, M.-M., Banerjee, R., Klessen, R. S., & Dullemond, C. P. 2010, *ApJ*, 719, 831
- Pickett, H. M., Poynter, R. L., Cohen, E. A., et al. 1998, *J. Quant. Spectr. Rad. Transf.*, 60, 883
- Pillai, T., Wyrowski, F., Menten, K. M., & Krügel, E. 2006, *A&A*, 447, 929
- Qin, S.-L., Wang, J.-J., Zhao, G., Miller, M., & Zhao, J.-H. 2008, *A&A*, 484, 361
- Ragan, S., Henning, T., Krause, O., et al. 2012, *A&A*, 547, A49
- Rathborne, J. M., Jackson, J. M., & Simon, R. 2006, *ApJ*, 641, 389
- Reid, M. J. & Ho, P. T. P. 1985, *ApJ*, 288, L17
- Rodón, J. A., Beuther, H., & Schilke, P. 2012, *A&A*, 545, A51
- Rolfs, R., Schilke, P., Zhang, Q., & Zapata, L. 2011, *A&A*, 536, A33
- Rosen, A. L., Offner, S. S. R., Sadavoy, S. I., et al. 2020, *Space Sci. Rev.*, 216, 62
- Rosero, V., Hofner, P., Claussen, M., et al. 2016, *ApJS*, 227, 25
- Rosero, V., Hofner, P., McCoy, M., et al. 2014, *ApJ*, 796, 130
- Sánchez-Monge, Á., Cesaroni, R., Beltrán, M. T., et al. 2013a, *A&A*, 552, L10
- Sánchez-Monge, Á., Kurtz, S., Palau, A., et al. 2013b, *ApJ*, 766, 114
- Sánchez-Monge, Á., Schilke, P., Schmiedeke, A., et al. 2017, *A&A*, 604, A6
- Sanhueza, P., Girart, J. M., Padovani, M., et al. 2021, *ApJ*, 915, L10
- Sanna, A., Moscadelli, L., Cesaroni, R., et al. 2010, *A&A*, 517, A71
- Schilke, P. 2015, in *EAS Publications Series*, Vol. 75-76, *EAS Publications Series*, 227–235
- Schuller, F., Menten, K. M., Contreras, Y., et al. 2009, *A&A*, 504, 415
- Smith, R. J., Longmore, S., & Bonnell, I. 2009, *MNRAS*, 400, 1775
- Soler, J. D., Beuther, H., Rugel, M., et al. 2019, *A&A*, 622, A166
- Sridharan, T. K., Beuther, H., Schilke, P., Menten, K. M., & Wyrowski, F. 2002, *ApJ*, 566, 931
- Tackenberg, J., Beuther, H., Henning, T., et al. 2014, *A&A*, 565, A101
- Tan, J. C., Beltrán, M. T., Caselli, P., et al. 2014, in *Protostars and Planets VI*, ed. H. Beuther, R. S. Klessen, C. P. Dullemond, & T. Henning, 149
- Testi, L., Felli, M., Persi, P., & Roth, M. 1998, *A&A*, 329, 233
- Thompson, M. A., Hatchell, J., Walsh, A. J., MacDonald, G. H., & Millar, T. J. 2006, *A&A*, 453, 1003
- Urquhart, J. S., König, C., Giannetti, A., et al. 2018, *MNRAS*, 473, 1059
- Urquhart, J. S., Wells, M. R. A., Pillai, T., et al. 2022, *MNRAS*, 510, 3389
- Walsh, A. J., Macdonald, G. H., Alvey, N. D. S., Burton, M. G., & Lee, J. K. 2003, *A&A*, 410, 597
- Wang, K., Zhang, Q., Testi, L., et al. 2014, *MNRAS*, 439, 3275
- Williams, J. P., de Geus, E. J., & Blitz, L. 1994, *ApJ*, 428, 693
- Williams, S. J., Fuller, G. A., & Sridharan, T. K. 2004, *A&A*, 417, 115
- Wood, D. O. S. & Churchwell, E. 1989, *ApJS*, 69, 831
- Xi, H., Zhou, J., Esimbek, J., et al. 2015, *MNRAS*, 453, 4203
- Zhang, Q., Wang, K., Lu, X., & Jiménez-Serra, I. 2015, *ApJ*, 804, 141
- Zhang, Q., Wang, Y., Pillai, T., & Rathborne, J. 2009, *ApJ*, 696, 268
- Zinnecker, H. & Yorke, H. W. 2007, *ARA&A*, 45, 481

## Appendix A: Summary of the ALMA observations

Tables A.1 and A.2 give an detailed overview of the ALMA 3 mm observations and spectral setup, respectively. The data calibration and imaging of this data set are explained in detail in Sect. 3.1.

## Appendix B: Overview of the sample

A multi-wavelength and multi-scale overview of the target regions are presented in Figs. B.1 - B.11 using archival VLA cm, ATLASGAL submm, *Herschel* FIR and *Spitzer* MIR data in comparison with the ALMA 3 mm observations. We note that mass and luminosity estimates in those descriptions might differ from the ATLASGAL results shown in Table 1, for example, due to a different assumed source distance.

### B.1. IRDC G11.11–4 (Fig. B.1)

The IRDC G11.11–4, also referred to as the “Snake”, is a filamentary cloud (Carey et al. 1998) that shows a spatial correlation between dust extinction maps and submm emission (Johnstone et al. 2003; Henning et al. 2010, see also Fig. B.1). Henning et al. (2010) detected 18 cores along the filament, two of them with masses  $>50 M_{\odot}$ . Wang et al. (2014) studied the hierarchical fragmentation from scales of 1 pc down to 0.01 pc in the filament and found chemical differentiation between fragmented cores indicating that the cores are at different evolutionary phases.

We observed with ALMA the region referred to as “P1” in the literature which already shows signatures of active star formation with  $8 \mu\text{m}$  emission, a molecular outflow (Johnstone et al. 2003), and the presence of  $\text{CH}_3\text{OH}$  and  $\text{H}_2\text{O}$  masers (Pillai et al. 2006). By modeling the SED of the dust continuum, Pillai et al. (2006) infer a luminosity of  $1200 L_{\odot}$  that is powered by a Zero Age Main Sequence (ZAMS) star of  $8 M_{\odot}$ . The authors infer an envelope mass and temperature of  $500 M_{\odot}$  and 19 K, respectively, and elevated temperatures around the protostar ( $\approx 60$  K). Rosero et al. (2014) detected radio continuum emission at 1.3 cm and 6 cm with the VLA which they attributed to a thermal ionized jet, while at 3 mm wavelengths the emission is dominated by dust.

### B.2. IRDC 18223–3 (Fig. B.2)

IRDC 18223–3 (“peak 3” studied by Beuther et al. 2002a) is located in the same filament as IRAS 18223–1243, an HII region (Bronfman et al. 1996) with bright radio continuum emission (Dewangan et al. 2018). Beuther et al. (2005a) studied the region with the Plateau de Bure Interferometer (PdBI) at 3 mm wavelengths, while no emission is detected at MIR wavelengths except for weak emission at  $4.5 \mu\text{m}$  around the source tracing shock-excited gas by an outflow. The fact that there is no MIR source detected in the *Spitzer* IRAC bands and only a small outflow mass of  $M_{\text{out}} = 3.4 M_{\odot}$  is estimated, the authors suspected that this source is a very young protostar before the HMPO phase.

Weak protostellar MIR emission became detectable with more sensitive *Spitzer* MIPS observations at 24 and  $70 \mu\text{m}$  (Beuther & Steinacker 2007). The authors fit the SED and find that most of the mass ( $M \approx 580 M_{\odot}$ ) is enclosed at low temperatures of  $T \approx 15$  K, while a small fraction ( $M \approx 0.01 M_{\odot}$ ) has elevated temperatures of  $T \geq 51$  K with a total luminosity of  $180 L_{\odot}$  and thus the source is expected to evolve into a high-

mass star. The outflow is directed from the northwest-southeast with a disk that is likely to be edge-on (Fallscheer et al. 2009).

Beuther et al. (2015b) studied the larger scale filament with PdBI mosaic observations and the authors detect 12 cores with a separation of 0.4 pc which is consistent with thermal Jeans fragmentation. However, a high mass-to-length ratio of  $\approx 1000 M_{\odot} \text{pc}^{-1}$  in the filament requires additional support against further collapse. The filament and its environment were studied by Dewangan et al. (2018) with  $^{13}\text{CO}$  line emission. The authors find two clouds at slightly different velocities at  $45 \text{ km s}^{-1}$  and  $51 \text{ km s}^{-1}$  that seem to be connected at the intermediate velocities suggesting that about 1 Myr ago a cloud-cloud collision could have occurred which could then have triggered the formation of high-mass stars.

### B.3. IRDC 18310–4 (Fig. B.3)

IRDC 18310–4 (“peak 4” in Beuther et al. 2002a) is located in the same filament as IRAS 18310–0825. The region, being dark up to 100  $\mu\text{m}$ , was a prestellar clump candidate with a mass reservoir of  $\approx 800 M_{\odot}$  without any signposts of active star formation (Beuther et al. 2013). The line width of  $\text{N}_2\text{H}^+$  decreases toward the center of the clump (Tackenberg et al. 2014).

Weak  $70 \mu\text{m}$  emission was detected toward one of the fragments (Beuther et al. 2015a) and the magnetic field is relatively weak ( $\approx 2.6$  mG) compared to more evolved HMPOs and HMCs (Beuther et al. 2018b). Recent ALMA observations revealed that among 11 cores with masses ranging from 1.1 to  $19 M_{\odot}$  at least four cores show outflows traced by CO and SiO emission such that star formation has been taking place for at least  $10^4$  yr (Morii et al. 2021).

### B.4. HMPO IRAS 18089 (Fig. B.4)

IRAS 18089–1732 is a massive HMPO with  $M \approx 2000 M_{\odot}$  with  $\text{H}_2\text{O}$  and  $\text{CH}_3\text{OH}$  maser emission (Beuther et al. 2004). The authors found a collimated north-south outflow revealed by SiO emission, while  $\text{CH}_3\text{OCHO}$  emission is confined to the central core region with a velocity gradient almost perpendicular to the outflow tracing the rotating envelope/disk structure. Sub-arcsecond resolution observations show that the core does not further fragment (Beuther et al. 2005b), however, the variability of  $\text{CH}_3\text{OH}$  maser emission with a period of  $\approx 30$  d could be explained by a binary system (Goedhart et al. 2009).

The rich molecular content and a temperature of 350 K derived with  $\text{CH}_3\text{CN}$  indicates that the central region has already formed a hot core in the inner region (Beuther et al. 2005b). Sanhueza et al. (2021) studied the region at 700 au scales with ALMA and find that the dust and magnetic field have spiral-like filamentary features and the  $\text{H}^{13}\text{CO}^+$  emission shows a complex velocity gradient suggesting that the filaments are rotating and infalling. An analysis of the energy budget shows that gravity is dominant over rotation, turbulence, and the magnetic field (Sanhueza et al. 2021). The authors estimate an infall rate of  $0.9 - 2.5 \times 10^{-4} M_{\odot} \text{yr}^{-1}$ .

### B.5. HMPO IRAS 18182 (Fig. B.5)

HMPO IRAS 18182 is a massive isolated core ( $M \approx 1500 M_{\odot}$  and  $L \approx 10^{4.3} L_{\odot}$ , Beuther et al. 2002a) with detected OH,  $\text{H}_2\text{O}$ , and  $\text{CH}_3\text{OH}$  maser emission (Sanna et al. 2010). Beuther et al. (2006) resolve no further fragmentation down to their angular resolution of  $3''$  and derive a temperature of 150 K in the cen-

Table A.1: Overview of the ALMA 3 mm observation blocks (Cycle 6, project code 2018.1.00424.S). The target regions were grouped into three fields in order to minimize off-source time (Table 2).

Field	SPR	Array configuration	Antennae	Date	On-source integration (min)	PWV (mm)	shortest baseline (m)	longest baseline (m)
Field 1	SPR1	C43-4	47	2018-10-28 21:06	20.4	1.3	15.1	1397.8
Field 1	SPR1	ACA	11	2018-12-28 18:08	48.6	6.0	8.9	48.9
Field 1	SPR2	C43-4	41	2018-12-15 19:34	26.6	4.1	15.1	740.4
Field 1	SPR2	ACA	10	2018-12-30 15:27	51.5	5.0	8.9	48.9
Field 1	SPR3	C43-4	48	2018-10-27 21:54	20.6	1.3	15.1	1397.8
Field 1	SPR3	ACA	11	2018-12-28 17:24	44.2	6.0	8.9	48.9
Field 2	SPR1	C43-4	46	2018-11-20 17:54	47.7	1.4	15.1	1397.8
Field 2	SPR1	C43-4	46	2018-11-20 18:42	48.6	1.5	15.1	1397.8
Field 2	SPR1	ACA	11	2019-05-10 09:30	84.2	5.0	8.9	48.0
Field 2	SPR1	ACA	11	2019-05-20 07:12	89.0	2.0	8.9	48.0
Field 2	SPR1	ACA	11	2019-05-23 07:36	83.8	1.0	8.9	48.0
Field 2	SPR2	C43-4	41	2019-05-03 11:22	55.8	1.0	15.1	740.4
Field 2	SPR2	ACA	11	2019-01-26 15:04	76.7	4.0	8.9	48.0
Field 2	SPR2	ACA	11	2019-03-29 08:16	83.2	5.0	8.9	48.0
Field 2	SPR2	ACA	11	2019-03-29 09:39	84.0	5.0	8.9	48.0
Field 2	SPR2	ACA	11	2019-03-29 11:06	54.6	5.0	8.9	48.0
Field 2	SPR3	C43-1	46	2019-01-10 18:20	41.3	2.4	15.1	313.7
Field 2	SPR3	ACA	11	2019-05-20 08:41	83.7	2.0	8.9	48.0
Field 2	SPR3	ACA	11	2019-05-23 08:59	83.4	1.0	8.9	48.0
Field 3	SPR1	C43-4	46	2018-11-16 21:38	43.6	2.0	15.1	1397.8
Field 3	SPR1	C43-4	46	2018-11-19 20:31	44.3	1.9	15.1	1397.8
Field 3	SPR1	ACA	11	2019-01-16 13:15	74.8	5.0	8.9	48.9
Field 3	SPR1	ACA	12	2019-01-17 12:35	78.6	5.0	8.9	48.9
Field 3	SPR2	C43-4	41	2019-04-17 11:20	61.8	3.3	15.0	783.5
Field 3	SPR2	ACA	10	2019-04-01 12:04	87.0	4.0	8.9	48.9
Field 3	SPR2	ACA	10	2019-04-17 12:17	86.9	3.0	8.9	44.7
Field 3	SPR3	C43-4	47	2018-10-30 22:39	50.2	1.4	15.1	1397.8
Field 3	SPR3	ACA	11	2019-01-16 14:43	74.9	5.0	8.9	48.9
Field 3	SPR3	ACA	11	2019-01-19 14:25	74.9	5.0	8.9	48.9

tral region using CH<sub>3</sub>CN line emission. The authors find that the outflow has a quadrupolar morphology and that the molecular emission peaks 1–2'' off from the continuum peak position. With multi-epoch CH<sub>3</sub>OH maser observations, [Sanna et al. \(2010\)](#) estimate that the central object has a mass of 35  $M_{\odot}$  assuming that the emission stems from a rotating disk.

### B.6. HMPO IRAS 18264 (Fig. B.6)

IRAS 18264 is an extended green object (EGO) with widespread emission in 4.5  $\mu\text{m}$  *Spitzer* data that rises from shocked H<sub>2</sub> gas in the outflow ([Cyganowski et al. 2008](#)) and has associated H<sub>2</sub>O and CH<sub>3</sub>OH masers ([Beuther et al. 2002c](#); [Chen et al. 2011](#)). Sensitive VLA observations at 1.3 cm and 6 cm reveal seven cm sources in the region with spectral indices in the range from –0.2 to +1.1 ([Rosero et al. 2016](#)) at these wavelengths. [Issac et al. \(2020\)](#) find that IRAS 18264 is a protocluster with multiple radio as well as mm components detected. The C<sup>17</sup>O line has an inverse P-Cygni profile tracing infalling material and multiple bipolar outflows are traced by C<sup>18</sup>O ([Issac et al. 2020](#)).

### B.7. HMC G9.62+0.19 (Fig. B.7)

The G9.62+0.19 star-forming complex consists of protostars at different evolutionary stages, from an embedded HMC to evolved UCH<sub>II</sub> regions, revealed by multi-wavelength observa-

tions from NIR to radio wavelengths ([Cesaroni et al. 1994](#); [Testi et al. 1998](#); [Linz et al. 2005](#)). The NIR emission is not only dominated by the SED of the YSO, but there are also contributions of the circumstellar matter and outflows, and the non-detection of the UCH<sub>II</sub> regions is consistent with a high extinction ([Linz et al. 2005](#)).

High angular resolution observations at 1 mm carried out by [Liu et al. \(2017\)](#) reveal that the filament contains at least 12 dense cores at different evolutionary stages from starless cores to the known UCH<sub>II</sub> regions, with three cores harboring molecular outflows. The authors propose that the expanding UCH<sub>II</sub> regions compress the gas of the clump in a filament in which sequential star formation is then triggered. The feedback of the UCH<sub>II</sub> regions results in a lack of low-mass star formation ([Liu et al. 2017](#)).

[Liu et al. \(2020\)](#) studied the spatial correlation of the molecular emission using ALMA 3 mm observations using the histogram of oriented gradients (HOG) method ([Soler et al. 2019](#)) that was also applied to the molecular lines of the CORE-extension regions ([Gieser et al. 2022](#)). The authors find that the molecules can be grouped to species that either trace extended emission (CS, HCN, HCO<sup>+</sup>), shocks (SiO), or the dense cores (SO, H<sup>13</sup>CN, HC<sub>3</sub>N, CH<sub>3</sub>OH). Widespread SiO emission with narrow line widths seems to stem from either colliding flows or the H<sub>II</sub> regions ([Liu et al. 2020](#)). A sketch of the regions with the dense cores at evolutionary stages under the influence of the H<sub>II</sub>



Table A.2: Overview of the spectral windows observed with ALMA.

SPR	spw	Central frequency $\nu_0$ (GHz)	Bandwidth (GHz)	number of channels $n_{\text{channel}}$	channel spacing $\delta\nu$ (MHz)	Targeted species
SPR1	0	86.676	0.117	480	0.244	HCO
SPR1	1	86.759	0.117	480	0.244	H <sup>13</sup> CO <sup>+</sup>
SPR1	2	86.852	0.117	480	0.244	SiO, CH <sub>3</sub> CH <sub>2</sub> CN
SPR1	3	86.345	0.117	480	0.244	H <sup>13</sup> CN
SPR1	4	87.44	0.117	480	0.244	CCH
SPR1	5	88.637	0.117	480	0.244	HCN, CH <sub>3</sub> OH
SPR1	6	87.93	0.117	480	0.244	HNCO
SPR1	7	87.322	0.117	480	0.244	CCH
SPR1	8	97.721	0.117	480	0.244	<sup>34</sup> SO
SPR1	9	97.987	0.117	480	0.244	CS
SPR1	10	96.926	0.117	480	0.244	CH <sub>3</sub> CH <sub>2</sub> CN
SPR1	11	96.994	0.117	480	0.244	O <sup>13</sup> CS, H <sup>13</sup> CCCN
SPR1	12	99.331	0.117	480	0.244	CH <sub>3</sub> OCH <sub>3</sub>
SPR1	13	100.736	0.117	480	0.244	HC <sub>3</sub> N, CH <sub>3</sub> OCHO
SPR1	14	99.305	0.117	480	0.244	SO
SPR1	15	99.872	0.117	480	0.244	CCS
SPR2	0	108.786	0.117	480	0.244	<sup>13</sup> CN
SPR2	1	110.207	0.117	480	0.244	<sup>13</sup> CO
SPR2	2	109.469	0.117	480	0.244	OCS, HNCO, HC <sub>3</sub> N
SPR2	3	109.788	0.117	480	0.244	C <sup>18</sup> O, NH <sub>2</sub> CHO
SPR2	4	109.506	1.875	1920	0.977	C <sup>15</sup> N, SiS, HC <sub>3</sub> N, HC <sub>5</sub> N, CH <sub>3</sub> OCH <sub>3</sub>
SPR2	5	97.006	1.875	1920	0.977	C <sup>33</sup> S, H <sup>13</sup> CS, C <sub>2</sub> H <sub>5</sub> OH, CH <sub>3</sub> NCO
SPR2	6	98.806	1.875	1920	0.977	H $\alpha$ , CH <sub>3</sub> CHO, CH <sub>3</sub> OCHO, CH <sub>3</sub> COCH <sub>3</sub>
SPR3	0	104.035	0.117	480	0.244	CH <sub>3</sub> CH <sub>2</sub> CN, SO <sub>2</sub> , CH <sub>3</sub> OH
SPR3	1	102.224	0.117	480	0.244	HSCN, CH <sub>3</sub> SH
SPR3	2	103.047	0.117	480	0.244	H <sub>2</sub> CS
SPR3	3	103.223	0.117	480	0.244	NH <sub>2</sub> CHO
SPR3	4	104.207	0.117	480	0.244	CH <sub>2</sub> CHCN, SO <sub>2</sub> , CH <sub>3</sub> OCH <sub>3</sub>
SPR3	5	104.88	0.117	480	0.244	HOCN
SPR3	6	104.717	0.117	480	0.244	<sup>13</sup> C <sup>18</sup> O, CH <sub>3</sub> OCH <sub>3</sub>
SPR3	7	105.564	0.117	480	0.244	CH <sub>3</sub> OH, CH <sub>3</sub> OCH <sub>3</sub>
SPR3	8	90.269	0.117	480	0.244	<sup>15</sup> NNH <sup>+</sup> , CH <sub>3</sub> OCHO
SPR3	9	90.669	0.117	480	0.244	HNC, CCS
SPR3	10	90.985	0.117	480	0.244	<sup>13</sup> C <sup>34</sup> S, HC <sub>3</sub> N, CH <sub>3</sub> OCH <sub>3</sub>
SPR3	11	91.945	0.117	480	0.244	CH <sub>3</sub> <sup>13</sup> CN
SPR3	12	91.64	0.117	480	0.244	CH <sub>3</sub> COCH <sub>3</sub>
SPR3	13	91.985	0.117	480	0.244	CH <sub>3</sub> CN
SPR3	14	93.179	0.117	480	0.244	N <sub>2</sub> H <sup>+</sup>
SPR3	15	92.415	0.117	480	0.244	CH <sub>2</sub> CHCN, CH <sub>3</sub> OH

regions is given in Fig. 10 in Liu et al. (2017) and Fig. 20 in Liu et al. (2020).

### B.8. HMC G10.47+0.03 (Fig. B.8)

The G10.47+0.03 region contains several MIR sources including a HMC, as well as multiple UCH<sub>II</sub> regions and strong maser activity (Pascucci et al. 2004, and references within). Cesaroni et al. (2010) found that three UCH<sub>II</sub> regions are located within the HMC itself. Based on CH<sub>3</sub>CN line emission the temperature in the innermost 1.''5 is estimated to be 160 K (Olmli et al. 1996). Molecular emission lines reveals that there is outflowing gas as well as infalling material (Rolffs et al. 2011). The authors find that the density toward the central 10 000 au flattens due to pressure (e.g., thermal, turbulent, wind-driven) driving expan-

sion. Gorai et al. (2020) detect precursors of prebiotic molecules toward the HMC, including HNCO, NH<sub>2</sub>CHO, and CH<sub>3</sub>NCO.

### B.9. HMC G34.26+0.15 (Fig. B.9)

G34.26+0.15 contains a cometary UCH<sub>II</sub> region and two unresolved UCH<sub>II</sub> regions (Reid & Ho 1985). The cometary UCH<sub>II</sub> region harbors a line-rich HMC (MacDonald et al. 1996). Mookerjea et al. (2007) find that the HMC is externally heated by the UCH<sub>II</sub> region with no internal heating. Toward the region, many COMs such as CH<sub>3</sub>OCHO, CH<sub>3</sub>OCH<sub>3</sub>, and NH<sub>2</sub>CHO are detected (Mookerjea et al. 2007). Ammonia (NH<sub>3</sub>) lines have inverse P-Cygni profiles indicating infalling material (Hajigholi et al. 2016).

**B.10. UCH<sub>II</sub> G10.30–0.15 (Fig. B.10)**

The UCH<sub>II</sub> region G10.30–0.15 is part of the W31 star-forming complex containing a cluster of stars and YSOs at different evolutionary stages (Beuther et al. 2011) and a large scale bipolar H<sub>II</sub> region launched by a massive O8–O9 star (Deharveng et al. 2015). The UCH<sub>II</sub> region G10.30–0.15 is associated with CH<sub>3</sub>OH maser emission and the central object is a B0 star (Deharveng et al. 2015). The authors studied the clustered nature of the W31 region and find that five clumps, including the clump containing G10.30–0.15 at the waist of the bipolar H<sub>II</sub> region, are a result of triggered star formation.

**B.11. UCH<sub>II</sub> G13.87+0.28 (Fig. B.11)**

G13.87+0.28 is a cometary UCH<sub>II</sub> region, with a bright head and an extended low brightness tail. The morphology and kinematics of the ionized and molecular gas are consistent with a bow shock launched by a stellar wind of a massive O6.5 ZAMS star (Garay et al. 1994). High velocity components of 22 GHz water masers are likely associated with an outflow (Xi et al. 2015).

**Appendix C: Source properties**

The fragmentation properties of the regions based on the 3 mm continuum emission are analyzed in Sect. 4.1. Table C.1 summarizes the properties derived with `clumpfind`, such as position and peak intensity of all fragments. We classify the fragments into protostellar sources (including dust cores, dust+ff cores and cometary UCH<sub>II</sub> regions), while cores with  $S/N < 15$  are not further analyzed in this study due to insufficient sensitivity and angular resolution. The dust cores have compact mm emission, while dust+ff cores have in addition H(40) $\alpha$  recombination line (Fig. D.1) and CORNISH 6 cm emission (Figs. B.1 - B.11). Our sample also covers three cometary UCH<sub>II</sub> regions with extended, cometary-shaped, mm emission as well as H(40) $\alpha$  recombination line and 6 cm emission.

Table C.2 summarizes the radial temperature fit results derived in Sect. 5.3 for all protostellar sources. Fig. 6 shows the radial temperature profile and fit for dust core 1 in HMPO IRAS 18089 and for the remaining sources the profiles are shown in Fig. C.1. The beam-averaged temperature (Sect. 5), and H<sub>2</sub> column density and mass (Sect. 7) are listed in Table C.3 for all protostellar sources.

Table C.4 summarizes the fit results of the visibility profiles and corresponding density profiles for all protostellar sources (Sect. 6.2). Fig. 7 shows the visibility profile and fit for HMC G9.62+0.192 and for the remaining sources the profiles are shown in Fig. C.2.

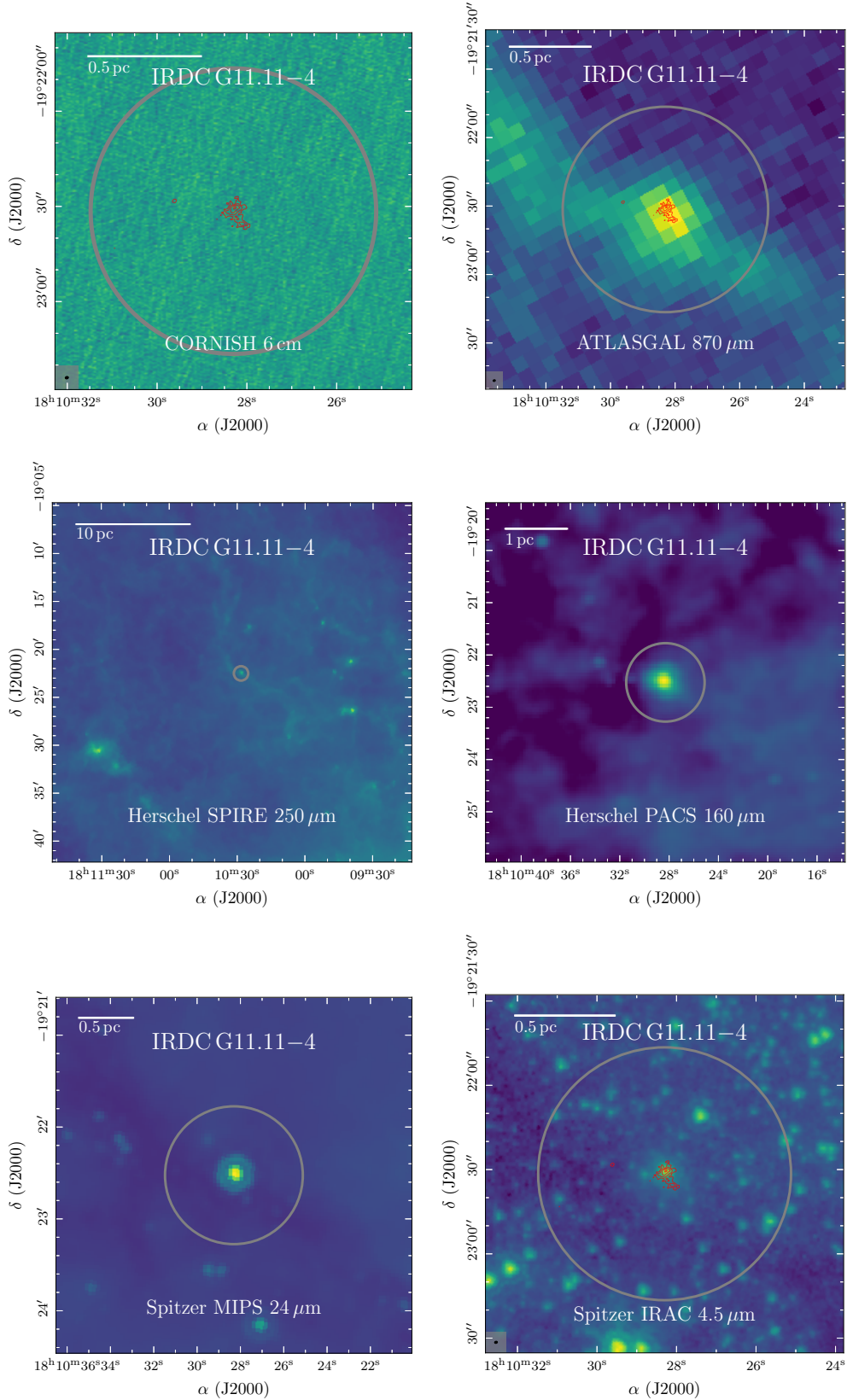


Fig. B.1: Multi wavelength overview of IRDC G11.11-4. In color, CORNISH 6 cm, ATLASGAL 870 $\mu$ m, *Herschel* SPIRE 250  $\mu$ m, *Herschel* PACS 70  $\mu$ m, *Spitzer* MIPS 24  $\mu$ m, and *Spitzer* IRAC 4.5  $\mu$ m data are presented as labeled. In all panels, the ALMA primary beam size is indicated by a grey circle. In the top right and left and bottom right panel, the ALMA 3 mm continuum data are shown by red contours. The dotted red contour marks the  $-5\sigma_{\text{cont}}$  level. The solid red contours start at  $5\sigma_{\text{cont}}$  and contour steps increase by a factor of 2 (e.g., 5, 10, 20, 40 $\sigma_{\text{cont}}$ ). The ALMA synthesized beam size is shown in the bottom left corner.



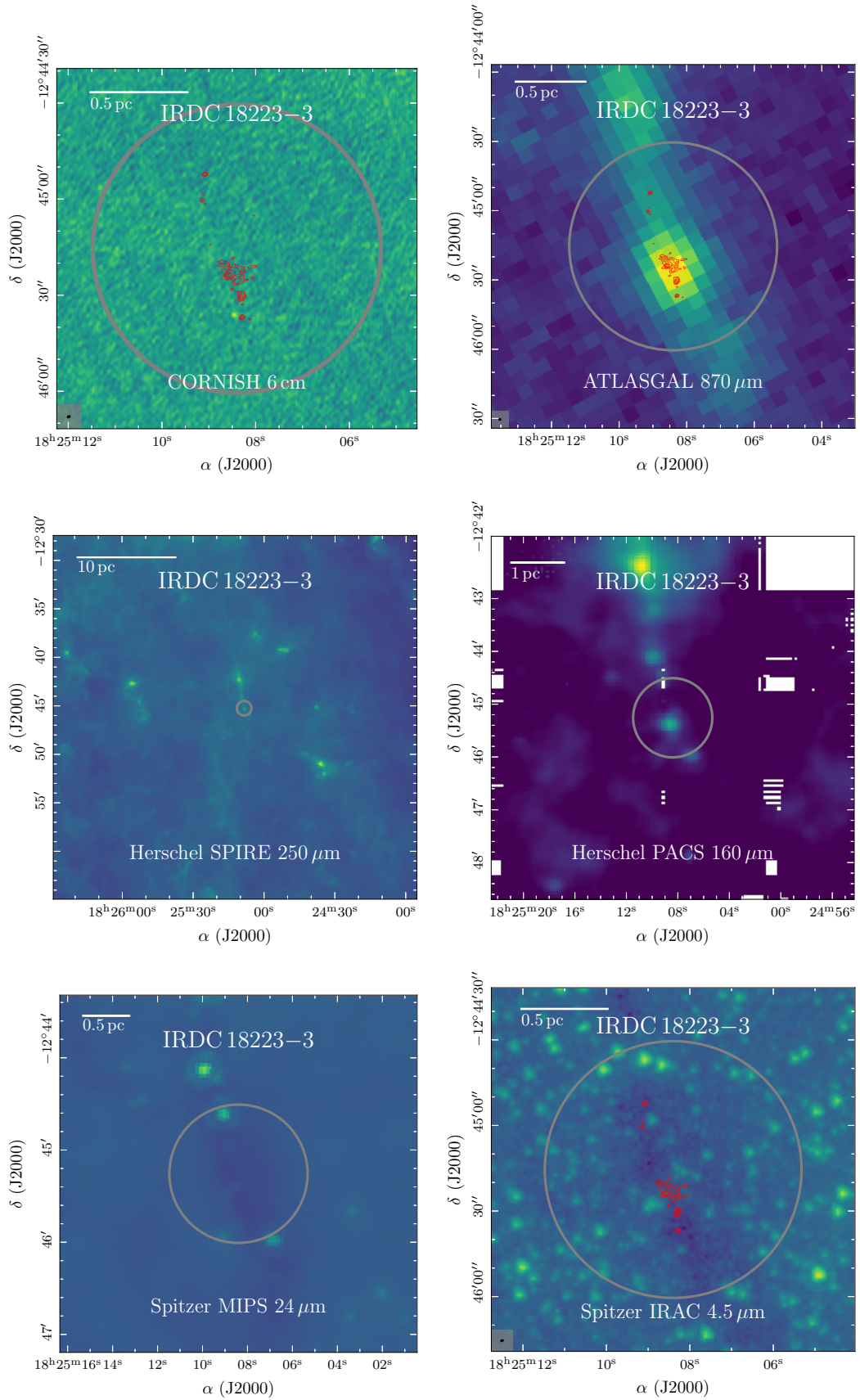


Fig. B.2: The same as Fig. B.1, but for IRDC 18223-3.

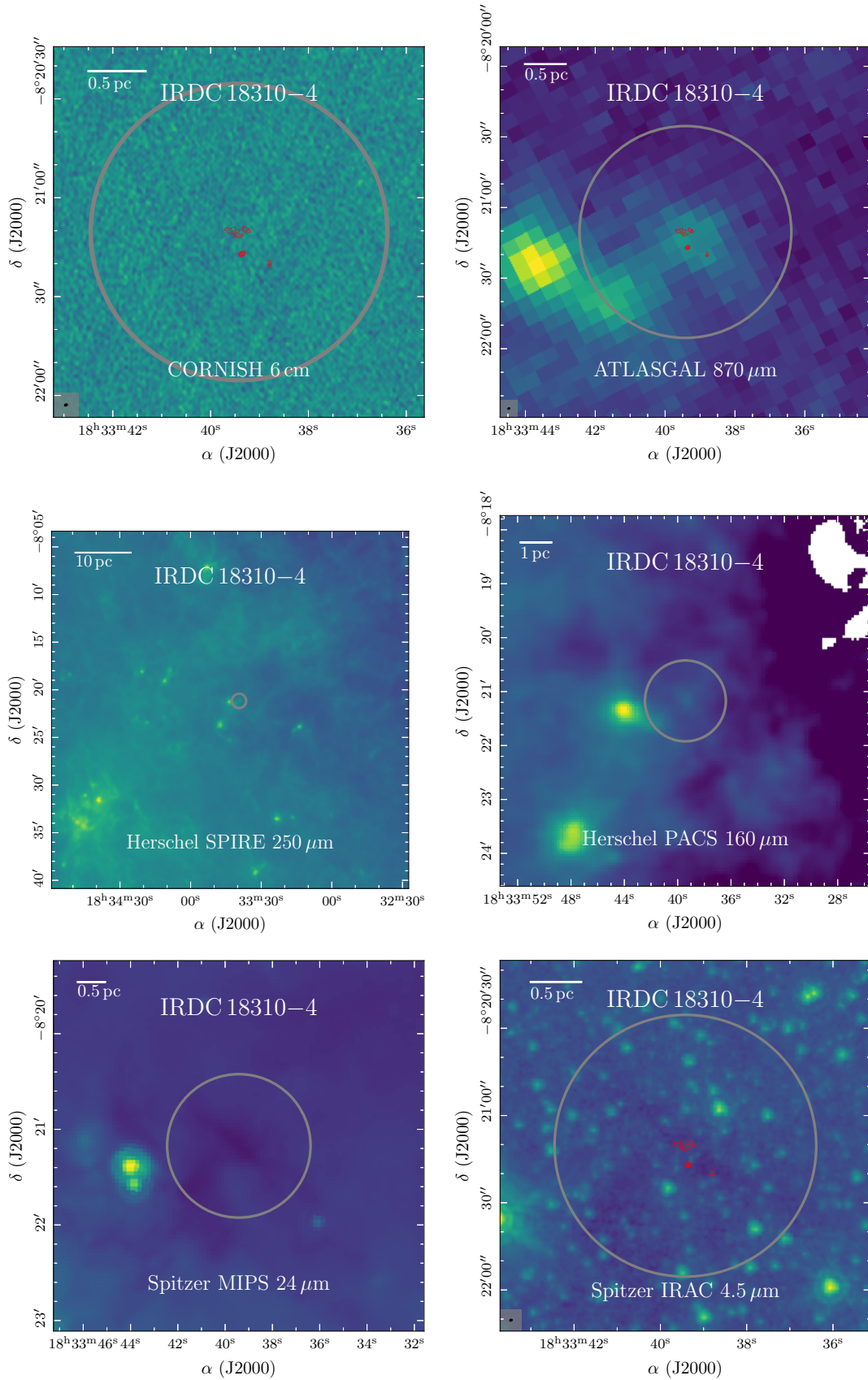


Fig. B.3: The same as Fig. B.1, but for IRDC 18310-4.

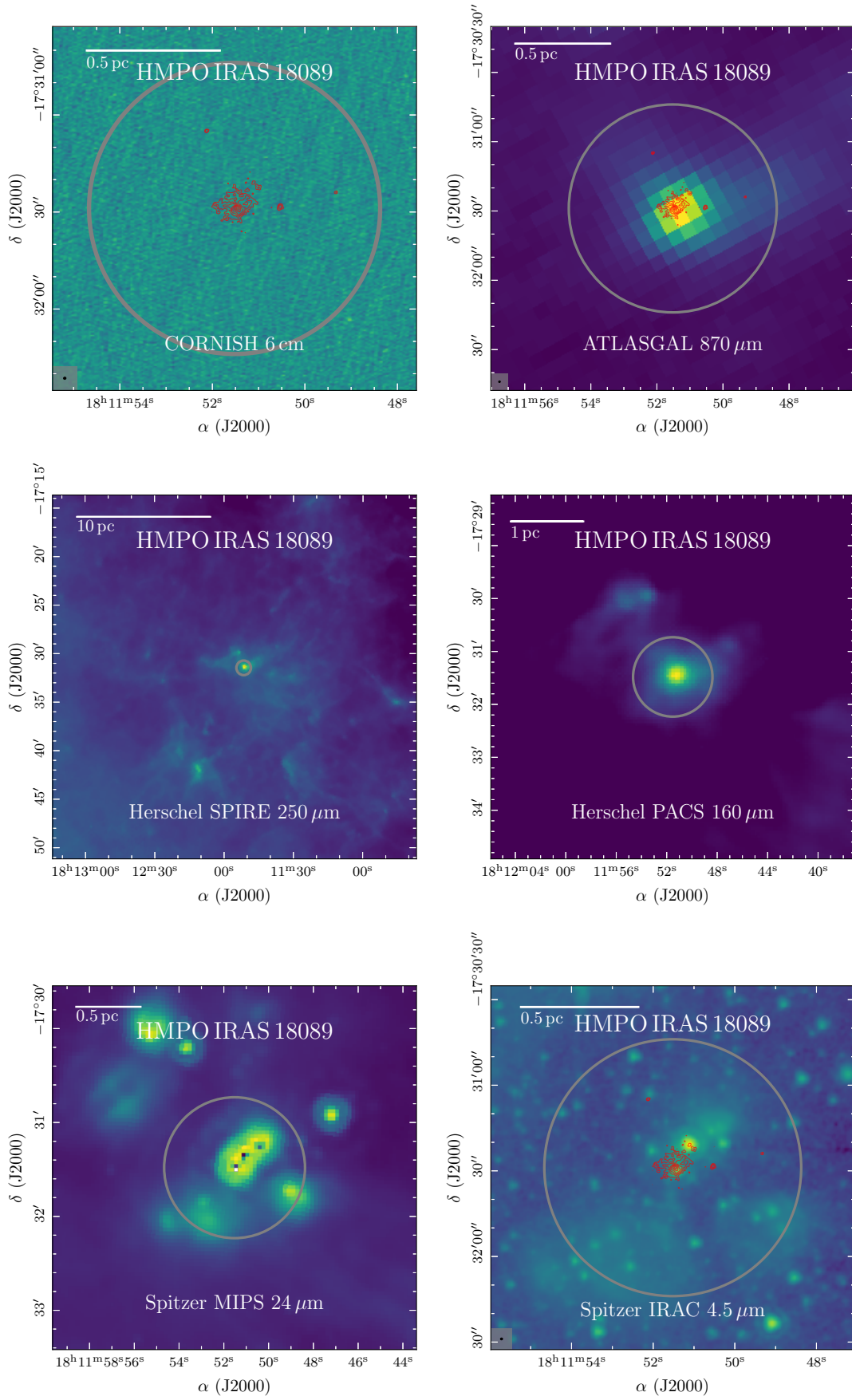


Fig. B.4: The same as Fig. B.1, but for HMPO IRAS 18089.



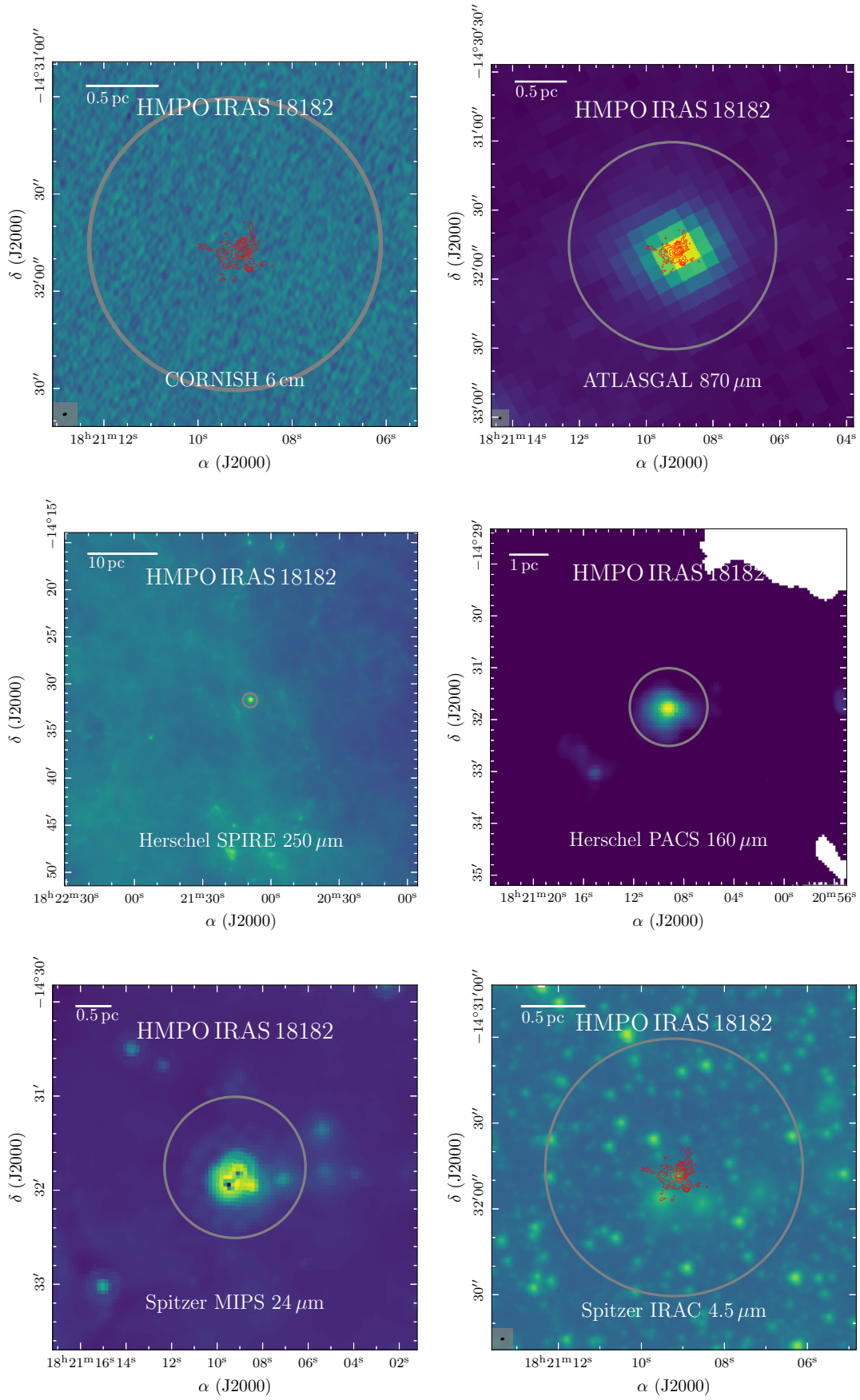


Fig. B.5: The same as Fig. B.1, but for HMPO IRAS 18182.

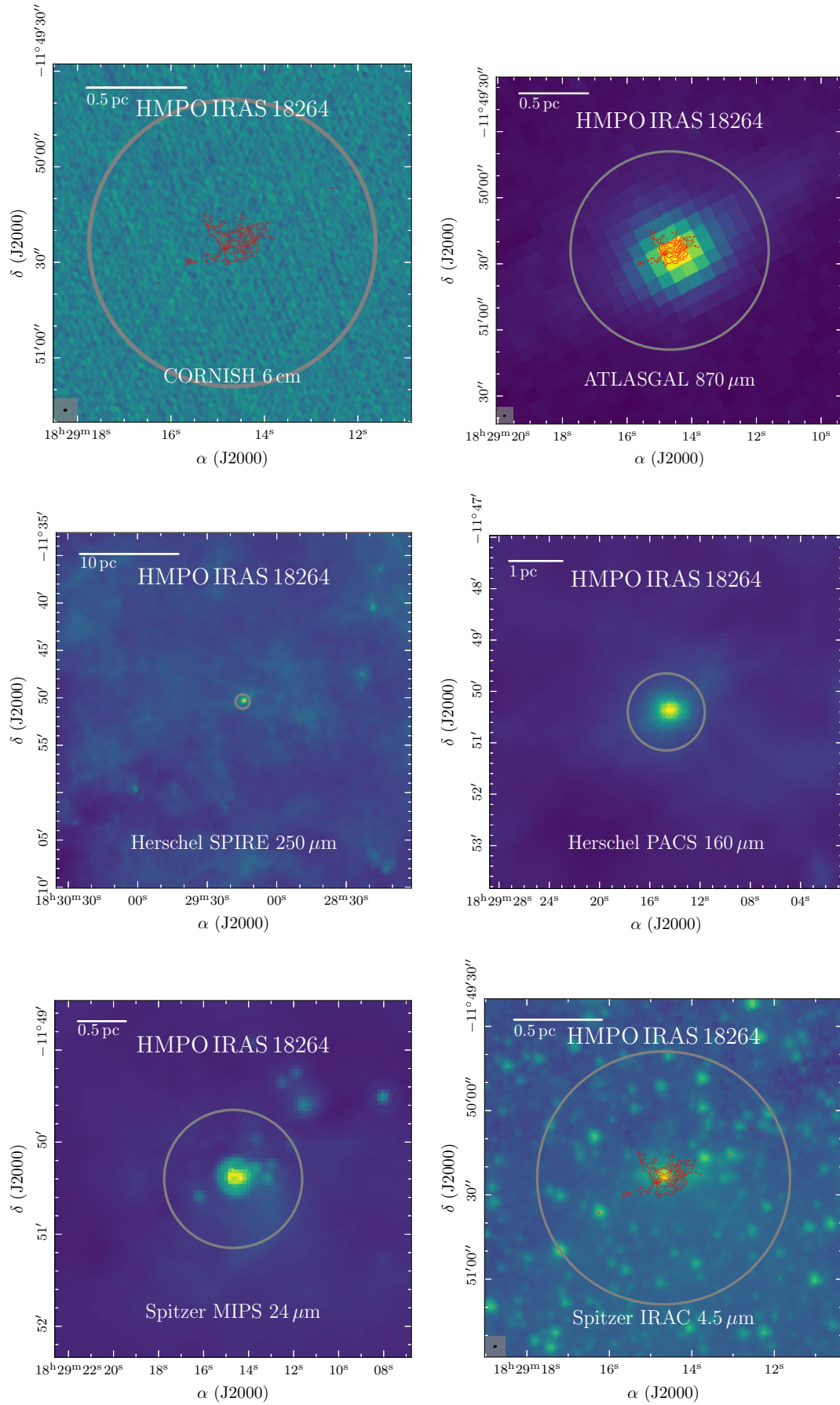


Fig. B.6: The same as Fig. B.1, but for HMPO IRAS 18264.

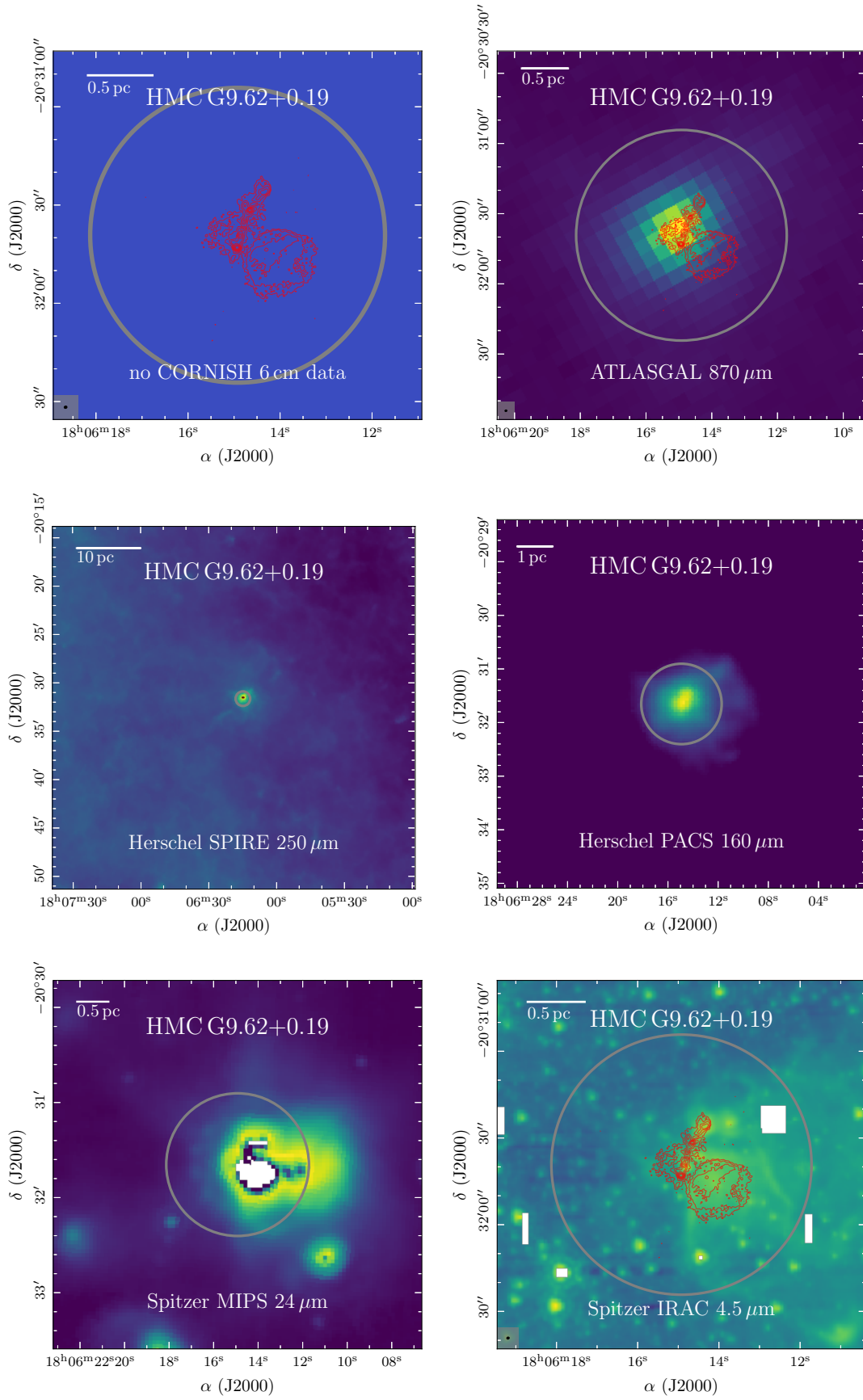


Fig. B.7: The same as Fig. B.1, but for HMC G9.62+0.19. The region was not covered by the CORNISH survey.



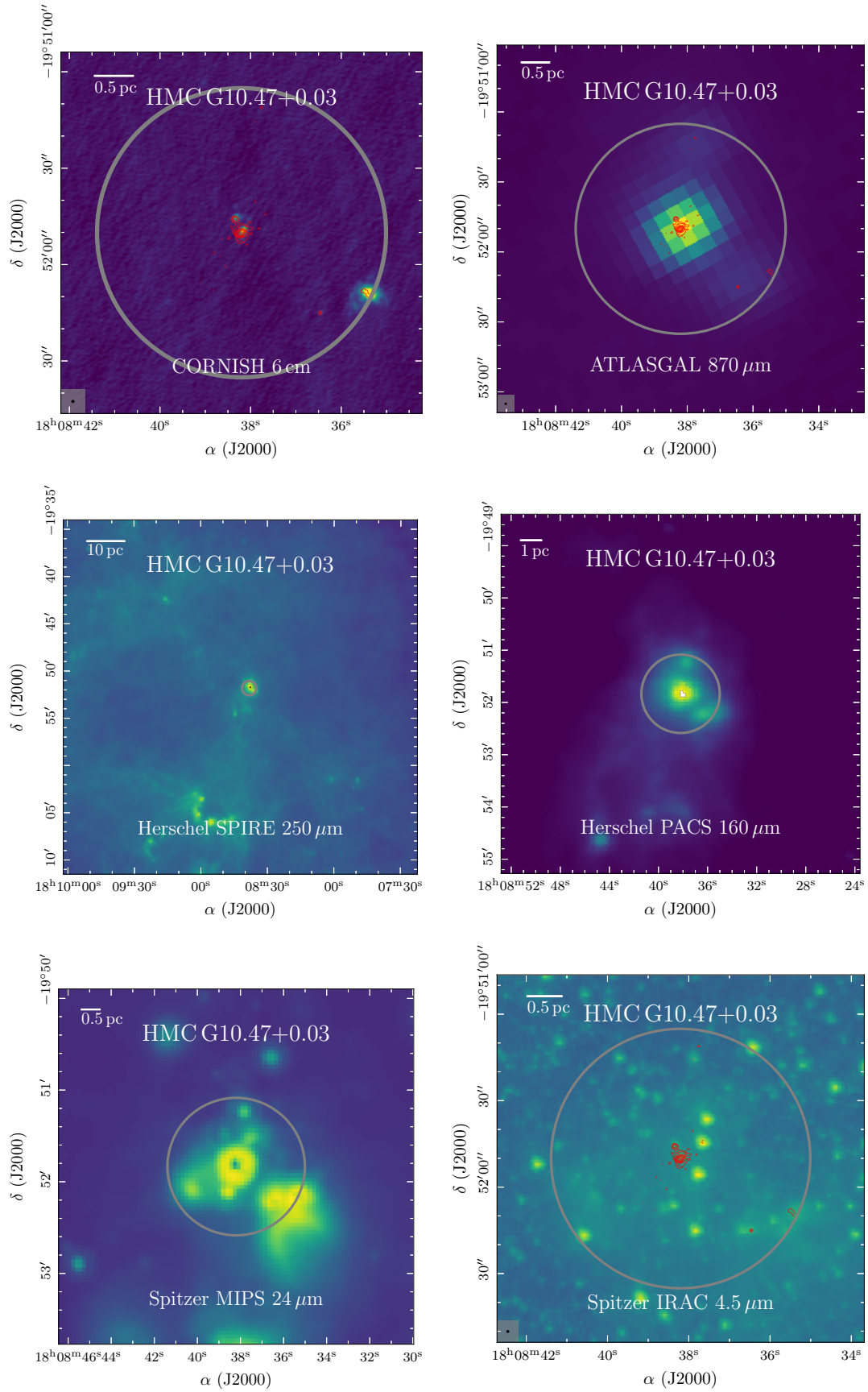


Fig. B.8: The same as Fig. B.1, but for HMC G10.47+0.03.

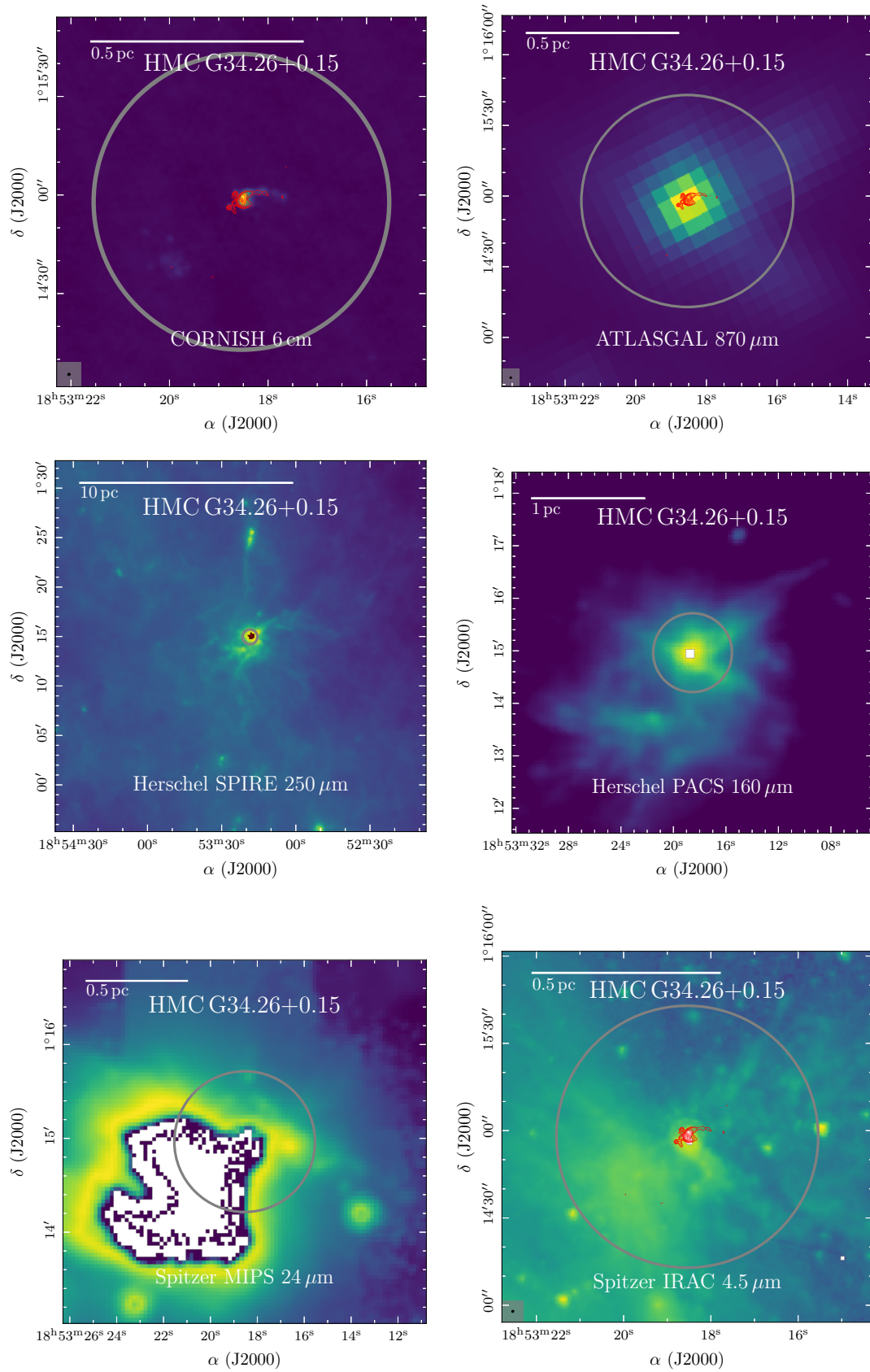


Fig. B.9: The same as Fig. B.1, but for HMC G34.26+0.15.

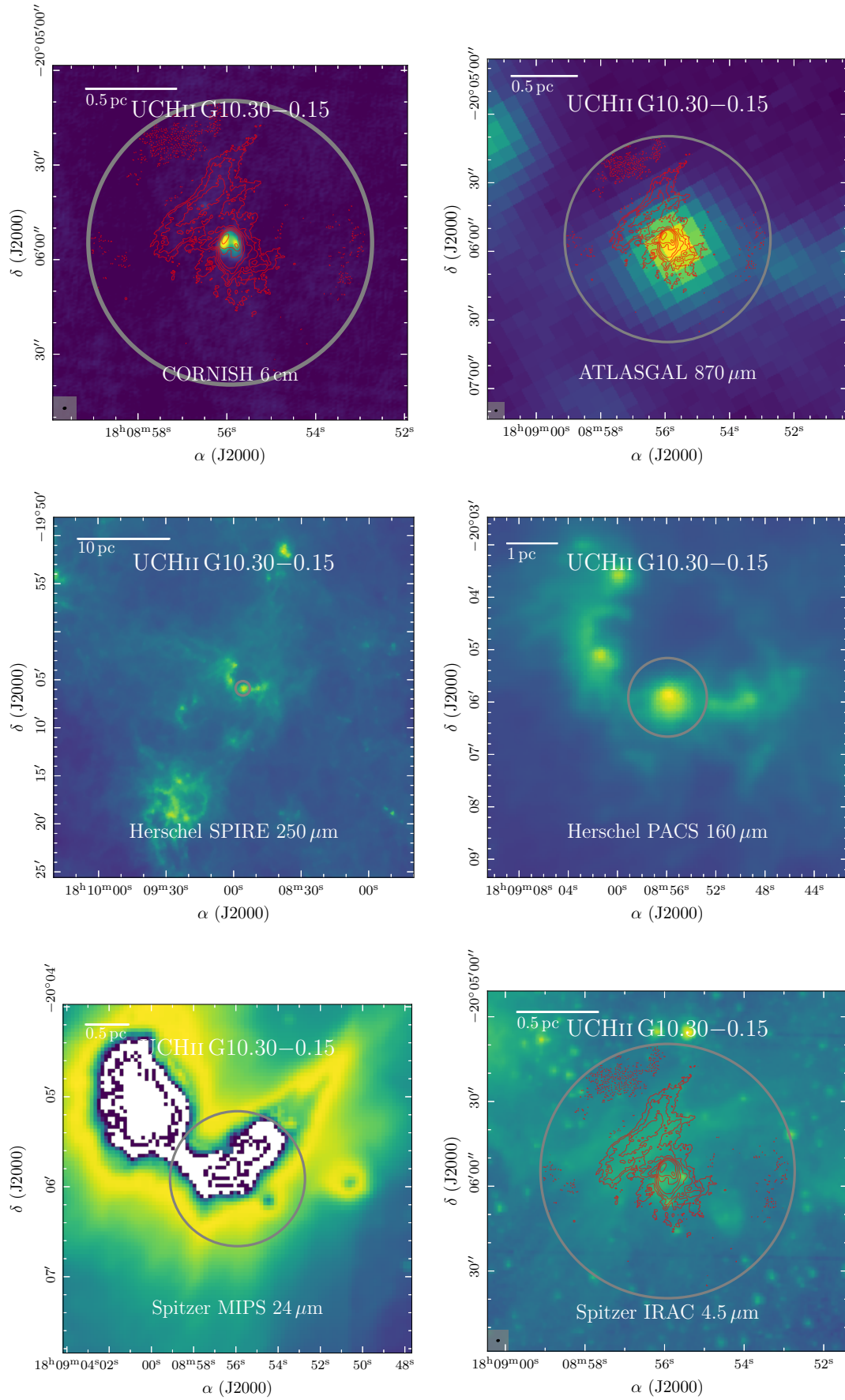


Fig. B.10: The same as Fig. B.1, but for UCH II G10.30-0.15.

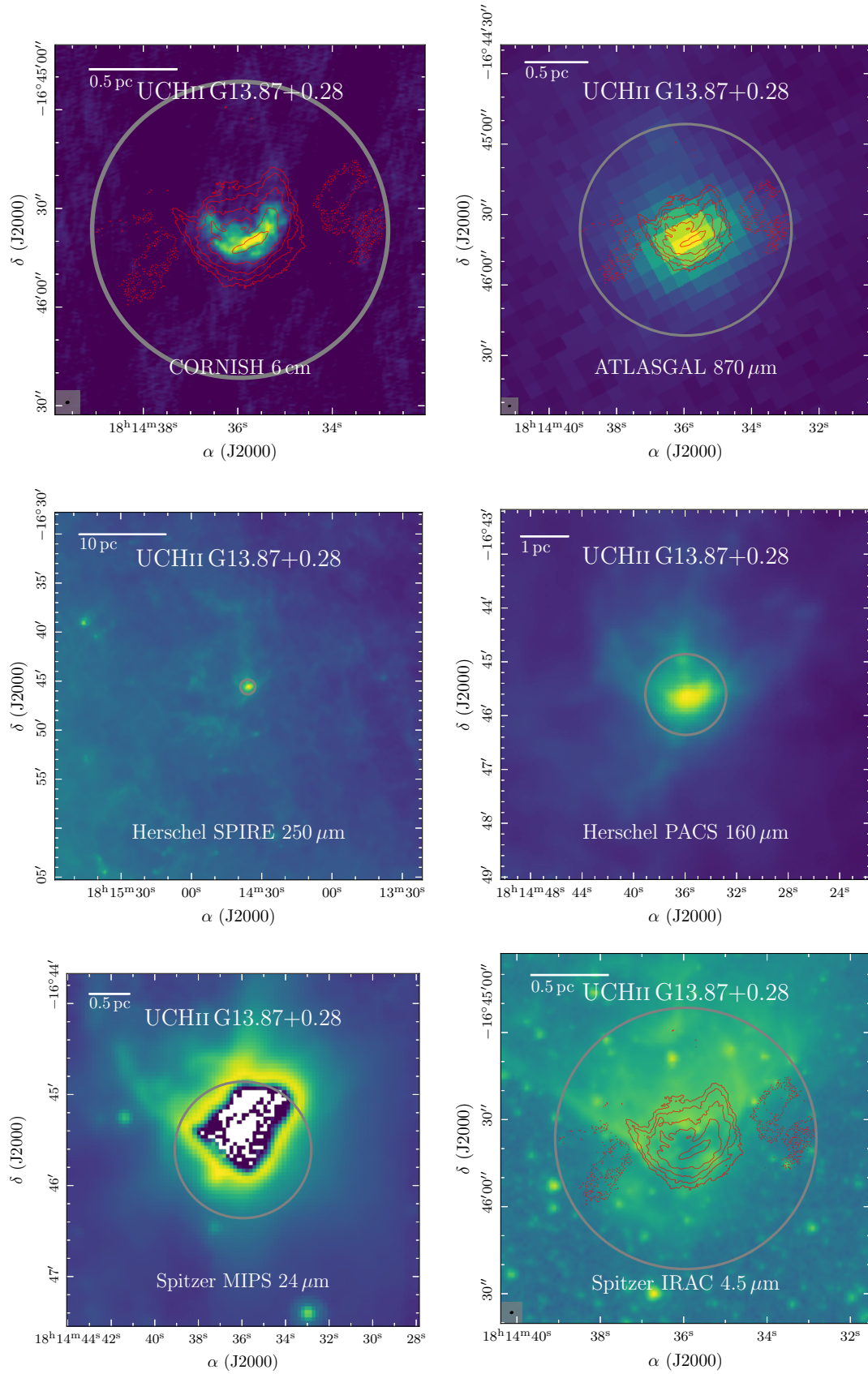


Fig. B.11: The same as Fig. B.1, but for UCH II G13.87+0.28.



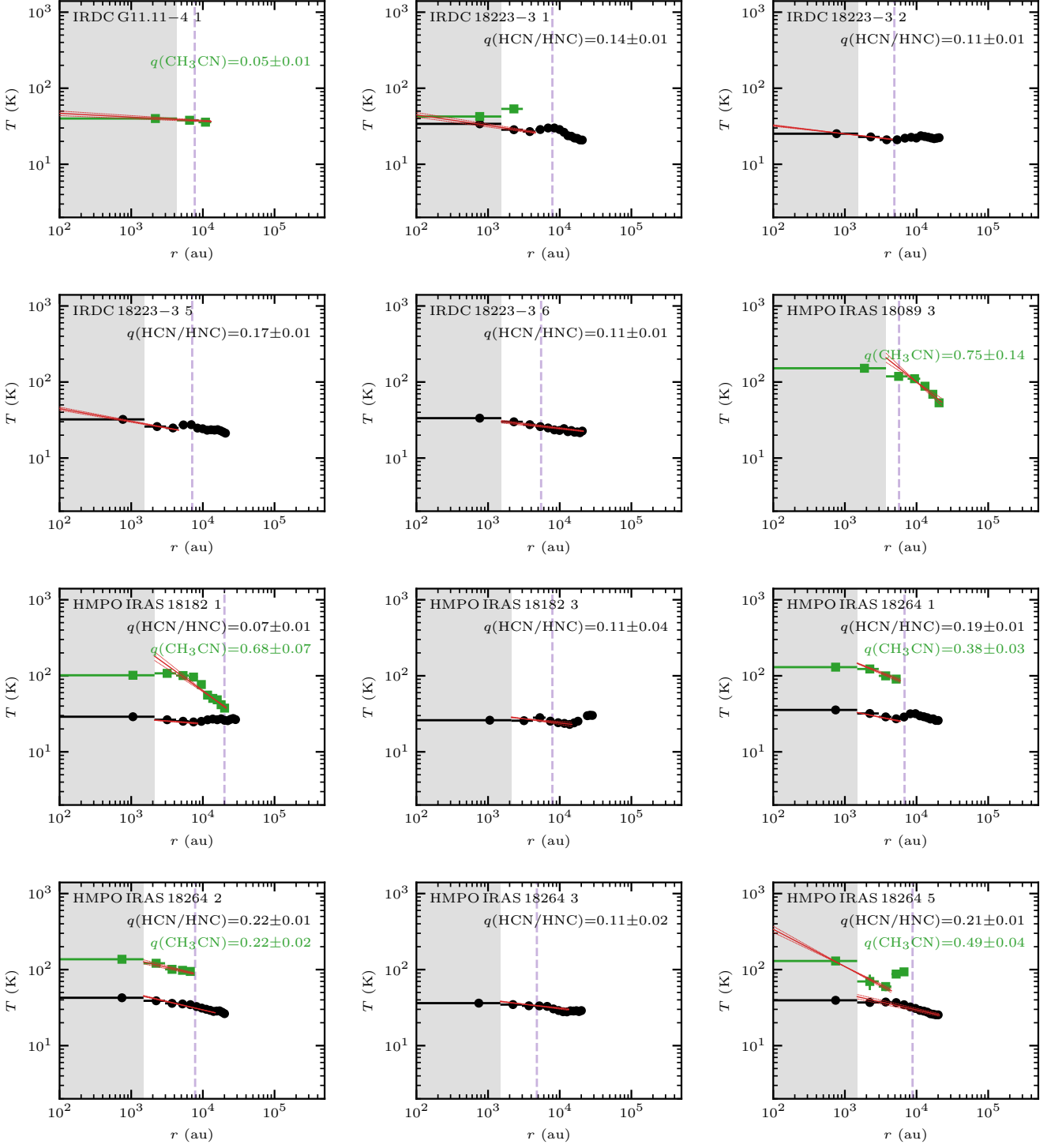


Fig. C.1: Radial temperature profiles. The profiles extracted from the HCN-to-HNC intensity ratio (Fig. 3),  $\text{CH}_3\text{CN}$  (Fig. 4), and  $\text{CH}_3^{13}\text{CN}$  (Fig. 5) temperature maps are shown by black circles, green squares, and blue diamonds, respectively. The inner unresolved region (one beam radius) is shown as a grey-shaded area. The dashed purple vertical line indicates the outer radius  $r_{\text{out}}$  of the continuum (Table C.1). A power-law fit and its  $1\sigma$  uncertainty to resolved and radially decreasing profiles is shown by the red solid and dashed lines, respectively (Sect. 5.3). The radial temperature profile of dust core 1 in HMPO IRAS 18089 is shown in Fig. 6.

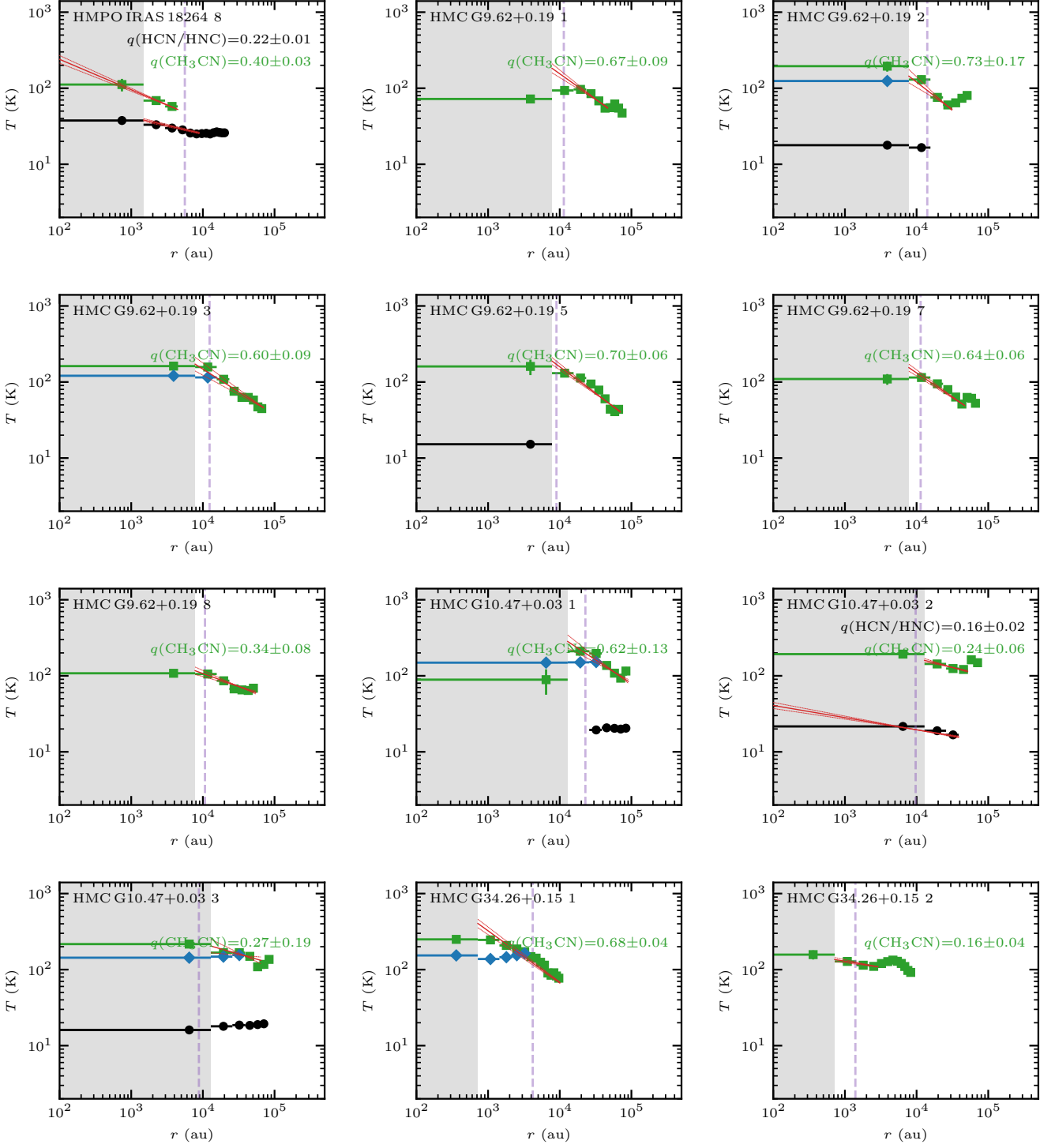


Fig. C.1 (cont.): Radial temperature profiles. The profiles extracted from the HCN-to-HNC intensity ratio (Fig. 3),  $\text{CH}_3\text{CN}$  (Fig. 4), and  $\text{CH}_3^{13}\text{CN}$  (Fig. 5) temperature maps are shown by black circles, green squares, and blue diamonds, respectively. The inner unresolved region (one beam radius) is shown as a grey-shaded area. The dashed purple vertical line indicates the outer radius  $r_{\text{out}}$  of the continuum (Table C.1). A power-law fit and its  $1\sigma$  uncertainty to resolved and radially decreasing profiles is shown by the red solid and dashed lines, respectively (Sect. 5.3). The radial temperature profile of dust core 1 in HMPO IRAS 18089 is shown in Fig. 6.

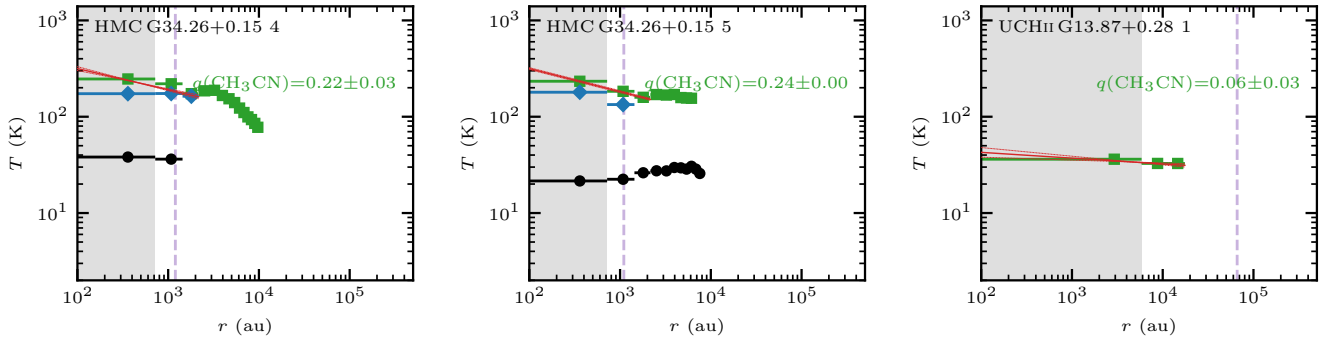


Fig. C.1 (cont.): Radial temperature profiles. The profiles extracted from the HCN-to-HNC intensity ratio (Fig. 3),  $\text{CH}_3\text{CN}$  (Fig. 4), and  $\text{CH}_3^{13}\text{CN}$  (Fig. 5) temperature maps are shown by black circles, green squares, and blue diamonds, respectively. The inner unresolved region (one beam radius) is shown as a grey-shaded area. The dashed purple vertical line indicates the outer radius  $r_{\text{out}}$  of the continuum (Table C.1). A power-law fit and its  $1\sigma$  uncertainty to resolved and radially decreasing profiles is shown by the red solid and dashed lines, respectively (Sect. 5.3). The radial temperature profile of dust core 1 in HMPO IRAS 18089 is shown in Fig. 6.

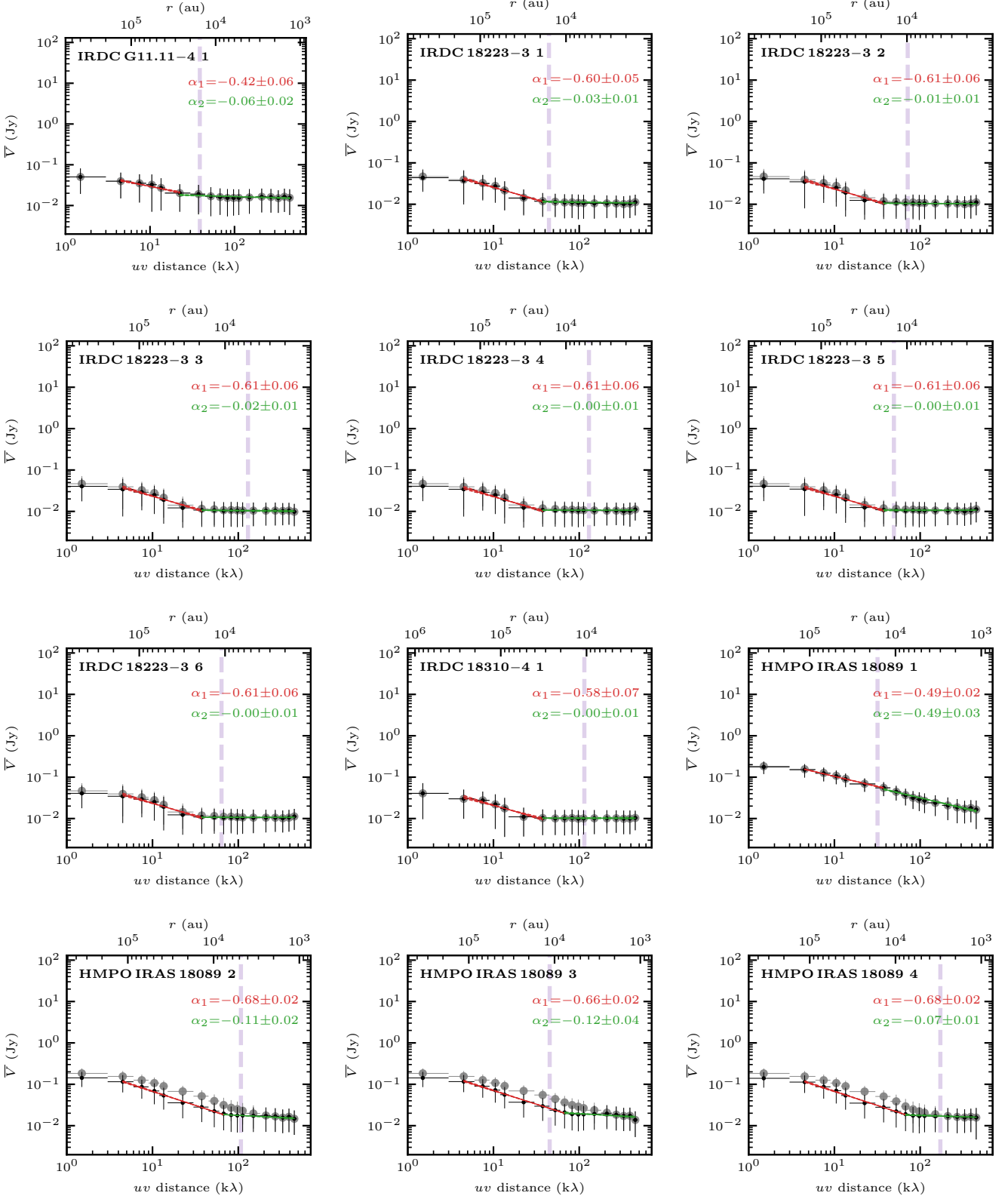


Fig. C.2: Visibility profiles. The profile of the non-core-subtracted and core-subtracted data is shown in grey and black, respectively (further explained in Sect. 6.1). Two power-law profiles, tracing the clump and core scales, are fitted to the core-subtracted data shown in red and green, respectively. The bottom axis shows the  $uv$  distance in k $\lambda$  and the top axis is the corresponding spatial scale. The purple dashed line indicates the diameter of the sources (Table C.1). The visibility profile of dust+ff core 2 in HMC G9.62+19 is shown in Fig. 7.



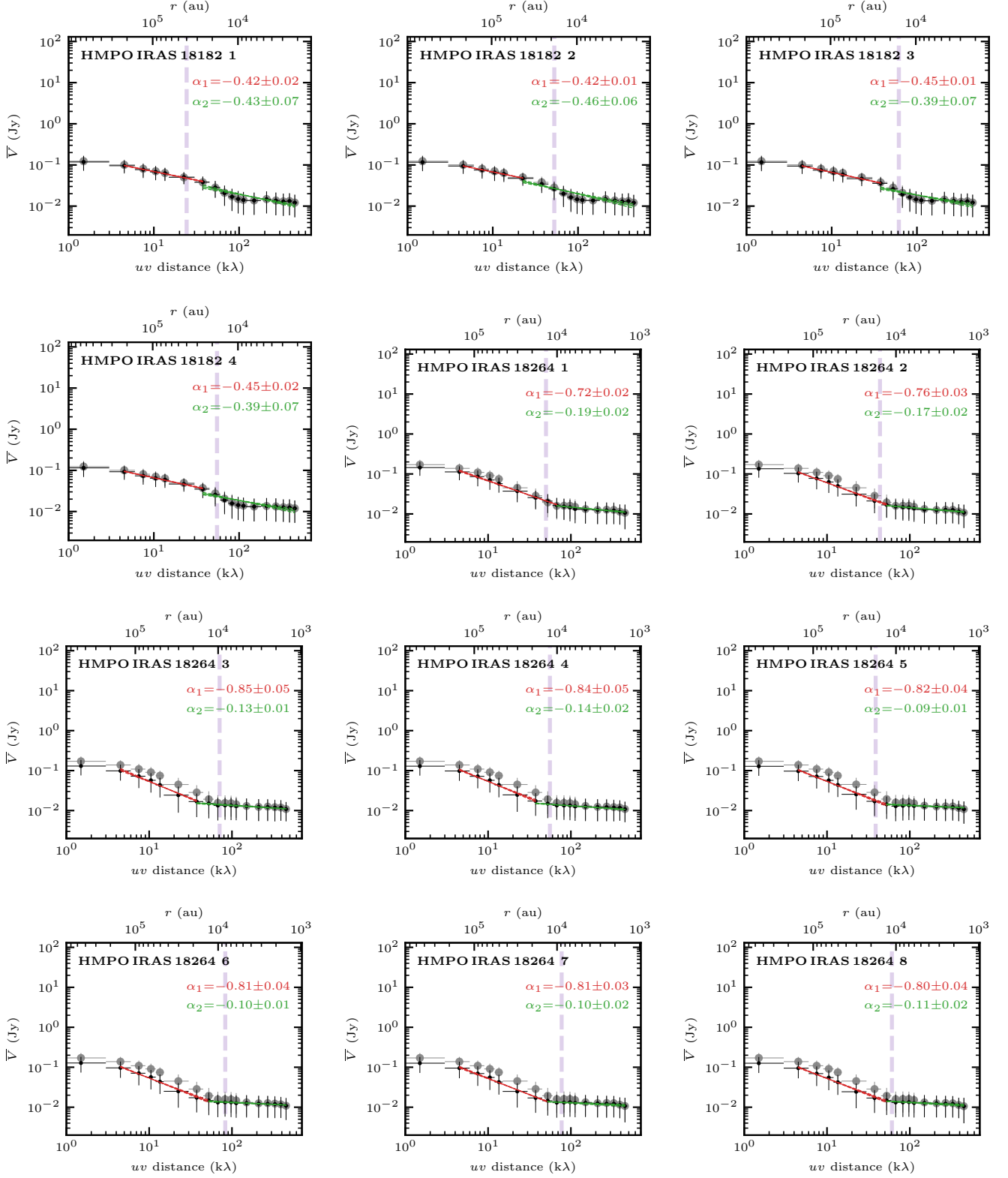


Fig. C.2 (cont.): Visibility profiles. The profile of the non-core-subtracted and core-subtracted data is shown in grey and black, respectively (further explained in Sect. 6.1). Two power-law profiles, tracing the clump and core scales, are fitted to the core-subtracted data shown in red and green, respectively. The bottom axis shows the  $uv$  distance in k $\lambda$  and the top axis is the corresponding spatial scale. The purple dashed line indicates the diameter of the sources (Table C.1). The visibility profile of dust+ff core 2 in HMC G9.62+.19 is shown in Fig. 7.

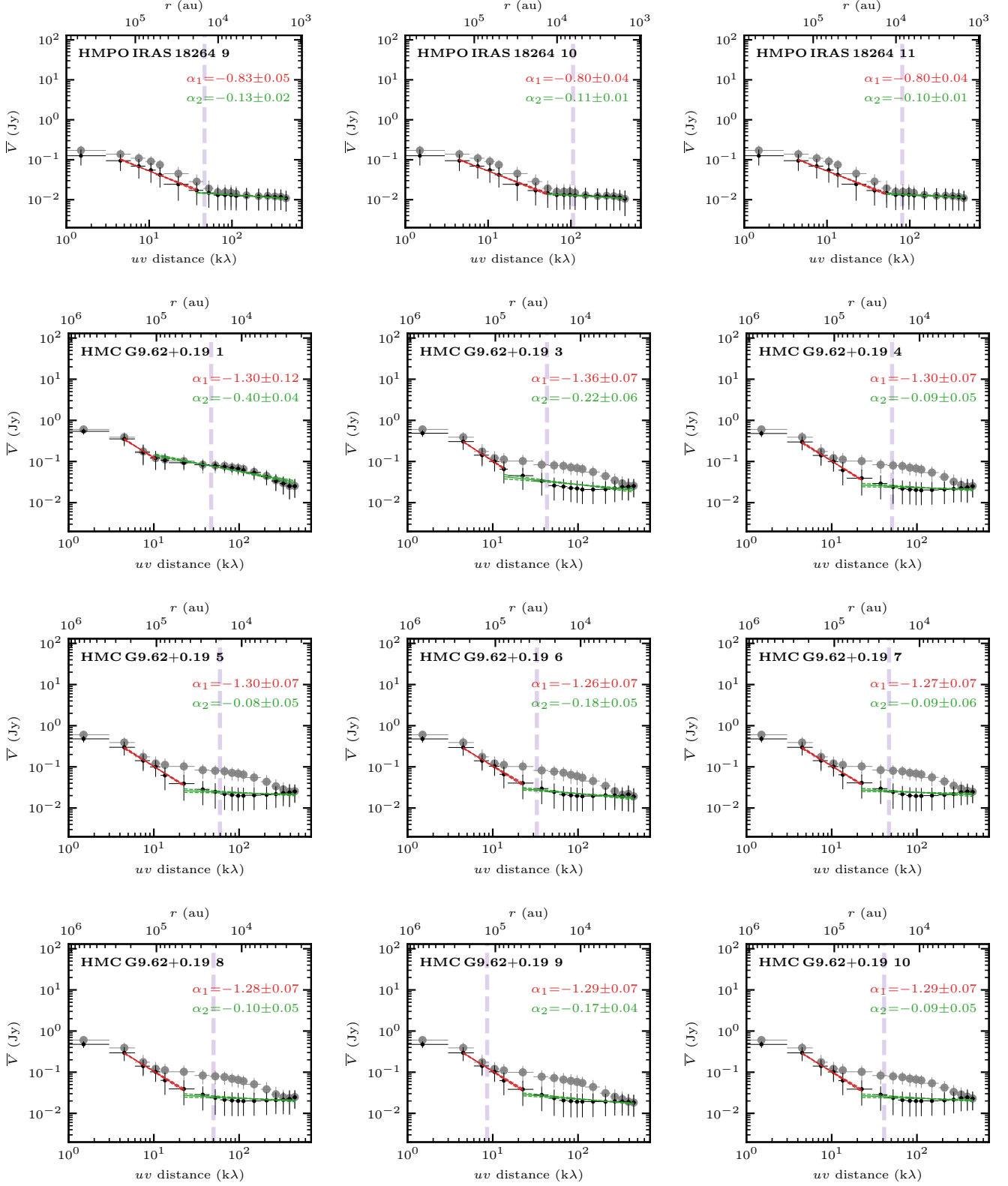


Fig. C.2 (cont.): Visibility profiles. The profile of the non-core-subtracted and core-subtracted data is shown in grey and black, respectively (further explained in Sect. 6.1). Two power-law profiles, tracing the clump and core scales, are fitted to the core-subtracted data shown in red and green, respectively. The bottom axis shows the  $uv$  distance in  $k\lambda$  and the top axis is the corresponding spatial scale. The purple dashed line indicates the diameter of the sources (Table C.1). The visibility profile of dust+ff core 2 in HMC G9.62+.19 is shown in Fig. 7.

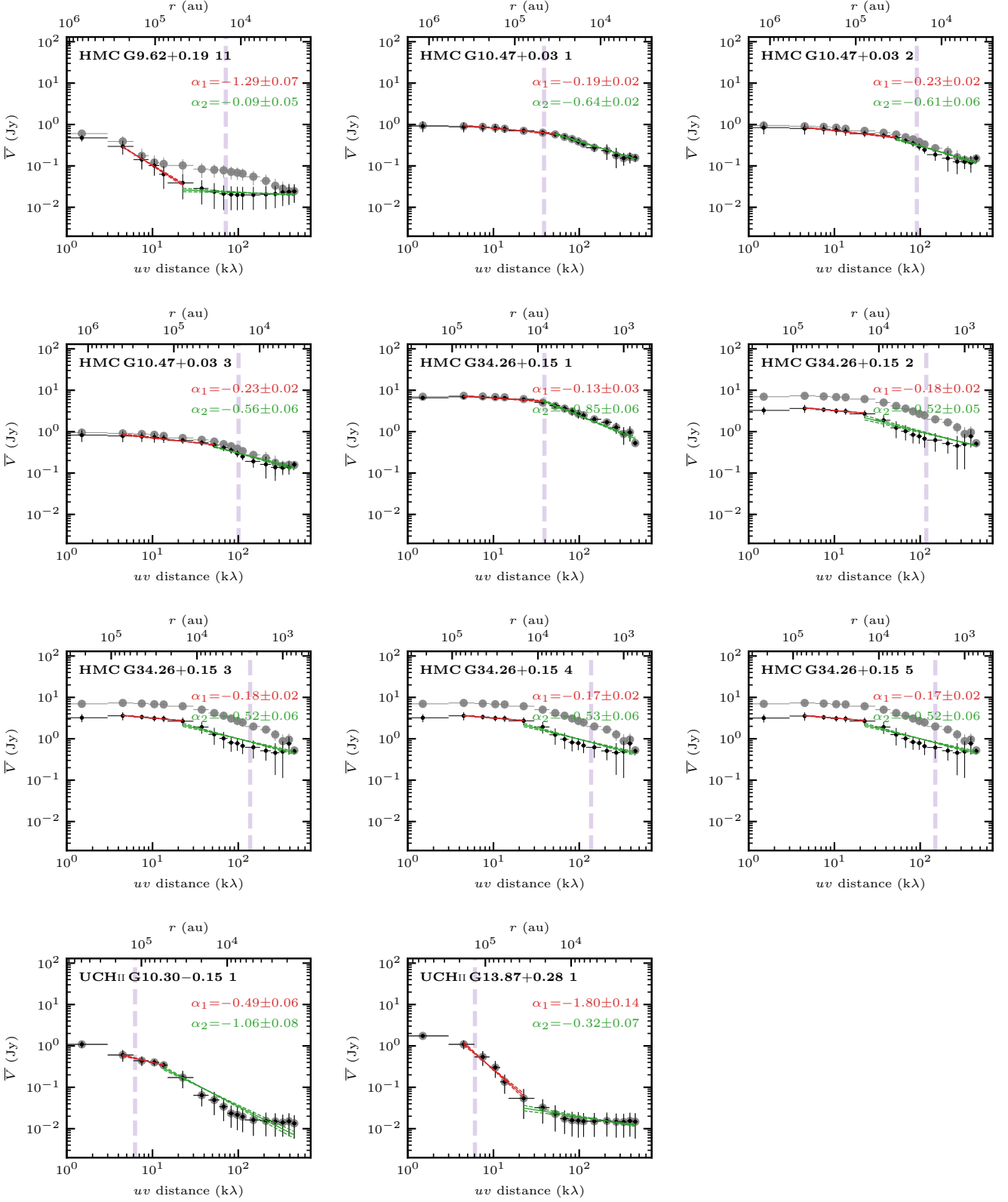


Fig. C.2 (cont.): Visibility profiles. The profile of the non-core-subtracted and core-subtracted data is shown in grey and black, respectively (further explained in Sect. 6.1). Two power-law profiles, tracing the clump and core scales, are fitted to the core-subtracted data shown in red and green, respectively. The bottom axis shows the  $uv$  distance in  $k\lambda$  and the top axis is the corresponding spatial scale. The purple dashed line indicates the diameter of the sources (Table C.1). The visibility profile of dust+ff core 2 in HMC G9.62+.19 is shown in Fig. 7.

Table C.1: Overview of the fragmented continuum sources in the ALMA sample. The properties are determined using the `c1umpfind` algorithm on the ALMA 3 mm continuum (Fig. 2), except for the extended cometary UCH<sub>II</sub> regions (HMC G9.62+0.19 9, UCH<sub>II</sub> G10.30–0.15 1, and UCH<sub>II</sub> G13.87+0.28 1), for which the properties were estimated considering the full extent of the structure. The fragments are classified into dust cores, dust+ff cores and cometary UCH<sub>II</sub> regions, further explained in Sect. 4.1. Cores with  $S/N < 15$  are not further analyzed in this study and are not classified. The relative positions,  $\Delta\alpha$  and  $\Delta\delta$ , are given with respect to the phase center of the region (Table 1).

Position	$\alpha$ J(2000)	$\delta$ J(2000)	$\Delta\alpha$ (")	$\Delta\delta$ (")	$I_{3\text{mm}}$ (mJy beam <sup>-1</sup> )	$F_{3\text{mm}}$ (mJy)	$r_{\text{out}}$ (au)	classification
IRDC G11.11–4 1	18:10:28.28	–19:22:30.7	–0.45	+0.90	1.4	10	7 700	dust core
IRDC G11.11–4 2	18:10:28.11	–19:22:35.5	–2.85	–3.90	0.48	2.1	4 400	
IRDC G11.11–4 3	18:10:28.22	–19:22:34.2	–1.35	–2.55	0.37	0.87	2 900	
IRDC G11.11–4 4	18:10:28.25	–19:22:33.4	–0.90	–1.80	0.36	0.64	2 400	
IRDC 18223–3 1	18:25:08.58	–12:45:23.9	+2.55	–8.25	2.9	11	7 900	dust core
IRDC 18223–3 2	18:25:08.31	–12:45:30.9	–1.50	–15.30	1.1	3.0	4 900	dust core
IRDC 18223–3 3	18:25:09.09	–12:44:52.5	+9.90	+23.10	0.81	0.89	2 700	dust core
IRDC 18223–3 4	18:25:08.30	–12:45:37.1	–1.65	–21.45	0.67	0.75	2 700	dust core
IRDC 18223–3 5	18:25:08.38	–12:45:24.0	–0.45	–8.40	0.57	4.4	7 100	dust core
IRDC 18223–3 6	18:25:08.66	–12:45:20.9	+3.60	–5.25	0.51	2.4	5 500	dust core
IRDC 18223–3 7	18:25:09.16	–12:45:00.5	+10.95	+15.15	0.26	0.30	2 200	
IRDC 18310–4 1	18:33:39.37	–08:21:17.1	–0.90	–6.60	1.2	1.4	5 300	dust core
IRDC 18310–4 2	18:33:39.49	–08:21:11.1	+0.90	–0.60	0.31	1.7	9 400	
IRDC 18310–4 3	18:33:39.27	–08:21:10.1	–2.40	+0.45	0.27	0.62	5 800	
IRDC 18310–4 4	18:33:38.80	–08:21:20.4	–9.30	–9.90	0.25	0.29	4 000	
HMPO IRAS 18089 1	18:11:51.47	–17:31:28.9	–0.90	+0.15	24	92	8 100	dust core
HMPO IRAS 18089 2	18:11:50.54	–17:31:28.6	–14.10	+0.45	1.9	3.4	2 400	dust core
HMPO IRAS 18089 3	18:11:51.28	–17:31:27.5	–3.60	+1.50	1.4	16	5 700	dust core
HMPO IRAS 18089 4	18:11:52.13	–17:31:05.0	+8.55	+24.00	1.1	1.1	1 500	dust core
HMPO IRAS 18089 5	18:11:51.95	–17:31:27.8	+6.00	+1.20	0.84	2.2	2 500	
HMPO IRAS 18089 6	18:11:51.02	–17:31:22.6	–7.35	+6.45	0.67	1.5	2 000	
HMPO IRAS 18089 7	18:11:51.66	–17:31:25.1	+1.80	+3.90	0.66	2.6	2 700	
HMPO IRAS 18089 8	18:11:51.53	–17:31:24.7	+0.00	+4.35	0.62	3.2	2 900	
HMPO IRAS 18089 9	18:11:49.34	–17:31:24.1	–31.35	+4.95	0.61	0.50	1 200	
HMPO IRAS 18089 10	18:11:51.89	–17:31:29.0	+5.10	–0.00	0.60	1.9	2 400	
HMPO IRAS 18182 1	18:21:09.05	–14:31:48.0	–2.55	–2.40	13	75	20 000	dust core
HMPO IRAS 18182 2	18:21:09.06	–14:31:44.7	–2.40	+0.90	2.1	4.9	9 200	dust core
HMPO IRAS 18182 3	18:21:08.92	–14:31:53.4	–4.35	–7.80	2.1	4.3	7 900	dust core
HMPO IRAS 18182 4	18:21:09.49	–14:31:49.1	+3.90	–3.45	0.44	3.4	8 800	dust core
HMPO IRAS 18264 1	18:29:14.37	–11:50:22.6	–4.80	+1.50	9.9	35	6 800	dust core
HMPO IRAS 18264 2	18:29:14.43	–11:50:24.6	–3.90	–0.45	7.8	35	7 800	dust core
HMPO IRAS 18264 3	18:29:14.82	–11:50:25.5	+1.80	–1.35	4.0	6.6	4 800	dust core
HMPO IRAS 18264 4	18:29:14.79	–11:50:24.3	+1.35	–0.15	3.1	11	6 100	dust core
HMPO IRAS 18264 5	18:29:14.48	–11:50:25.9	–3.15	–1.80	2.4	13	8 800	dust core
HMPO IRAS 18264 6	18:29:14.68	–11:50:23.8	–0.15	+0.30	1.9	6.2	4 100	dust core
HMPO IRAS 18264 7	18:29:14.49	–11:50:22.2	–3.00	+1.95	1.7	4.5	4 400	dust core
HMPO IRAS 18264 8	18:29:14.34	–11:50:20.4	–5.25	+3.75	1.4	5.3	5 600	dust core
HMPO IRAS 18264 9	18:29:14.86	–11:50:22.9	+2.40	+1.20	1.3	8.3	7 300	dust core
HMPO IRAS 18264 10	18:29:14.20	–11:50:20.2	–7.20	+3.90	0.49	1.1	3 200	dust core
HMPO IRAS 18264 11	18:29:14.69	–11:50:26.1	+0.00	–1.95	0.48	1.8	4 200	dust core
HMPO IRAS 18264 12	18:29:15.09	–11:50:19.9	+5.85	+4.20	0.36	2.6	5 800	
HMPO IRAS 18264 13	18:29:14.10	–11:50:21.0	–8.70	+3.15	0.32	1.2	4 000	
HMC G9.62+0.19 1	18:06:14.94	–20:31:43.1	+0.15	–3.75	58	100	11 400	dust+ff core
HMC G9.62+0.19 2	18:06:14.67	–20:31:31.7	–3.75	+7.65	24	49	14 100	dust+ff core
HMC G9.62+0.19 3	18:06:14.88	–20:31:39.5	–0.75	–0.15	11	37	12 400	dust core
HMC G9.62+0.19 4	18:06:14.78	–20:31:35.0	–2.10	+4.35	4.5	14	10 500	dust core
HMC G9.62+0.19 5	18:06:14.82	–20:31:37.4	–1.65	+1.95	4.4	12	9 000	dust core
HMC G9.62+0.19 6	18:06:14.36	–20:31:26.3	–8.10	+13.05	3.5	34	16 300	dust+ff core
HMC G9.62+0.19 7	18:06:15.03	–20:31:41.5	+1.35	–2.10	3.5	15	11 400	dust core
HMC G9.62+0.19 8	18:06:14.77	–20:31:30.4	–2.25	+9.00	2.1	11	10 700	dust core
HMC G9.62+0.19 9	18:06:14.03	–20:31:47.6	–12.75	–8.25	2.2	343	62 400	cometary UCH <sub>II</sub> region
HMC G9.62+0.19 10	18:06:15.16	–20:31:38.2	+3.15	+1.20	0.85	10	13 000	dust core
HMC G9.62+0.19 11	18:06:15.04	–20:31:46.7	+1.50	–7.35	0.75	3.7	7 500	dust core



Table C.1: continued.

Position	$\alpha$	$\delta$	$\Delta\alpha$	$\Delta\delta$	$I_{3\text{mm}}$	$F_{3\text{mm}}$	$r_{\text{out}}$	classification
	J(2000)	J(2000)	(")	(")	(mJy beam <sup>-1</sup> )	(mJy)	(au)	
HMC G9.62+0.19 12	18:06:14.32	-20:31:23.3	-8.55	+16.05	0.54	1.1	4 500	
HMC G9.62+0.19 13	18:06:14.93	-20:31:33.5	+0.00	+5.85	0.54	1.3	4 600	
HMC G9.62+0.19 14	18:06:15.04	-20:31:34.0	+1.50	+5.40	0.52	2.5	6 700	
HMC G9.62+0.19 15	18:06:15.01	-20:31:36.1	+1.05	+3.30	0.50	0.73	3 400	
HMC G9.62+0.19 16	18:06:15.04	-20:31:35.2	+1.50	+4.20	0.49	0.71	3 500	
HMC G9.62+0.19 17	18:06:15.27	-20:31:40.9	+4.80	-1.50	0.49	3.4	8 300	
HMC G10.47+0.03 1	18:08:38.24	-19:51:50.5	+0.45	-0.30	336	776	22 800	dust+ff core
HMC G10.47+0.03 2	18:08:38.36	-19:51:46.0	+2.10	+4.20	7.2	23	9 700	dust+ff core
HMC G10.47+0.03 3	18:08:38.26	-19:51:48.4	+0.75	+1.80	5.4	14	8 800	dust core
HMC G10.47+0.03 4	18:08:36.48	-19:52:15.1	-24.45	-24.90	3.2	3.4	4 900	
HMC G34.26+0.15 1	18:53:18.59	+01:14:58.0	+0.60	+0.30	2502	6636	4 200	dust+ff core
HMC G34.26+0.15 2	18:53:18.68	+01:15:00.1	+1.95	+2.40	111	145	1 400	dust+ff core
HMC G34.26+0.15 3	18:53:18.80	+01:14:56.1	+3.75	-1.65	81	100	1 200	dust+ff core
HMC G34.26+0.15 4	18:53:18.70	+01:14:57.3	+2.25	-0.45	62	89	1 200	dust core
HMC G34.26+0.15 5	18:53:18.72	+01:14:55.6	+2.55	-2.10	35	46	1 100	dust core
HMC G34.26+0.15 6	18:53:18.69	+01:14:54.7	+2.10	-3.00	19	14	700	
HMC G34.26+0.15 7	18:53:18.22	+01:15:00.6	-4.95	+2.85	18	64	1 600	
UCH <sub>II</sub> G10.30-0.15 1	18:08:55.96	-20:05:55.5	+0.30	-0.75	18	1006	59 300	cometary UCH <sub>II</sub> region
UCH <sub>II</sub> G13.87+0.28 1	18:14:35.81	-16:45:37.4	-2.10	-0.75	7.0	1819	66 100	cometary UCH <sub>II</sub> region

Table C.2: Radial temperature profiles in the ALMA sample. The radial temperature profiles and power-law fit according to Eq. (1) are shown in Figs. 6 and C.1.

	HCN-to-HNC ratio			CH <sub>3</sub> CN			classification
	$r_{\text{in}}$ (au)	$T_{\text{in}}$ (K)	$q$	$r_{\text{in}}$ (au)	$T_{\text{in}}$ (K)	$q$	
IRDC G11.11-4 1	...	...	...	2175	39.9±1.5	0.05±0.01	dust core
IRDC 18223-3 1	765	34.0±1.6	0.14±0.01	...	...	...	dust core
IRDC 18223-3 2	765	25.2±0.6	0.11±0.01	...	...	...	dust core
IRDC 18223-3 3	...	...	...	...	...	...	dust core
IRDC 18223-3 4	...	...	...	...	...	...	dust core
IRDC 18223-3 5	765	32.2±0.8	0.17±0.01	...	...	...	dust core
IRDC 18223-3 6	2295	30.0±1.1	0.11±0.01	...	...	...	dust core
IRDC 18310-4 1	...	...	...	...	...	...	dust core
HMPO IRAS 18089 1	...	...	...	5625	149.5±11.4	0.76±0.1	dust core
HMPO IRAS 18089 2	...	...	...	...	...	...	dust core
HMPO IRAS 18089 3	...	...	...	5625	118.6±35.9	0.75±0.14	dust core
HMPO IRAS 18089 4	...	...	...	...	...	...	dust core
HMPO IRAS 18182 1	3172	26.4±1.0	0.07±0.01	3172	107.7±30.8	0.68±0.07	dust core
HMPO IRAS 18182 2	...	...	...	...	...	...	dust core
HMPO IRAS 18182 3	3172	25.7±1.5	0.11±0.04	...	...	...	dust core
HMPO IRAS 18182 4	...	...	...	...	...	...	dust core
HMPO IRAS 18264 1	2228	32.0±1.5	0.19±0.01	2228	122.9±3.0	0.38±0.03	dust core
HMPO IRAS 18264 2	2228	38.9±2.2	0.22±0.01	2228	121.1±6.1	0.22±0.02	dust core
HMPO IRAS 18264 3	2228	34.7±1.8	0.11±0.02	...	...	...	dust core
HMPO IRAS 18264 4	...	...	...	...	...	...	dust core
HMPO IRAS 18264 5	2228	36.9±3.6	0.21±0.01	742	129.8±2.9	0.49±0.04	dust core
HMPO IRAS 18264 6	...	...	...	...	...	...	dust core
HMPO IRAS 18264 7	...	...	...	...	...	...	dust core
HMPO IRAS 18264 8	2228	33.1±1.9	0.22±0.01	742	111.7±5.9	0.4±0.03	dust core
HMPO IRAS 18264 9	...	...	...	...	...	...	dust core
HMPO IRAS 18264 10	...	...	...	...	...	...	dust core
HMPO IRAS 18264 11	2228	43.7±1.7	0.31±0.02	...	...	...	dust core
HMC G9.62+0.19 1	...	...	...	11700	93.5±46.6	0.67±0.09	dust+ff core
HMC G9.62+0.19 2	...	...	...	11700	129.8±21.7	0.73±0.17	dust+ff core
HMC G9.62+0.19 3	...	...	...	11700	157.4±23.0	0.6±0.09	dust core
HMC G9.62+0.19 4	...	...	...	...	...	...	dust core
HMC G9.62+0.19 5	...	...	...	11700	130.7±11.8	0.7±0.06	dust core

Table C.2: continued.

	HCN-to-HNC ratio			CH <sub>3</sub> CN			classification
	$r_{\text{in}}$ (au)	$T_{\text{in}}$ (K)	$q$	$r_{\text{in}}$ (au)	$T_{\text{in}}$ (K)	$q$	
HMC G9.62+0.19 6	...	...	...	...	...	...	dust+ff core
HMC G9.62+0.19 7	...	...	...	11700	114.6±9.9	0.64±0.06	dust core
HMC G9.62+0.19 8	...	...	...	11700	105.6±8.1	0.34±0.08	dust core
HMC G9.62+0.19 9	...	...	...	...	...	...	cometary UCH <sub>II</sub> region
HMC G9.62+0.19 10	...	...	...	...	...	...	dust core
HMC G9.62+0.19 11	...	...	...	...	...	...	dust core
HMC G10.47+0.03 1	...	...	...	19350	210.4±31.9	0.62±0.13	dust+ff core
HMC G10.47+0.03 2	6450	21.6±0.7	0.16±0.02	19350	143.2±4.3	0.24±0.06	dust+ff core
HMC G10.47+0.03 3	...	...	...	19350	167.1±23.5	0.27±0.19	dust core
HMC G34.26+0.15 1	...	...	...	1080	245.8±63.2	0.68±0.04	dust+ff core
HMC G34.26+0.15 2	...	...	...	1080	128.1±5.5	0.16±0.04	dust+ff core
HMC G34.26+0.15 3	...	...	...	...	...	...	dust+ff core
HMC G34.26+0.15 4	...	...	...	360	246.6±8.0	0.22±0.03	dust core
HMC G34.26+0.15 5	...	...	...	360	233.5±5.4	0.24±0.0	dust core
UCH <sub>II</sub> G10.30−0.15 1	...	...	...	...	...	...	cometary UCH <sub>II</sub> region
UCH <sub>II</sub> G13.87+0.28 1	...	...	...	2925	36.2±1.4	0.06±0.03	cometary UCH <sub>II</sub> region

Table C.3: H<sub>2</sub> column density  $N(\text{H}_2)$  and mass  $M$  in the ALMA sample. The beam-averaged temperature  $\bar{T}$  are computed from the temperature maps (Sect. 5). The dust continuum optical depth  $\tau_{\nu}^{\text{cont}}$ , H<sub>2</sub> column density  $N(\text{H}_2)$ , and mass  $M$  are calculated according to Eqs. (8), (6), and (7), respectively.

	HCN/HNC $\bar{T}$ (K)	CH <sub>3</sub> CN $\bar{T}$ (K)	CH <sub>3</sub> <sup>13</sup> CN $\bar{T}$ (K)	$\tau_{\nu}^{\text{cont}}$	$N(\text{H}_2)$ (cm <sup>-2</sup> )	$M$ ( $M_{\odot}$ )	classification
IRDC G11.11−4 1	...	39.9±0.9	...	5.9(−3)	1.1(24)±2.2(23)	0.82±0.16	dust core
IRDC 18223−3 1	34.0±1.5	42.4±5.2	...	1.3(−2)	2.4(24)±5.8(23)	1.21±0.29	dust core
IRDC 18223−3 2	25.2±0.4	...	...	9.0(−3)	1.7(24)±3.4(23)	0.60±0.12	dust core
IRDC 18223−3 3	...	...	...	...	...	...	dust core
IRDC 18223−3 4	...	...	...	...	...	...	dust core
IRDC 18223−3 5	32.2±0.6	...	...	3.4(−3)	6.4(23)±1.3(23)	0.67±0.14	dust core
IRDC 18223−3 6	33.5±1.2	...	...	2.9(−3)	5.5(23)±1.1(23)	0.36±0.07	dust core
IRDC 18310−4 1	...	...	...	...	...	...	dust core
HMPO IRAS 18089 1	19.6±0.4	179.0±1.0	96.0±1.2	6.0(−2)	1.1(25)±2.2(24)	3.20±0.64	dust core
HMPO IRAS 18089 2	...	...	...	...	...	...	dust core
HMPO IRAS 18089 3	...	151.6±7.0	...	2.1(−3)	4.0(23)±8.3(22)	0.35±0.07	dust core
HMPO IRAS 18089 4	...	...	...	...	...	...	dust core
HMPO IRAS 18182 1	29.0±0.5	101.6±2.4	...	2.1(−2)	3.9(24)±7.9(23)	6.08±1.22	dust core
HMPO IRAS 18182 2	22.0±0.7	33.1±2.2	...	1.1(−2)	2.1(24)±4.5(23)	1.28±0.27	dust core
HMPO IRAS 18182 3	26.1±0.2	...	...	1.4(−2)	2.6(24)±5.3(23)	1.44±0.29	dust core
HMPO IRAS 18182 4	18.5±0.1	51.1±11.3	...	1.5(−3)	2.8(23)±8.4(22)	0.56±0.17	dust core
HMPO IRAS 18264 1	35.6±0.7	130.0±1.1	...	1.4(−2)	2.6(24)±5.2(23)	1.18±0.24	dust core
HMPO IRAS 18264 2	42.6±0.5	136.7±2.7	...	1.0(−2)	1.9(24)±3.9(23)	1.14±0.23	dust core
HMPO IRAS 18264 3	36.2±0.7	...	...	2.1(−2)	4.0(24)±8.1(23)	0.84±0.17	dust core
HMPO IRAS 18264 4	20.8±1.1	...	...	3.1(−2)	5.7(24)±1.2(24)	2.48±0.52	dust core
HMPO IRAS 18264 5	39.5±1.0	129.8±14.3	...	3.4(−3)	6.4(23)±1.5(23)	0.45±0.10	dust core
HMPO IRAS 18264 6	22.5±0.3	26.2±6.4	...	1.5(−2)	2.7(24)±9.1(23)	1.12±0.37	dust core
HMPO IRAS 18264 7	22.1±0.4	...	...	1.5(−2)	2.9(24)±5.8(23)	0.99±0.20	dust core
HMPO IRAS 18264 8	37.6±1.3	111.7±20.9	...	2.3(−3)	4.3(23)±1.2(23)	0.21±0.06	dust core
HMPO IRAS 18264 9	18.2±0.1	...	...	1.4(−2)	2.7(24)±5.3(23)	2.25±0.45	dust core
HMPO IRAS 18264 10	19.8±0.5	23.8±4.7	...	4.1(−3)	7.7(23)±2.3(23)	0.23±0.07	dust core
HMPO IRAS 18264 11	43.6±0.2	...	...	2.1(−3)	3.9(23)±7.8(22)	0.19±0.04	dust core
HMC G9.62+0.19 1	...	72.2±1.9	...	6.4(−2)	1.2(25)±2.4(24)	6.44±1.30	dust+ff core
HMC G9.62+0.19 2	17.8±0.2	195.0±29.7	124.4±3.6	3.1(−2)	5.7(24)±1.1(24)	3.69±0.75	dust+ff core
HMC G9.62+0.19 3	...	161.9±6.2	120.8±7.9	1.8(−2)	3.3(24)±7.0(23)	3.55±0.75	dust core
HMC G9.62+0.19 4	...	97.8±6.3	...	8.9(−3)	1.7(24)±3.5(23)	1.72±0.36	dust core
HMC G9.62+0.19 5	15.2±0.0	160.2±36.9	...	5.3(−3)	1.0(24)±3.1(23)	0.90±0.28	dust core
HMC G9.62+0.19 6	24.2±0.7	36.2±1.2	...	8.2(−4)	1.5(23)±3.1(22)	0.47±0.10	dust+ff core

Notes. The optical depth  $\tau_{\nu}^{\text{cont}}$  and column density  $N$  are given as a(b) meaning  $a \times 10^b$ .

Table C.3: continued.

	HCN/HNC $\bar{T}$ (K)	CH <sub>3</sub> CN $\bar{T}$ (K)	CH <sub>3</sub> <sup>13</sup> CN $\bar{T}$ (K)	$\tau_{\nu}^{\text{cont}}$	$N(\text{H}_2)$ (cm <sup>-2</sup> )	$M$ ( $M_{\odot}$ )	classification
HMC G9.62+0.19 7	...	109.5±17.7	...	6.2(-3)	1.2(24)±3.0(23)	1.57±0.41	dust core
HMC G9.62+0.19 8	...	108.0±1.6	...	3.8(-3)	7.2(23)±1.5(23)	1.17±0.23	dust core
HMC G9.62+0.19 9	...	...	...	...	...	...	cometary UCHII region
HMC G9.62+0.19 10	...	80.6±4.0	...	2.1(-3)	3.9(23)±8.0(22)	1.47±0.30	dust core
HMC G9.62+0.19 11	...	36.1±3.0	...	4.2(-3)	7.9(23)±1.7(23)	1.26±0.28	dust core
HMC G10.47+0.03 1	...	89.0±32.6	148.9±10.2	5.0(-1)	7.4(25)±1.6(25)	150.61±31.89	dust+ff core
HMC G10.47+0.03 2	21.6±0.5	192.8±21.5	...	7.7(-4)	1.5(23)±3.3(22)	0.40±0.09	dust+ff core
HMC G10.47+0.03 3	16.1±0.6	216.5±13.6	143.4±5.1	9.1(-3)	1.7(24)±3.5(23)	3.90±0.79	dust core
HMC G34.26+0.15 1	...	249.8±0.2	153.6±7.1	...	2.2(26)±4.6(25)	17.84±3.66	dust+ff core
HMC G34.26+0.15 2	...	157.4±21.6	...	3.7(-2)	6.8(24)±1.7(24)	0.27±0.07	dust+ff core
HMC G34.26+0.15 3	...	112.9±10.3	...	1.8(-2)	3.5(24)±7.6(23)	0.13±0.03	dust+ff core
HMC G34.26+0.15 4	38.1±1.2	246.6±3.6	173.5±13.6	8.6(-2)	1.6(25)±3.3(24)	0.68±0.15	dust core
HMC G34.26+0.15 5	21.5±0.4	233.5±2.5	179.6±14.0	4.7(-2)	8.6(24)±1.9(24)	0.34±0.07	dust core
UCHII G10.30-0.15 1	16.5±0.1	31.4±1.3	...	1.4(-2)	2.6(24)±5.3(23)	22.71±4.65	cometary UCHII region
UCHII G13.87+0.28 1	...	36.2±1.6	...	8.7(-3)	1.6(24)±3.4(23)	76.30±15.68	cometary UCHII region

Notes. The optical depth  $\tau_{\nu}^{\text{cont}}$  and column density  $N$  are given as a(b) meaning  $a \times 10^b$ .

Table C.4: Visibility and density profiles in the ALMA sample. The visibility profiles are shown in Figs. 7 (HMC G9.62+0.19 2) and C.2 (all remaining sources). Two power-law profiles were fitted to the observed visibility profile with  $\alpha_1$  and  $\alpha_2$  tracing roughly the clump and core scales, respectively. The corresponding density power-law indices  $p_1$  and  $p_2$  (Eq. 2) are then estimated according to Eq. (5) considering the observed temperature power-law index  $q$  (Table C.2).

	$\alpha_1$	$p_1$	$\alpha_2$	$p_2$	classification
IRDC G11.11-4 1	-0.42 ± 0.06	2.53 ± 0.06	-0.06 ± 0.02	2.89 ± 0.02	dust core
IRDC 18223-3 1	-0.60 ± 0.05	2.26 ± 0.05	-0.03 ± 0.01	2.83 ± 0.01	dust core
IRDC 18223-3 2	-0.61 ± 0.06	2.28 ± 0.06	-0.01 ± 0.01	2.88 ± 0.01	dust core
IRDC 18223-3 3	-0.61 ± 0.06	...	-0.02 ± 0.01	...	dust core
IRDC 18223-3 4	-0.61 ± 0.06	...	-0.00 ± 0.01	...	dust core
IRDC 18223-3 5	-0.61 ± 0.06	2.22 ± 0.06	-0.00 ± 0.01	2.83 ± 0.01	dust core
IRDC 18223-3 6	-0.61 ± 0.06	2.28 ± 0.06	-0.00 ± 0.01	2.89 ± 0.01	dust core
IRDC 18310-4 1	-0.58 ± 0.07	...	-0.00 ± 0.01	...	dust core
HMPO IRAS 18089 1	-0.49 ± 0.02	1.75 ± 0.10	-0.49 ± 0.03	1.75 ± 0.10	dust core
HMPO IRAS 18089 2	-0.68 ± 0.02	...	-0.11 ± 0.02	...	dust core
HMPO IRAS 18089 3	-0.66 ± 0.02	1.59 ± 0.14	-0.12 ± 0.04	2.13 ± 0.15	dust core
HMPO IRAS 18089 4	-0.68 ± 0.02	...	-0.07 ± 0.01	...	dust core
HMPO IRAS 18182 1	-0.42 ± 0.02	1.90 ± 0.07	-0.43 ± 0.07	1.89 ± 0.10	dust core
HMPO IRAS 18182 2	-0.42 ± 0.01	...	-0.46 ± 0.06	...	dust core
HMPO IRAS 18182 3	-0.45 ± 0.01	2.44 ± 0.04	-0.39 ± 0.07	2.50 ± 0.08	dust core
HMPO IRAS 18182 4	-0.45 ± 0.02	...	-0.39 ± 0.07	...	dust core
HMPO IRAS 18264 1	-0.72 ± 0.02	1.90 ± 0.04	-0.19 ± 0.02	2.43 ± 0.04	dust core
HMPO IRAS 18264 2	-0.76 ± 0.03	2.02 ± 0.04	-0.17 ± 0.02	2.61 ± 0.03	dust core
HMPO IRAS 18264 3	-0.85 ± 0.05	2.04 ± 0.05	-0.13 ± 0.01	2.76 ± 0.02	dust core
HMPO IRAS 18264 4	-0.84 ± 0.05	...	-0.14 ± 0.02	...	dust core
HMPO IRAS 18264 5	-0.82 ± 0.04	1.69 ± 0.06	-0.09 ± 0.01	2.42 ± 0.04	dust core
HMPO IRAS 18264 6	-0.81 ± 0.04	...	-0.10 ± 0.01	...	dust core
HMPO IRAS 18264 7	-0.81 ± 0.03	...	-0.10 ± 0.02	...	dust core
HMPO IRAS 18264 8	-0.80 ± 0.04	1.80 ± 0.05	-0.11 ± 0.02	2.49 ± 0.04	dust core
HMPO IRAS 18264 9	-0.83 ± 0.05	...	-0.13 ± 0.02	...	dust core
HMPO IRAS 18264 10	-0.80 ± 0.04	...	-0.11 ± 0.01	...	dust core
HMPO IRAS 18264 11	-0.80 ± 0.04	1.89 ± 0.04	-0.10 ± 0.01	2.59 ± 0.02	dust core
HMC G9.62+0.19 1	-1.30 ± 0.12	1.03 ± 0.15	-0.40 ± 0.04	1.93 ± 0.10	dust+ff core
HMC G9.62+0.19 2	-1.32 ± 0.10	0.95 ± 0.20	-0.28 ± 0.03	1.99 ± 0.17	dust+ff core
HMC G9.62+0.19 3	-1.36 ± 0.07	1.04 ± 0.11	-0.22 ± 0.06	2.18 ± 0.11	dust core
HMC G9.62+0.19 4	-1.30 ± 0.07	...	-0.09 ± 0.05	...	dust core
HMC G9.62+0.19 5	-1.30 ± 0.07	1.00 ± 0.09	-0.08 ± 0.05	2.22 ± 0.08	dust core
HMC G9.62+0.19 6	-1.26 ± 0.07	...	-0.18 ± 0.05	...	dust+ff core
HMC G9.62+0.19 7	-1.27 ± 0.07	1.09 ± 0.09	-0.09 ± 0.06	2.27 ± 0.08	dust core
HMC G9.62+0.19 8	-1.28 ± 0.07	1.38 ± 0.11	-0.10 ± 0.05	2.56 ± 0.09	dust core

Table C.4: continued.

	$\alpha_1$	$p_1$	$\alpha_2$	$p_2$	classification
HMC G9.62+0.19 9	$-1.29 \pm 0.07$	...	$-0.17 \pm 0.04$	...	cometary UCH <sub>II</sub> region
HMC G9.62+0.19 10	$-1.29 \pm 0.07$	...	$-0.09 \pm 0.05$	...	dust core
HMC G9.62+0.19 11	$-1.29 \pm 0.07$	...	$-0.09 \pm 0.05$	...	dust core
HMC G10.47+0.03 1	$-0.19 \pm 0.02$	$2.19 \pm 0.13$	$-0.64 \pm 0.02$	$1.74 \pm 0.13$	dust+ff core
HMC G10.47+0.03 2	$-0.23 \pm 0.02$	$2.53 \pm 0.06$	$-0.61 \pm 0.06$	$2.15 \pm 0.08$	dust+ff core
HMC G10.47+0.03 3	$-0.23 \pm 0.02$	$2.50 \pm 0.19$	$-0.56 \pm 0.06$	$2.17 \pm 0.20$	dust core
HMC G34.26+0.15 1	$-0.13 \pm 0.03$	$2.19 \pm 0.05$	$-0.85 \pm 0.06$	$1.47 \pm 0.07$	dust+ff core
HMC G34.26+0.15 2	$-0.18 \pm 0.02$	$2.66 \pm 0.04$	$-0.52 \pm 0.05$	$2.32 \pm 0.06$	dust+ff core
HMC G34.26+0.15 3	$-0.18 \pm 0.02$	...	$-0.52 \pm 0.06$	...	dust+ff core
HMC G34.26+0.15 4	$-0.17 \pm 0.02$	$2.61 \pm 0.04$	$-0.53 \pm 0.06$	$2.25 \pm 0.07$	dust core
HMC G34.26+0.15 5	$-0.17 \pm 0.02$	$2.59 \pm 0.02$	$-0.52 \pm 0.06$	$2.24 \pm 0.06$	dust core
UCH <sub>II</sub> G10.30-0.15 1	$-0.49 \pm 0.06$	...	$-1.06 \pm 0.08$	...	cometary UCH <sub>II</sub> region
UCH <sub>II</sub> G13.87+0.28 1	$-1.80 \pm 0.14$	$1.14 \pm 0.14$	$-0.32 \pm 0.07$	$2.62 \pm 0.08$	cometary UCH <sub>II</sub> region

### Appendix D: Free-free contribution

Figure D.1 show the H(40) $\alpha$  recombination line integrated intensity map of all regions. In Sect. 4.2 we estimate the contribution of free-free emission at 3 mm wavelengths based on the H(40) $\alpha$  recombination line (Fig. D.2) using Eq. (3).



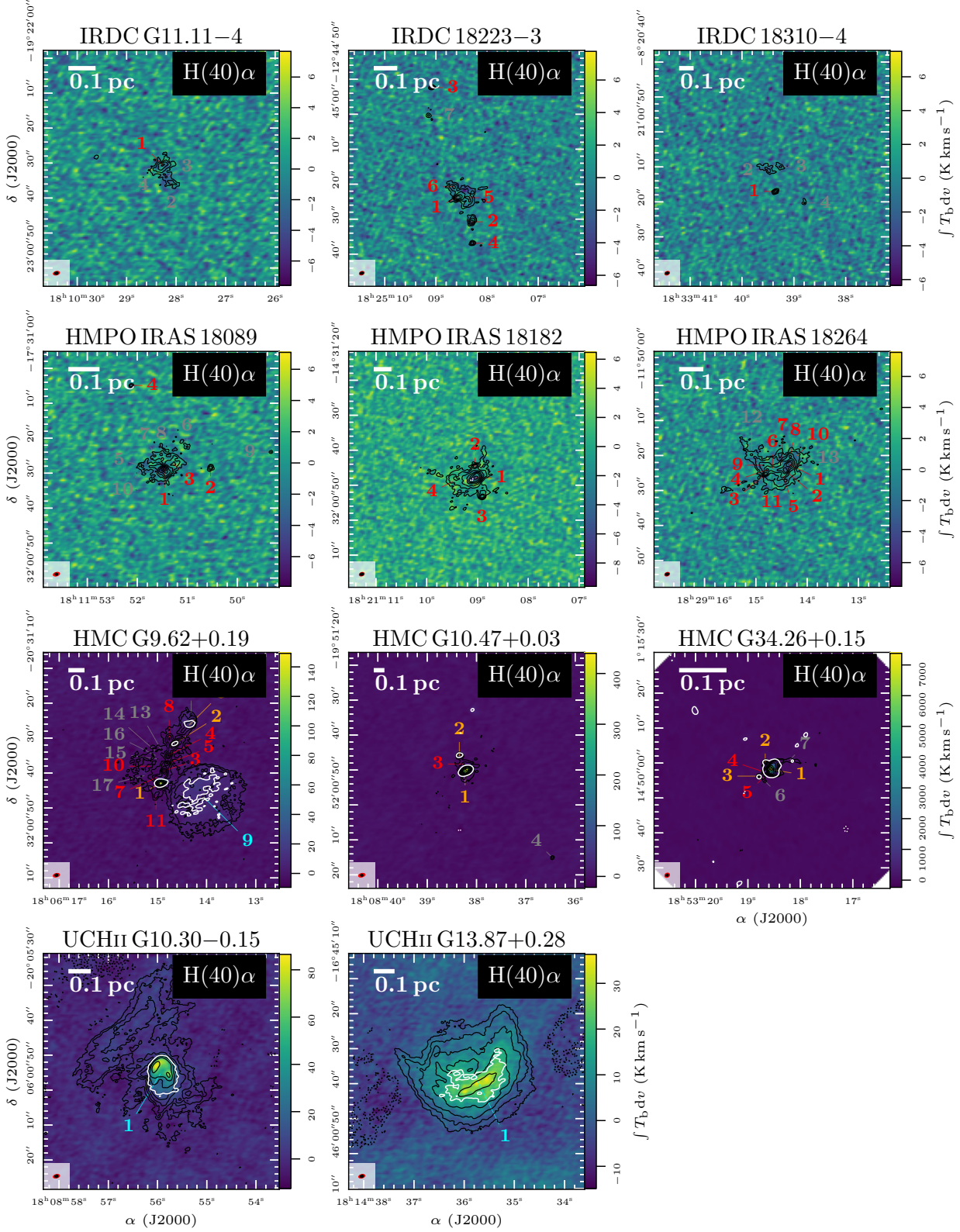


Fig. D.1: Integrated intensity maps of H(40) $\alpha$ . In each panel, the H(40) $\alpha$  integrated intensity of the region is shown in color and white contours (dotted:  $-5\sigma$  and solid:  $+5\sigma$ ). The 3 mm continuum data is shown by black contours. The dotted black contour marks the  $-5\sigma_{\text{cont}}$  level. The solid black contours start at  $5\sigma_{\text{cont}}$  and contour steps increase by a factor of 2 (e.g., 5, 10, 20,  $40\sigma_{\text{cont}}$ ). The synthesized beam of the continuum (black) and line (red) data is shown in the bottom left corner. The continuum fragments are classified into dust cores (red), dust+ff cores (orange), cometary UCHII regions (cyan), further explained in Sect. 4.1. Fragments with  $S/N < 15$  are not analyzed in this study and are labeled in grey.

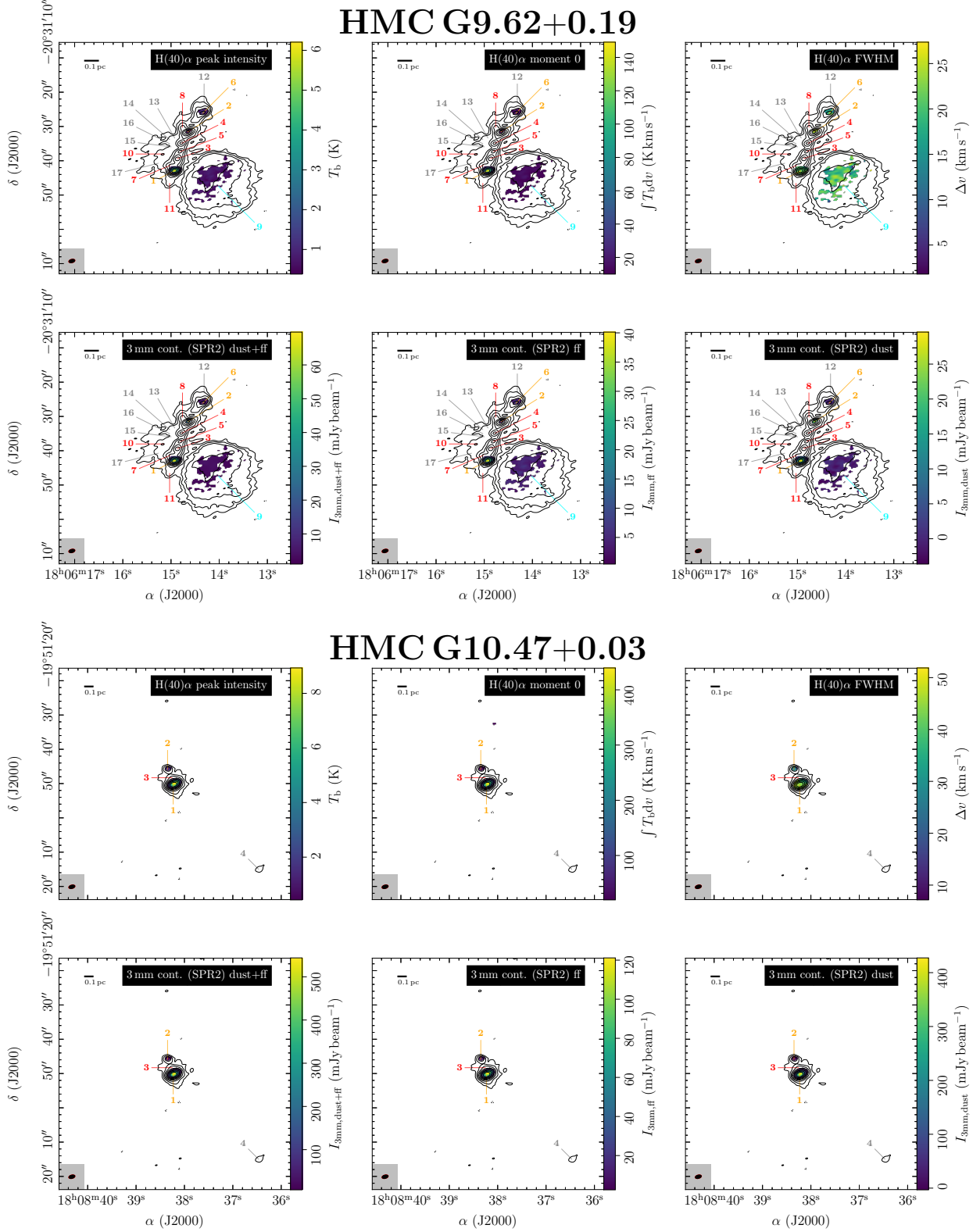


Fig. D.2: Estimate of the free-free contribution at 3 mm (Eq. 3). In all panels, the SPR2 3 mm continuum is shown in contours. The dotted black contour marks the  $-5\sigma_{\text{cont}}$  level. The solid black contours start at  $5\sigma_{\text{cont}}$  and contour steps increase by a factor of 2 (e.g., 5, 10, 20,  $40\sigma_{\text{cont}}$ ). The top panels show in color the H(40) $\alpha$  peak intensity, integrated intensity, and line width derived from the 2nd moment. The bottom panels show in color the SPR2 3 mm continuum (dust + ff), 3 mm ff continuum (estimated using Eq. 3), and 3 mm dust continuum. The synthesized beam size of the continuum and line data is shown in the bottom left corner in black and red, respectively. In all panels, the area where the H(40) $\alpha$  integrated intensity and SPR2 continuum have a  $S/N < 5$  are masked. The continuum fragments are classified into dust cores (red), dust+ff cores (orange), cometary UCHII regions (cyan), further explained in Sect. 4.1. Fragments with  $S/N < 15$  are not analyzed in this study and are labeled in grey.

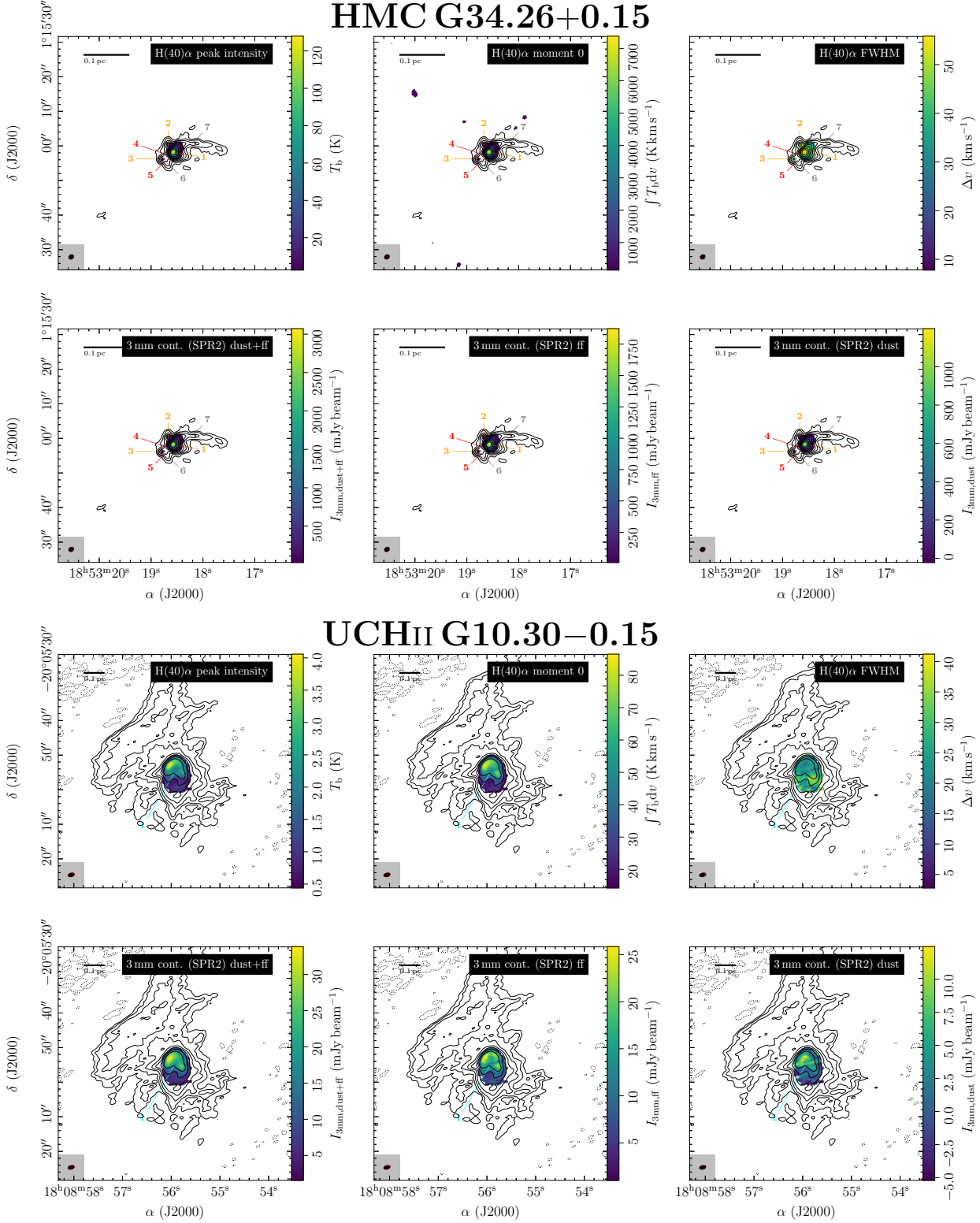


Fig. D.2 (cont.): Estimate of the free-free contribution at 3 mm (Eq. 3). In all panels, the SPR2 3 mm continuum is shown in contours. The dotted black contour marks the  $-5\sigma_{\text{cont}}$  level. The solid black contours start at  $5\sigma_{\text{cont}}$  and contour steps increase by a factor of 2 (e.g., 5, 10, 20,  $40\sigma_{\text{cont}}$ ). The top panels show in color the H(40) $\alpha$  peak intensity, integrated intensity, and line width derived from the 2nd moment. The bottom panels show in color the SPR2 3 mm continuum (dust + ff), 3 mm ff continuum (estimated using Eq. 3), and 3 mm dust continuum. The synthesized beam size of the continuum and line data is shown in the bottom left corner in black and red, respectively. In all panels, the area where the H(40) $\alpha$  integrated intensity and SPR2 continuum have a  $S/N < 5$  are masked. The continuum fragments are classified into dust cores (red), dust+ff cores (orange), cometary UCHII regions (cyan), further explained in Sect. 4.1. Fragments with  $S/N < 15$  are not analyzed in this study and are labeled in grey.

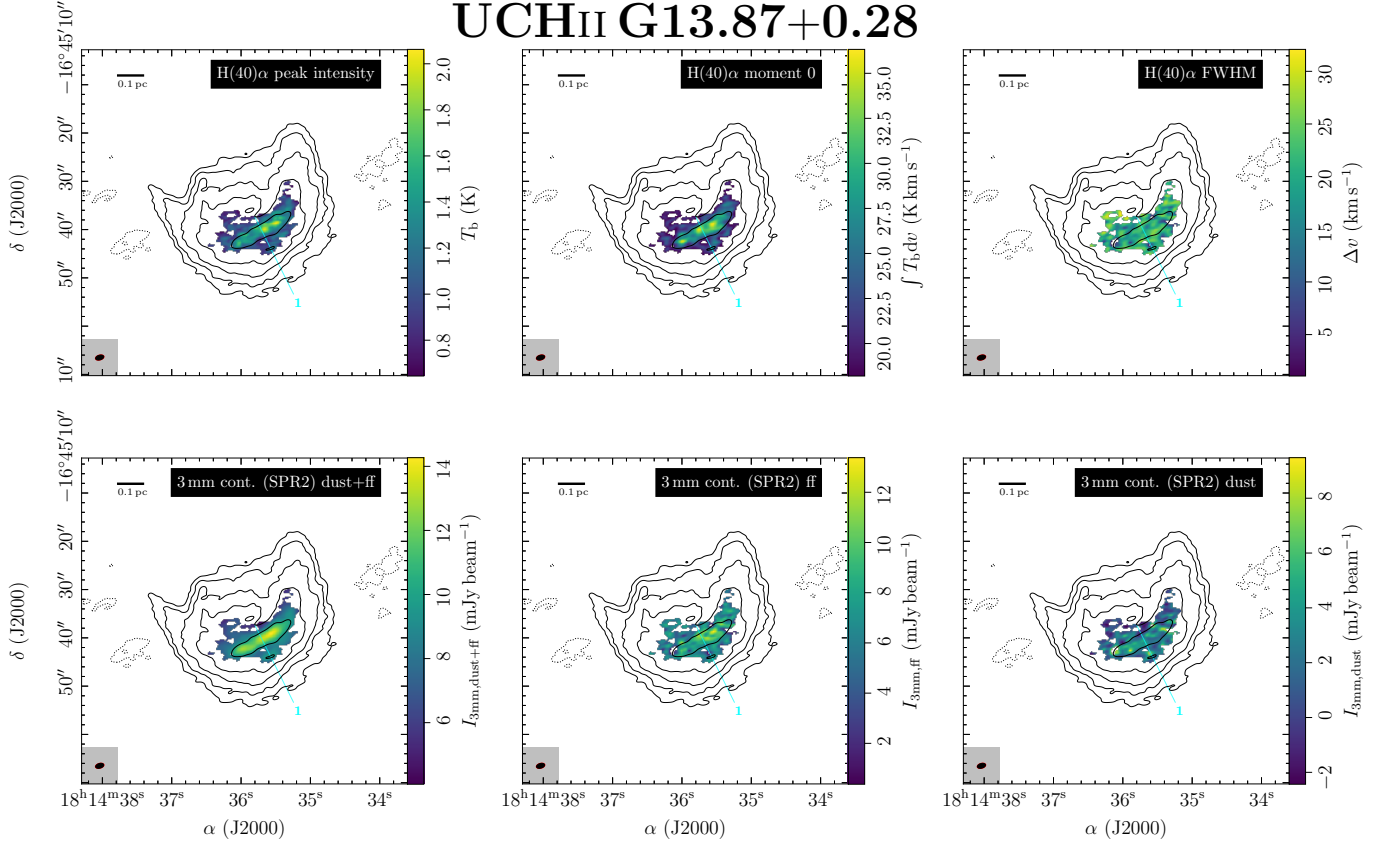


Fig. D.2 (cont.): Estimate of the free-free contribution at 3 mm (Eq. 3). In all panels, the SPR2 3 mm continuum is shown in contours. The dotted black contour marks the  $-5\sigma_{\text{cont}}$  level. The solid black contours start at  $5\sigma_{\text{cont}}$  and contour steps increase by a factor of 2 (e.g., 5, 10, 20,  $40\sigma_{\text{cont}}$ ). The top panels show in color the H(40) $\alpha$  peak intensity, integrated intensity, and line width derived from the 2nd moment. The bottom panels show in color the SPR2 3 mm continuum (dust + ff), 3 mm ff continuum (estimated using Eq. 3), and 3 mm dust continuum. The synthesized beam size of the continuum and line data is shown in the bottom left corner in black and red, respectively. In all panels, the area where the H(40) $\alpha$  integrated intensity and SPR2 continuum have a  $S/N < 5$  are masked. The continuum fragments are classified into dust cores (red), dust+ff cores (orange), cometary UCHII regions (cyan), further explained in Sect. 4.1. Fragments with  $S/N < 15$  are not analyzed in this study and are labeled in grey.